SECOND SOUND SHOCK WAVES IN ROTATING SUPERFLUID HELIUM

Thesis by
John Robert Torczynski

In Partial Fulfillment
of the Requirements for the Degree of
Doctor of Philosophy

California Institute of Technology
Pasadena, California

1983
(Submitted May 27, 1983)

To Jeanne, my bride to be. Our birthdays were special this year.

ACKNOWLEDGEMENTS

I would like to thank the following people for help, advice, and encouragement throughout this project.

Professor Hans W. Liepmann has my greatest admiration and respect. I particularly appreciate the freedom and support that he gave me to pursue research topics of my choosing. It is my hope that some of his enthusiasm to understand and his ability to do so will rub off.

Thomas Roesgen greatly aided the author by introducing him to the computer as a practical lab research tool. He also provided constant evaluation, insight, and advice as difficulties were encountered and surmounted (he also held the top end of the helium transfer tube).

Bill Kath gave constant encouragement and friendship throughout the years here. He made several observations that forced the author to understand certain helium experiments more clearly.

Tim Turner, my predecessor, to use his own words has "generously enlightened the author about the mysteries that persist in modern cryogenic technology." He has been an invaluable source of experimental knowledge and insight, which he has frequently shared with the author.

Thanks to those of GALCIT who have lent help, encouragement, and (most importantly) equipment. Special thanks to Jacquelyn Beard, whose typing and word processing abilities were crucial to the on-time completion of this thesis. This research was supported by NASA Grant NSG-7508 and by Caltech.

ABSTRACT

Second sound shock waves have been used to examine the breakdown of superfluidity in bulk He II. The maximum counterflow velocity achieved in this manner was measured at a variety of temperatures and pressures. The results are found to agree with predictions of vortex nucleation theories (Langer & Fisher, 1967) in their pressure and temperature dependences although it was shown that dissipation occurred only near the heater. A simple scaling argument is suggested, assuming breakdown occurs near the heater. A vortex dynamics model of breakdown (following the method of Turner, private communication) is developed.

To examine the effect of vorticity on breakdown, second sound shocks were produced in rotating helium. Experiments were performed in which the shocks propagated either along or normal to the axis of rotation, called "axial" and "transverse" cases, respectively. In both cases the decay was seen to increase monotonically with the rotation rate. Furthermore, the decay was ongoing, rather than being confined to a narrow region near the heater. However, the extraordinary dissipation in the transverse case seemed to be related primarily to the arrival of secondary waves from the heater-sidewall boundary. An explanation of this difference is put forth in terms of vortex nucleation in the bulk fluid, using ideas similar to Crocco's Theorem.

In order to examine the breakdown of superfluidity away from walls in nonrotating fluid, spherically converging second sound shocks were produced. The temperature jumps of the waves were measured, and exact numerical solutions of the two-fluid jump conditions (Moody, 1983) were used to calculate the relative velocity in each case. The experiments show that the processes limiting the

counterflow velocity still occur at the heater although the strongest final waves produced have relative velocities in excess of 10 $\frac{m}{sec}$. These are the largest relative velocities ever produced in the bulk fluid.

TABLE OF CONTENTS

Chapter 1

BEHAVIOR OF SECOND SOUND SHOCK WAVES

The breakdown of superfluidity remains one of the most interesting aspects of the physics of Helium II. Of principal concern is the occurrence of additional dissipation during counterflow experiments with large heat fluxes. When the relative velocity between normal and super components exceeds a certain value, the two components can no longer be thought of as noninteracting fluids. Rather, new dissipative mechanisms come into play and limit the maximum counterflow velocity obtained.

This "critical" dissipation can be characterized by a fundamental, or intrinsic, critical velocity. By fundamental or intrinsic, it is meant that this critical velocity is geometry independent (and frame invariant). Previous investigators had studied critical velocities, but their experiments were performed in constricted geometries, such as closely packed powders (Clow and Reppy, 1967), porous materials (Notarys, 1969), and thin films of helium on glass cylinders (Hess, 1971). However, since it is intrinsic, this critical velocity should be able to be observed out in the bulk fluid (away from walls).

A second sound shock wave is the ideal method for setting up counterflows and studying the intrinsic critical velocity in bulk fluid. Planar second sound shocks provide an abrupt change of flow state, impulsively accelerating quiescent fluid to a finite uniform relative velocity. This change is accomplished in less than a microsecond, the length of time required for a shock to travel its own thickness. Furthermore, wall effects can be eliminated by time resolution because they require a finite amount of time to propagate inward from the walls. Moreover, the wave fronts remain extremely planar even with the

strongest shocks, as schlieren photography has revealed, so the motion remains one-dimensional.

1.1. Weak Waves

Second sound shocks have been used by investigators (Turner, 1979) to study the breakdown of superfluidity. Before a discussion of the breakdown process, it is best to recall the nonlinear evolution of a temperature wave in superfluid helium. Suppose an arbitrary one-dimensional heat pulse is introduced into the fluid by means of a wall heater. At an instant in time the pulse may appear as in Figure 1.1.

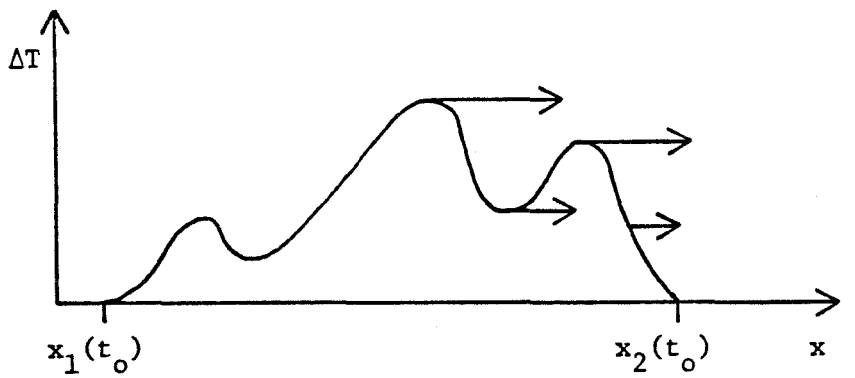

Figure 1.1. Propagation of an arbitrary temperature profile at time t_o.

Each point on the profile travels without decaying at its characteristic velocity, which in the limit of small perturbations is the following,

$$u = a\left[1 + B\,\frac{\Delta T}{T}\right] \tag{1.1}$$

where a is the unperturbed speed of second sound, $\frac{\Delta T}{T}$ is the normalized

temperature rise above the ambient temperature, and $B = B(p,T)$ is the non-linear steepening coefficient. This result is due to Khalatnikov, who derived B explicitly.

$$B(p,T) = T \left[\frac{\partial}{\partial T}\right]_p \ln\left\{\frac{\alpha^3 c_p}{T}\right\} \tag{1.2}$$

It is worth noting that B is positive from 0.95 K to 1.88 K and negative from 1.88 K to T_λ.

Suppose that $B > 0$ for the profile in Figure 1.1. Thus, the higher points of the profile move more rapidly than the lower points, as shown. However, the area under the profile is preserved. Let $A(t)$ be the area of the pulse at time t, where $x_1(t)$ and $x_2(t)$ are chosen so that $\Delta T(x_1,t) = \Delta T(x_2,t) = \Delta T_o$. Therefore $u(x_1,t) = u(x_2,t)$.

$$A(t) = \int_{x_1(t)}^{x_2(t)} \Delta T(x,t)\, dx$$

$$\frac{dA}{dt} = \int_{x_1(t)}^{x_2(t)} \frac{\partial \Delta T}{\partial t} dx + \left[\, \Delta T(x,t)\, u(x,t)\right] \Big|_{x_1(t)}^{x_2(t)}$$

Now the boundary term vanishes by choice of x_1 and x_2. Since each point of the profile travels at its characteristic velocity, we have

$$\frac{\partial \Delta T}{\partial t} = -u\, \frac{\partial \Delta T}{\partial x} = \frac{-T}{\alpha B} u\, \frac{\partial u}{\partial x}.$$

Thus

$$\frac{dA}{dt} = \frac{-T}{2aB} \int_{x_1}^{x_2} d(u^2) = 0,$$

so $A(t)$ is constant in time (Whitham, 1974).

Although the area of the profile is invariant, the shape is modified since points on the profile with large values of ΔT move more quickly than points with small values of ΔT . Hence, the profile steepens and, in fact, will become multivalued at some later time, as shown in Figure 1.2.

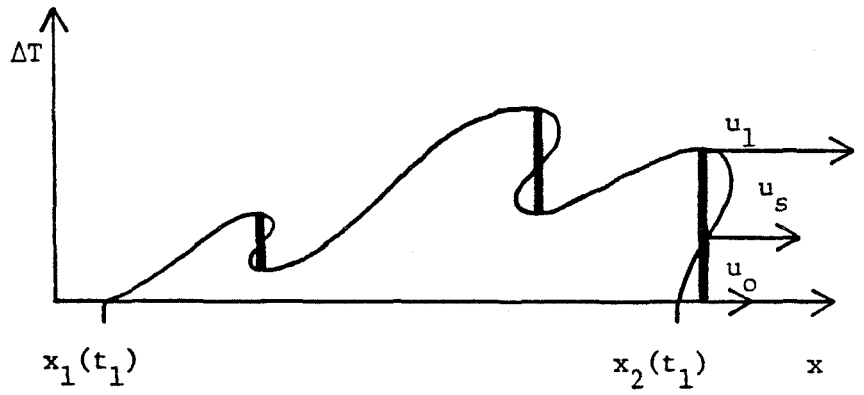

Figure 1.2. The temperature profile at a later time t_1 .

Clearly this multivaluedness is unphysical. What actually occurs is that a shock is formed in each multivalued region (indicated by bold lines in Figure 1.2).

This shock may be thought of as a discontinuity propagating at some intermediate velocity determined by integrating the conservation equations across the shock. In practice, however, since second sound shocks are quite weak,

$$\left|\frac{\Delta T}{T}\right| << 1 \text{ and } M-1 << 1,$$

and the shock velocity is found to an excellent approximation to be the average characteristic velocity of the lopped-off regions. In cases where B may be regarded as constant (away from T = 1.88 K, at which B passes through 0), the shock velocity u_s is the average of the characteristic velocities at the bottom and top. Thus we have

$$u_s = \frac{1}{2}(u_o + u_1) = a\left|1 + \frac{1}{2}B\ \frac{\Delta T}{T}\right|$$

since

$$u_o = a$$

and

$$u_1 = a\left|1 + B\,\Delta\frac{T}{T}\right|$$

or in terms of the Mach number

$$M = \frac{u_s}{a} = 1 + \frac{1}{2}B\ \frac{\Delta T}{T} \qquad (1.3)$$

which is Khalatnikov's result. In regions where B varies rapidly with temperature, the averaging must be carried out in detail. The location of the shock is determined by the area preservation property already discussed. Since the area

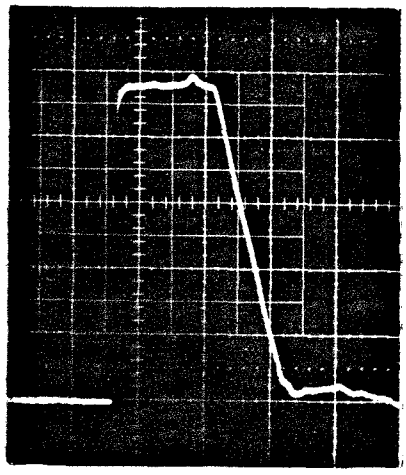

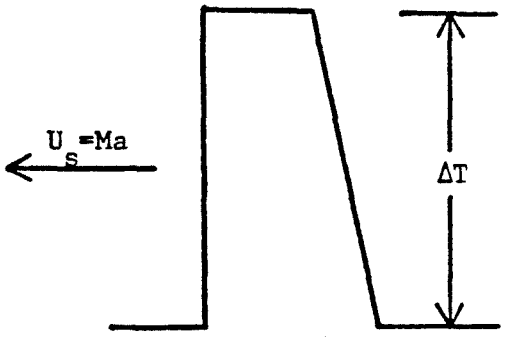

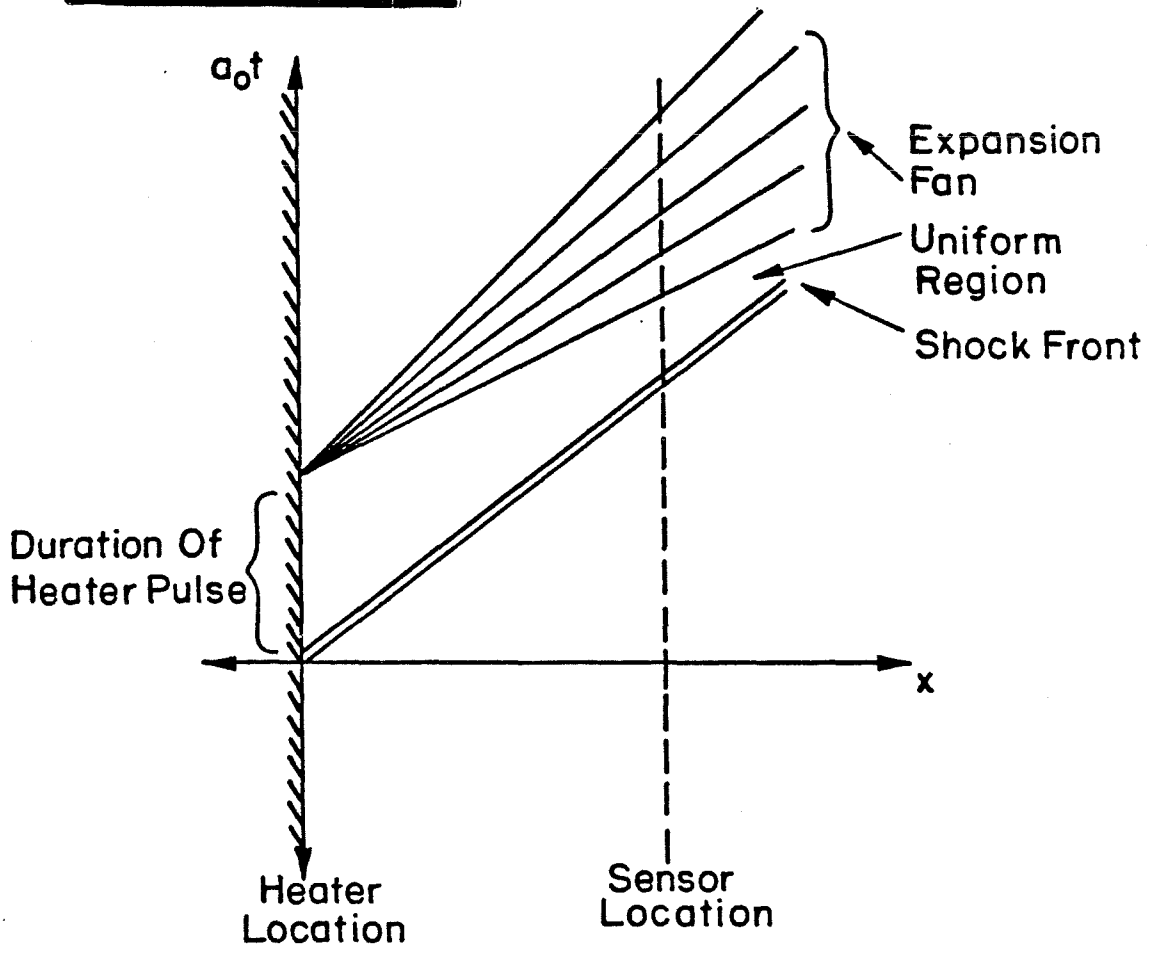

Figure 1.3. An initially rectangular heat pulse evolves into a shock front, a region of uniform counterflow, and an expansion fan.

of the pulse is preserved, the shock is fitted in so that the areas of the two lopped-off regions are equal (this also determines its velocity).

Figure 1.3 shows the evolution of a square pulse of heat propagating in superfluid helium when $B > 0$. The leading edge remains sharp, limited in steepness by balancing the nonlinear steepening with dissipation, but the trailing edge expands, the lowest point traveling at the unperturbed speed of second sound. The highest point travels faster than the shock by $\frac{1}{2}\beta a \frac{\Delta T}{T}$, and eventually catches up with it. At this time, referred to as the shock-expansion coincidence, the amplitude of the shock begins decreasing according to triangular wave decay, in which the area remains constant (Fig. 1.4).

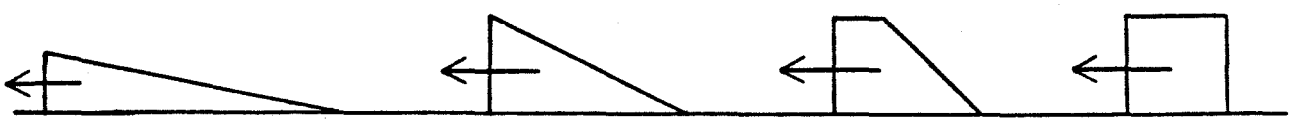

Figure 1.4. Regular decay of an initially square pulse.

It should be strongly emphasized that what has been said here is not exclusive to superfluid helium. Rather, it is valid for any type of weak wave with a linear relationship between the characteristic velocity and the perturbed quantity (ΔT for second sound in He II).

1.2. Breakdown Stages

It is important to keep in mind the fact that the points of the temperature profile propagate at their characteristic velocity without decaying (except for the triangular wave decay as mentioned). This provides a criterion for recognizing anomalous behavior in a second sound shock experiment.

A typical second sound shock experiment is described below. First, a point (p_0, T_0) in the pressure-temperature plane (see Fig. 1.5) is selected for the experiment.

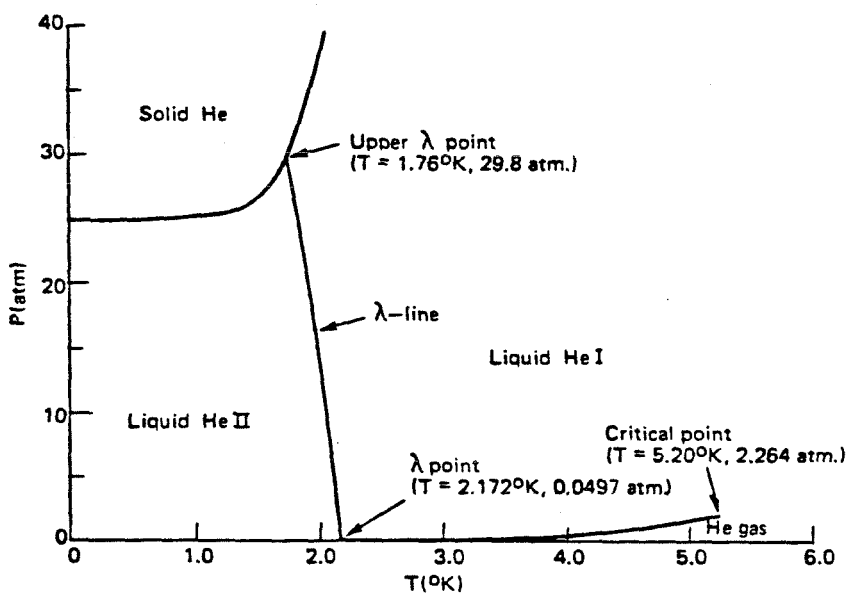

Figure 1.5. Phase diagram of helium (after Putterman, 1974).

Next, a rectangular voltage pulse is fired across the endwall heater, producing a rectangular heat pulse. This rectangular temperature profile propagates down the shock tube, evolving as discussed above, and is recorded at an endwall superconducting sensor (recall Fig. 1.3 and see Appendix C for a detailed description of the shock tube). Data taken include the arrival time, the temperature rise at the shock front, and a polaroid or digital recording of the entire pulse.

The arrival time is related to the average Mach number by

$$< M > = \frac{L}{a\ t_A} \tag{1.4}$$

where L is the shock tube length. Assuming that the pulse has not decayed while propagating, the average and instantaneous Mach numbers are equal, and the above relation may be combined with (1.3) to yield

$$\frac{1}{t_A} = \frac{a}{L}\left(1 + \frac{1}{2} B\ \frac{\Delta T}{T}\right) \tag{1.5}$$

where ΔT is the measured temperature jump. A slight difficulty arises in the application of this result. The shock tube length L is quite difficult to determine because of the differing cryogenic contraction of materials (for Turner's variable length second sound shock tube one can guess the length to no better than a few millimeters). However, Turner noted that as $\Delta T \rightarrow 0, \frac{1}{t_A} \rightarrow \frac{a}{L}$. A linear fit of $\frac{1}{t_A}$ *vs.* ΔT for a few points with small ΔT uniquely determines the intercept, which is $\frac{a}{L}$. Then for much larger ΔT, Turner verified (1.5), showing that the slope of $M-1$ vs. $\frac{\Delta T}{T}$ was $\frac{1}{2} B(p_0, T_0)$, as did Osborne (1951).

Figure 1.6 is a plot of $\frac{1}{2} B \frac{\Delta T}{T}$ *vs.* $M-1$ at $T = 1.609\ K$. The pressure is slightly larger than saturated vapor pressure due to the hydrostatic head of helium above the shock tube. With the data displayed in this way, the Khalatnikov solution falls along the 45° line. As the heater power is increased, the Mach number and temperature jump follow the Khalatnikov solution until $M \approx 1.03$. For larger heater powers, the data rapidly diverge from the theoretical

prediction. Exact numerical solutions to the jump conditions (Moody, 1983) show that this curvature results in part from higher order terms (see Fig. 1.7). However, the apparent retrograde effect (increasing heater power reduces shock strength and Mach number) around $M \approx 1.05$ is in no way explained.

It is useful to examine the waveforms produced in this experiment. Recall that for $T < 1.88\ K$ a rectangular temperature pulse will remain steep at the leading edge but flatten at the trailing edge. The region in between remains uniform. Indeed, in the experiment shown, this was found for low heater powers. As the Mach number neared 1.03, it was observed that the uniform region started to tilt (Fig. 1.8), indicating that some sort of decay had occurred. Moreover, a "warm tail" appeared following the pulse. Further increasing the heater power increased the tipping and raised the warm tail, obliterating the expansion fan. Finally a shock limit is reached, at which further increases of heater power lead only to reductions in shock strength and Mach number. It must be emphasized that the Mach number is an average value and that the temperature jump is what is measured at the sensor. The breakdown steps are slightly more complicated for a back-steepened shock and will not be discussed here.

1.3. Location of Decay Region

It has been stressed that second sound shock waves are useful for examining the fundamental critical velocity and associated dissipative mechanisms in the bulk fluid (away from walls). It therefore becomes necessary to find out whether dissipation occurs out in the bulk fluid or at the walls, primarily at the heater. If the dissipation is ongoing as the pulse propagates along the shock tube, the amplitudes of points on the profile would decrease monotonically with propagation distance. If the dissipation occurs in a thin region near the heater, the pulse would undergo all of its decay while passing through this region and propagate without suffering further decay thereafter.

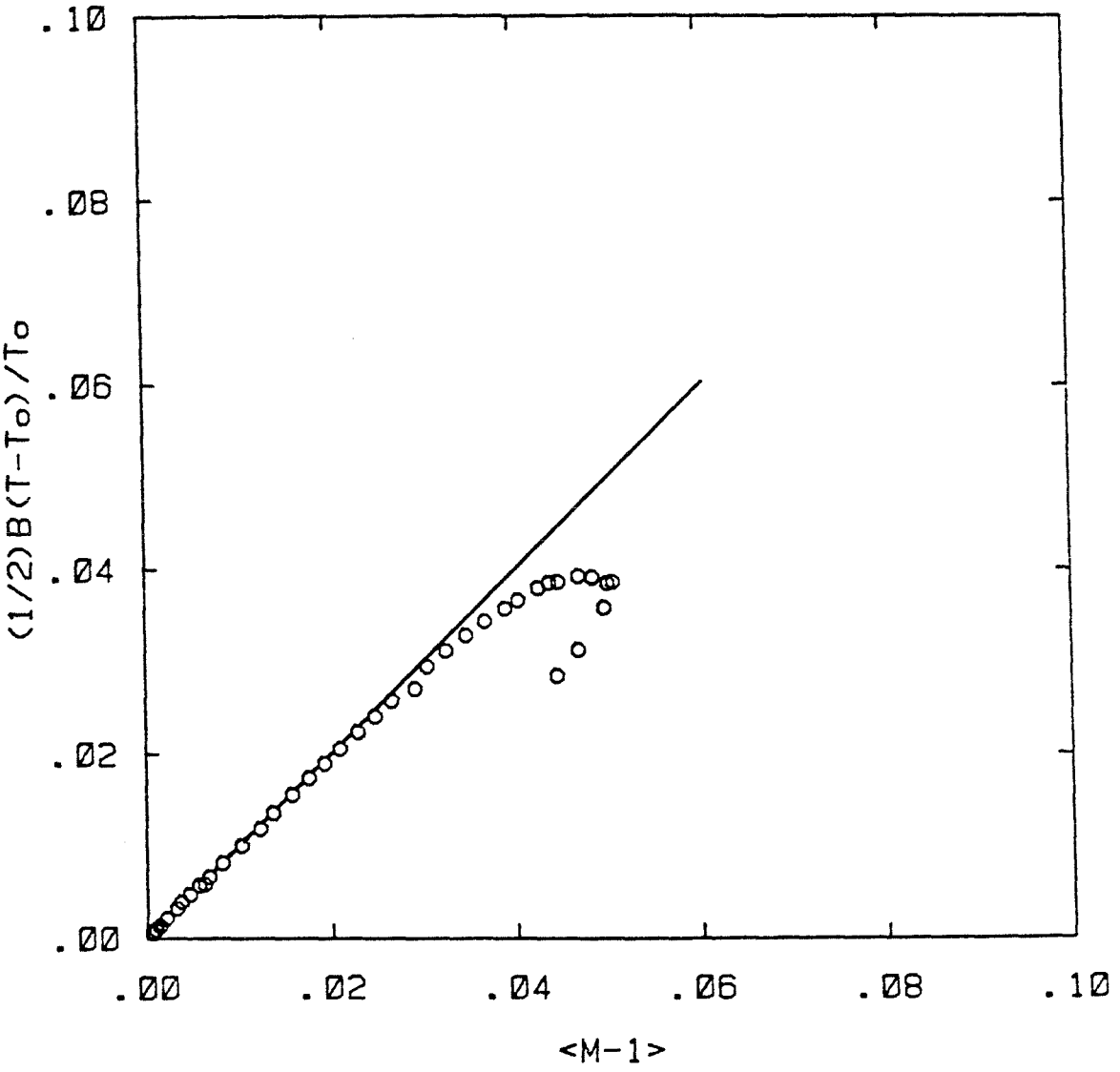

Figure 1.6. Scaled temperature jump vs. average Mach number at T = 1.609 K and p = s.v.p. (experiment H5). The line is the Khalatnikov solution.

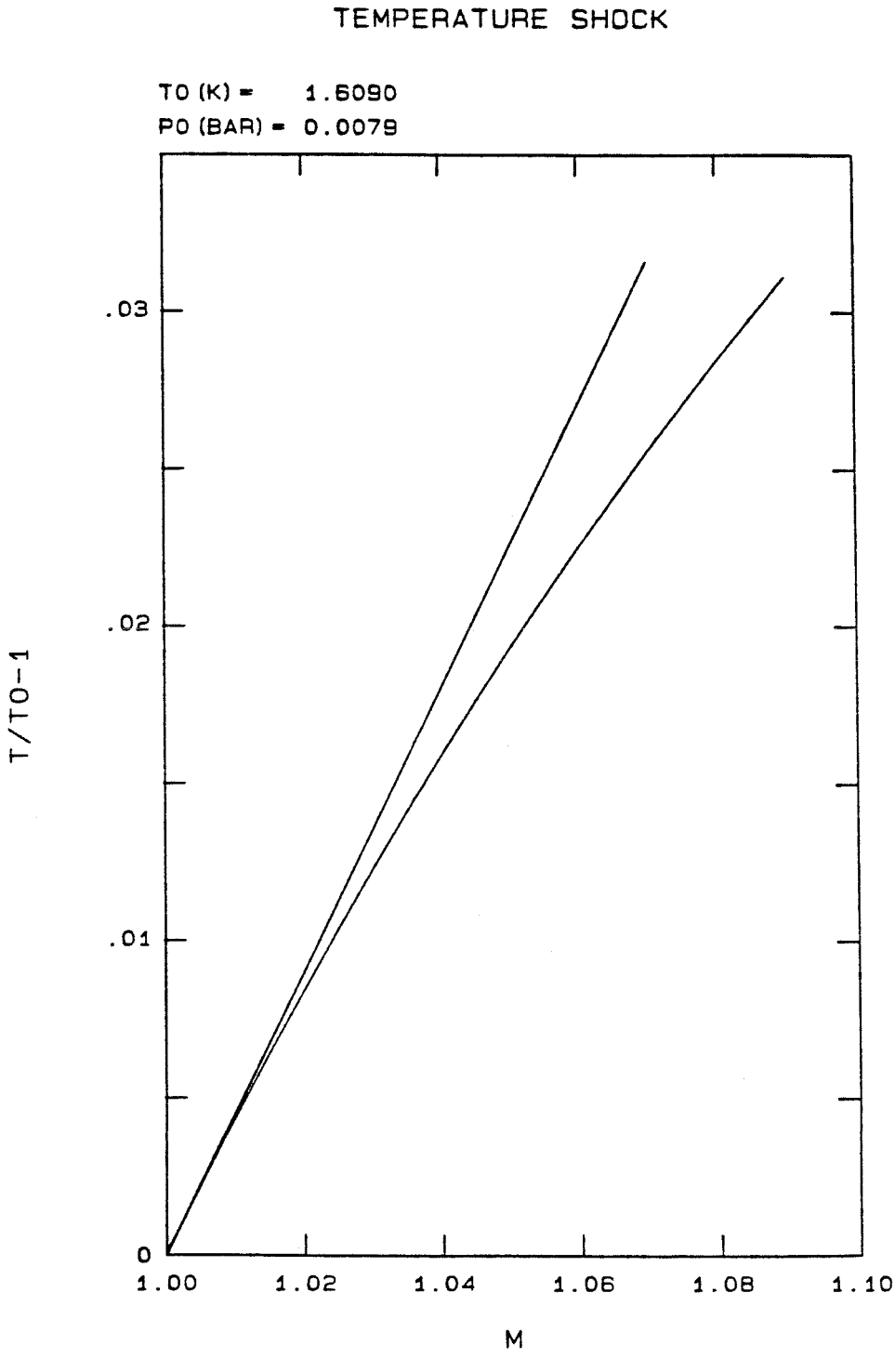

Figure 1.7. Numerical solution of jump conditions for experiment H5 (after Moody,1983). The straight line is the Khalatnikov solution.

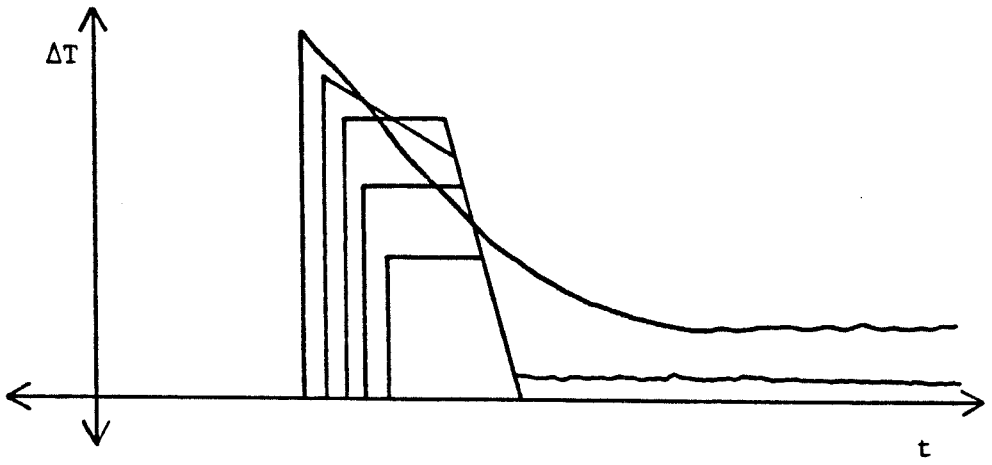

Figure 1.8. Variation of waveform with increasing heater power.

To examine this idea Turner used his variable length second sound shock tube (Turner, 1979) to observe the evolution of a decayed pulse. He found that even strongly decayed pulses did not decay further in amplitude while propagating. Note, however, that a wave with a tilted top does undergo the standard triangular wave decay typical of a shock-expansion coincidence. The significance of this result is that all of the limiting phenomena are occurring at or near the heater. In other words, the difficulty is getting heat into the fluid rather than propagating it by counterflow.

Chapter 2

THE FUNDAMENTAL CRITICAL VELOCITY

It has long been hypothesized that production of quantized vortices in the super component is responsible for the observed decay (Langer and Fisher, 1967). It is thought that, when the fundamental critical velocity is exceeded, vorticity (particularly quantized line and ring vortices) is produced in the super component. These vortices provide the means for momentum transfer between the normal and super components, so in their presence the relative velocity will decay. This momentum transfer occurs principally through the scattering of the excitations making up the normal fluid from the vortex core (Goodman, 1971).

2.1. Langer-Fisher Model

Langer and Fisher (1967) have put forth the idea that counterflow in superfluid helium should in some sense be considered a metastable state in much the same way that a supersaturated vapor is.

> For a given macroscopic sample of the metastable phase, there is a finite probablility per unit time for homogenous nucleation of the stable phase. But for a sufficiently small superflow (or supersaturation), this probability rate is too small to be observable, so the system appears to be stable. Conversely, the critical superflow (or supersaturation) is achieved when the probability of nucleation becomes appreciable within experimental times.

For the supersaturated vapor, the route to the stable phase involves the homogeneous nucleation of a droplet exceeding some critical size. This droplet then grows without bound. For counterflowing helium, the route to the "stable" state involves the production of a quantized ring vortex with radius exceeding

some critical radius, determined by the relative velocity. This vortex then grows and in a finite geometry is presumably annihilated at the walls, thus reducing the superfluid velocity.

Recall for a classical ring vortex of circulation κ , radius R, and core radius $a << R$ in an incompressible fluid of density ρ,

$$\textit{Energy}: \quad E_0 = \frac{1}{2}\kappa^2 \rho R \left[\ln \frac{8R}{a} - \frac{7}{4}\right] \tag{2.1}$$

$$\textit{Velocity}: \quad V_0 = \frac{\kappa}{4\pi R}\left[\ln \frac{8R}{a} - \frac{1}{4}\right] \tag{2.2}$$

$$\textit{Impulse}: \quad I_0 = \pi\kappa\rho R^2 \tag{2.3}$$

It should be noted in passing that these formulas are slightly dependent on a model for the core. In the above case a fluid-filled core in solid body rotation was assumed. Taking, for example, a hollow core vortex does not greatly affect (2.1) and (2.2). It is found that $7/4 \rightarrow 2$ in (2.1) and $1/4 \rightarrow 1/2$ in (2.2) (Putterman, 1974). Since in some sense the core radius is empirically determined, this slight difference is rather unimportant, changing most results by only a few percent.

Langer and Fisher consider a vortex ring in a uniform superflow $\vec{v}_s$. The energy of an excitation is just

$$E = E_0 + \vec{p}_0 \cdot \vec{v}_s \tag{2.4}$$

where E_0 is the "rest" energy of the vortex ring and $\vec{p}_0$ is the momentum added

to the flow by its creation. The momentum $\vec{p}_o$ of the vortex ring is calculated by Langer and Fisher in the following manner.

$$v_o = \frac{dE_o}{dp_o} = \frac{dE_o/dR}{dp_o/dR}, \tag{2.5}$$

so

$$\frac{dp_o}{dR} = \frac{1}{v_o}\frac{dE_o}{dR} \sim 2\pi\kappa\rho_s R \tag{2.6}$$

where the small logarithmic variations have been ignored. Note that integrating this relation yields

$$p_o = \pi\kappa\rho_s R^2 = I_o \tag{2.7}$$

which is the result for the impulse of the vortex ring.

Suppose such a vortex is traveling opposite to $\vec{v}_s$. Then it is found that

$$E(R) \approx \frac{1}{2}\kappa^2 \rho_s R\left[\ln\frac{8R}{a} - \frac{7}{4}\right] - \pi\kappa\rho_s R^2 v_s \tag{2.8}$$

Ignoring the logarithmic term as weak, one finds that $E(R)$ is quadratic in R with a maximum at some critical R_c. For $R > R_c$, $\frac{dE}{dR}$ is negative, so the vortex ring will grow outward, losing energy while doing so. If, on the other hand, $R < R_c$, the vortex ring will collapse to lose energy. R_c is found by setting $\frac{dE}{dR} = 0$.

$$\frac{dE}{dR} = \frac{dE_o}{dR} - v_s \frac{dp_o}{dR} = 0 \tag{2.9}$$

Comparing this with equation (2.5), it is seen that the critical radius is given by $v_s = v_o(R_c)$.

$$v_s = \frac{\kappa}{4\pi R_c}\left(\ln \frac{8R_c}{a} - \frac{1}{4}\right) \tag{2.10}$$

So according to the Langer-Fisher argument, production of a vortex ring of radius R_c as given above will allow reduction of v_s.

It is hypothesized that these rings are homogeneously nucleated by fluctuations in the fluid. Due to their scarcity, the Boltzmann distribution function $e^{-E/kT}$ is used to describe the probability of ring production. In order to produce a ring of radius R_c or larger,

$$E_o(R_c) \sim kT \tag{2.11}$$

Again ignoring the logarithmic dependences, this result yields:

$$v_{s,c} \approx \frac{\kappa^3 \rho_s}{8\pi kT} f\ (R_c) \tag{2.12}$$

where f is a weak logarithmic function of R_c . What is important to notice is that the critical velocity $v_{s,c} \propto \frac{\rho_s}{T}$.

2.2. Results of Critical Velocity Experiments

The Langer-Fisher theory produces a result $v_{s,c} \propto \frac{\rho_s}{T}$, a relation easily checked experimentally. Figure 2.1 shows shows results from two very different sorts of experiments. The first, included for comparison, employs pressure-driven superflow (Notarys, 1969). Notarys forced superfluid helium through mica sheet with small pores (typically 800 Å or less in diameter) and measured the superfluid velocity produced with a $1\mu m$ pressure difference. He found that $v_{s,c} \propto \frac{\rho_s}{T}$, with the appropriate numerical constant multiplying $\frac{\rho_s}{T}$ about an order of magnitude lower than predicted by the Langer-Fisher theory.

The second experiment involved measuring the maximum counterflow velocity produced by a second sound shock, following Turner's technique. Results from many such experiments closely follow the predicted $\frac{\rho_s}{T}$ functional dependence for w_m. The fact that the two numerical constants obtained are not the same is not significant since in both cases arbitrary (but easily reproducible) criteria were selected to determine the "critical" velocity.

2.3. Problems with Langer-Fisher Theory

Both experimental and theoretical considerations pose difficulties for the Langer-Fisher theory although, interestingly enough, both experiments give the required $\frac{\rho_s}{T}$ dependence for the critical velocity. Notarys notes an obvious shortcoming of the Langer-Fisher theory — in many cases the presumed vortex rings are larger than the pore size through which the super component flows. His conclusion from this observation is that although the vortex rings in the pores are quantitatively different from free rings, they are qualitatively the same. Second sound shock experiments show that the decay occurs only near the heater wall, not out in the bulk fluid, where one envisions the Langer-Fisher

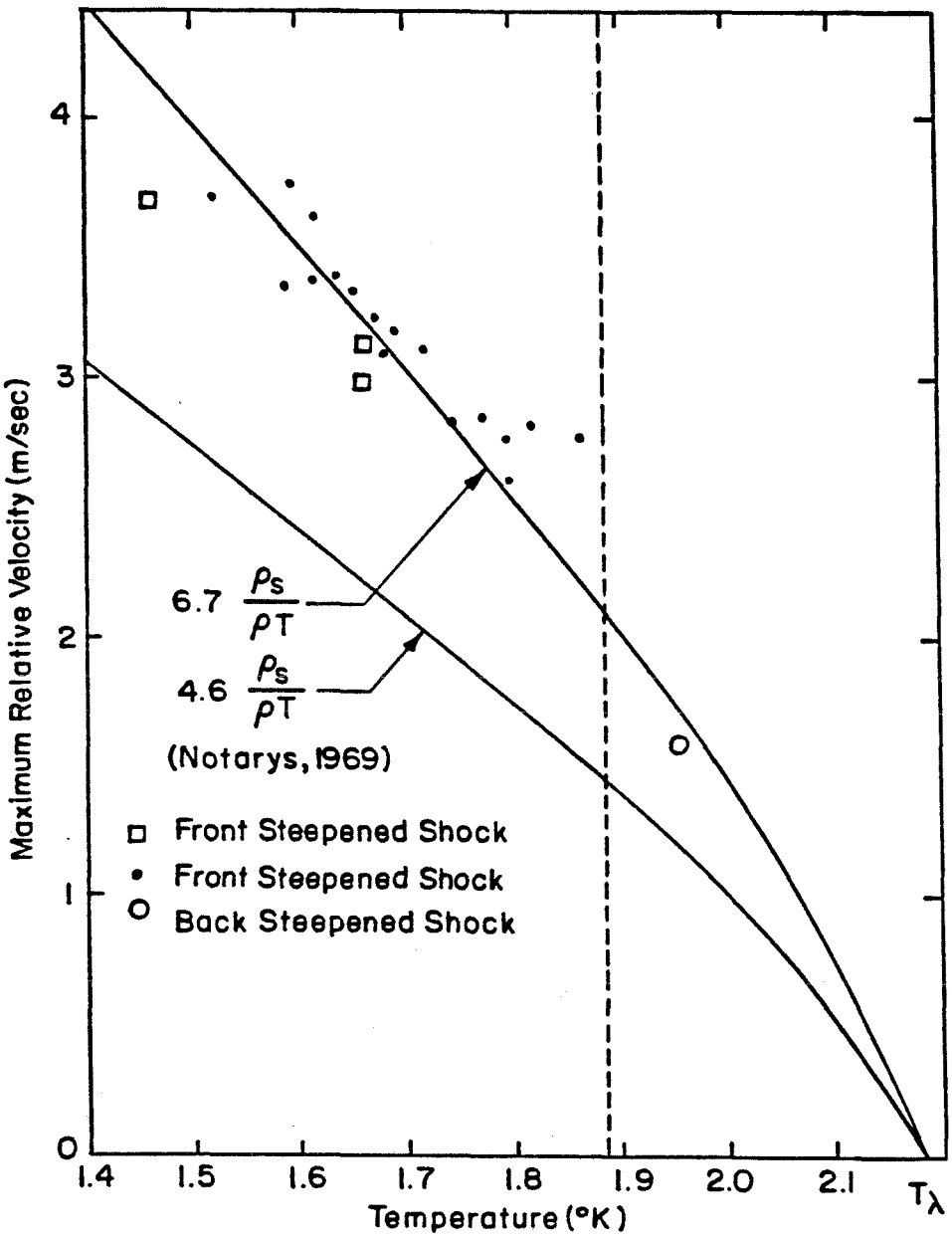

Figure 2.1. Temperature dependence of the maximum relative velocity. Open symbols are Turner's data (1979). Notarys' data (1969) are included for comparison.

model as being most applicable. In both cases the presence of solid boundaries (the pores in the mica or the endwall heater) are connected with the observed decay.

A simple scaling argument suggests why this is so. Near a wall, the superfluid density goes smoothly to zero (see Fig. 2.2) over some characteristic length, called the healing length (Tilley and Tilley, 1974).

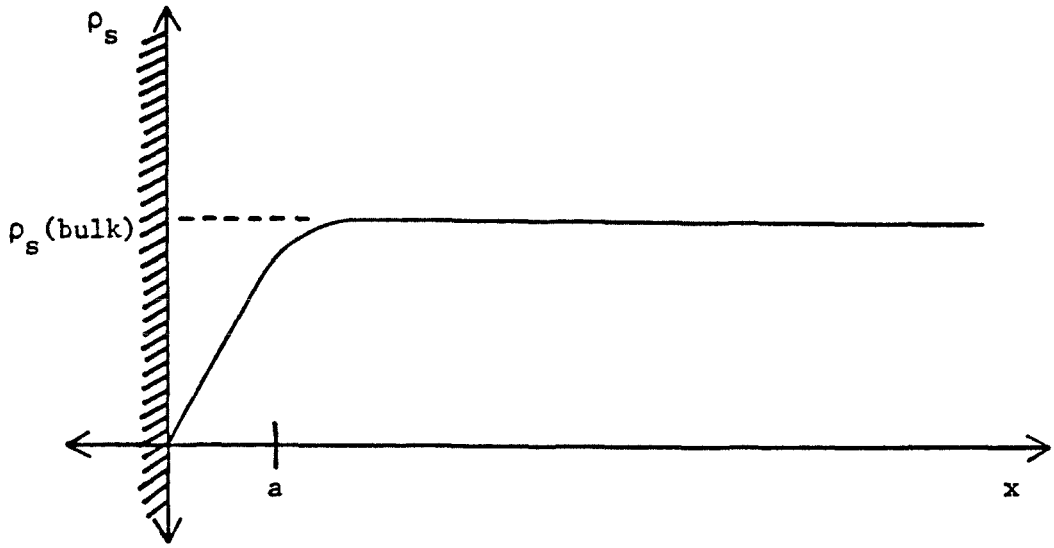

Figure 2.2 Variations of ρ_s near a wall.

To produce vorticity near a wall, we expect from dimensional analysis that

$$2\pi w_c a \sim \kappa = \frac{h}{m_4} \tag{2.13}$$

where w_c is the critical relative velocity. Experimentally it is found that

$$a \approx \left[0.243\times10^{-8}\ \frac{gm}{cm^{2\circ}K}\right]\frac{T}{\rho_s} \approx \left[\frac{m_4}{\hbar}\right]^2 \frac{k_B T}{2\rho_s} \tag{2.14}$$

over a wide range of temperatures and pressures (Putterman, 1974). Combining

these two results yields:

$$w_c \sim \left[6.5\times10^4 \frac{cm-^\circ K}{sec-gm}\right] \frac{\rho_s}{T} = \left[94 \frac{m-^\circ K}{sec}\right] \frac{\rho_s}{\rho T} \tag{2.15}$$

Thus, again it is seen that $w_c \propto \frac{\rho_s}{T}$, the Langer-Fisher result, when the process is occurring near solid boundaries. Again the numerical factor is an order of magnitude larger than observed.

The Langer-Fisher analysis runs into more serious problems when looked at theoretically. Of chief concern is the use of the impulse I_0 required to produce a vortex ring for the momentum p_0. Consider for a moment a vortex ring with a fluid-filled core (ffc) in a large box (not a domain of infinite extent) of incompressible fluid. The momentum of this excitation is given by:

$$\vec{p}_{ffc} = \int\int_{box}\int \rho\vec{v}\ dV = \rho V_{box}\vec{v}_{box} \tag{2.16}$$

so if the box is stationary, the momentum of such an excitation is zero (Wilks, 1967). Consider a hollow core vortex ring in a stationary box.

$$\vec{p}_{hollow} = \int\int_{box}\int \rho\vec{v}\ dV = \rho(V_{box}\ \vec{v}_{box} - V_{ring}\ \vec{v}_{ring}) \tag{2.17}$$

$$= -\rho\ V_{ring}\ \vec{v}_{ring}$$

Now $V_{ring} \sim 2\pi^2 a^2 R$ and $v_{ring} \sim \frac{\kappa}{4\pi R}$. Thus, $p_{hollow} \sim -\kappa\rho a^2$.

$$\frac{p_{hollow}}{I_{hollow}} \sim \left(\frac{a}{R}\right)^2 \tag{2.18}$$

Thus, the momentum of the ring is smaller than the impulse of the ring by a factor of $(a/R)^2$, which is quite small. One may well wonder what has happened to the impulse originally used to create the ring. Clearly the momentum has propagated to the walls of the box, which absorb it. This propagation occurs at the speed of sound (which in our case is effectively infinite — compressibility is assumed to be unimportant). Therefore, no energy maximum exists now since

$$p_0 \sim \pi\kappa\rho_s a^2 \tag{2.19}$$

$$E \sim \frac{1}{2}\pi^2 \rho_s R \left[\ln \frac{8R}{a} - \frac{7}{4}\right] - \pi\kappa\rho_s a^2 v_s \tag{2.20}$$

which is monotonic increasing in R. Reversing the Langer-Fisher argument, we conclude that counterflowing helium is not metastable in the *same* way that a supersaturated vapor is.

2.4. Mutual Friction

Although the Langer-Fisher theory breaks down under close scrutiny, it is not necessary to abandon the idea that quantized vortices play a crucial role in momentum exchange between normal and super components. Rather, one must look for interactions between the vortices and normal component that may cause vortices to grow or distort at the expense of the normal component. Such an interaction, known as mutual friction, has been postulated to occur between the normal fluid and has been used quite successfully to interpret experimental

results (Hall and Vinen, 1956). An interaction force of the form

$$\vec{F}_{ns} = B \frac{\rho_s \rho_n}{2\rho} \frac{\vec{\omega}_s \times (\vec{\omega}_s \times \vec{w})}{\omega_s} + B' \frac{\rho_s \rho_n}{2\rho} \vec{\omega}_s \times \vec{w} \qquad (2.21)$$

works to reduce the relative velocity w ($\vec{F}_{ns}$ acts on the normal component while $-\vec{F}_{ns}$ acts on the super component). Here B and B' are the coefficients of mutual friction, weak functions of the thermodynamic state. Also, $\vec{\omega}_s = < \nabla \times \vec{v}_s >$, where the average is taken over a region of space large compared to the vortex spacing but small compared to the scale on which that spacing changes.

This force seems to result from the scattering of excitations (mainly rotons for $T > 1.2\ K$) comprising the normal component from quantized superfluid vortices and has been studied numerically (Goodman, 1971). It was found that the scattering was asymmetric with respect to the forward direction as expected (see Fig. 2.3). In fact, some rotons interacted with the vortex by very nearly reversing their trajectories (referred to as a "snap-back" by Goodman). Analysis of many scattering events allowed the calculation of B and B', which agree reasonably well with experimental results.

Applying the mutual friction idea to a single quantized vortex line, one finds the force per unit length to be given by

$$\vec{f} = D \rho_s \kappa \hat{\kappa} \times (\hat{\kappa} \times (\vec{v}_L - \vec{v}_n)) + D' \rho_s \kappa \hat{\kappa} \times (\vec{v}_L - \vec{v}_n) \qquad (2.22)$$

where D and D' are dimensionless, $\hat{\kappa}$ is the unit vector tangent to the vortex, and $\vec{v}_L$ is the vortex velocity. Note that $\vec{v}_L \neq < \vec{v}_s >$, the mean superfluid velocity at the core. Therefore, this vortex will experience another force arising from

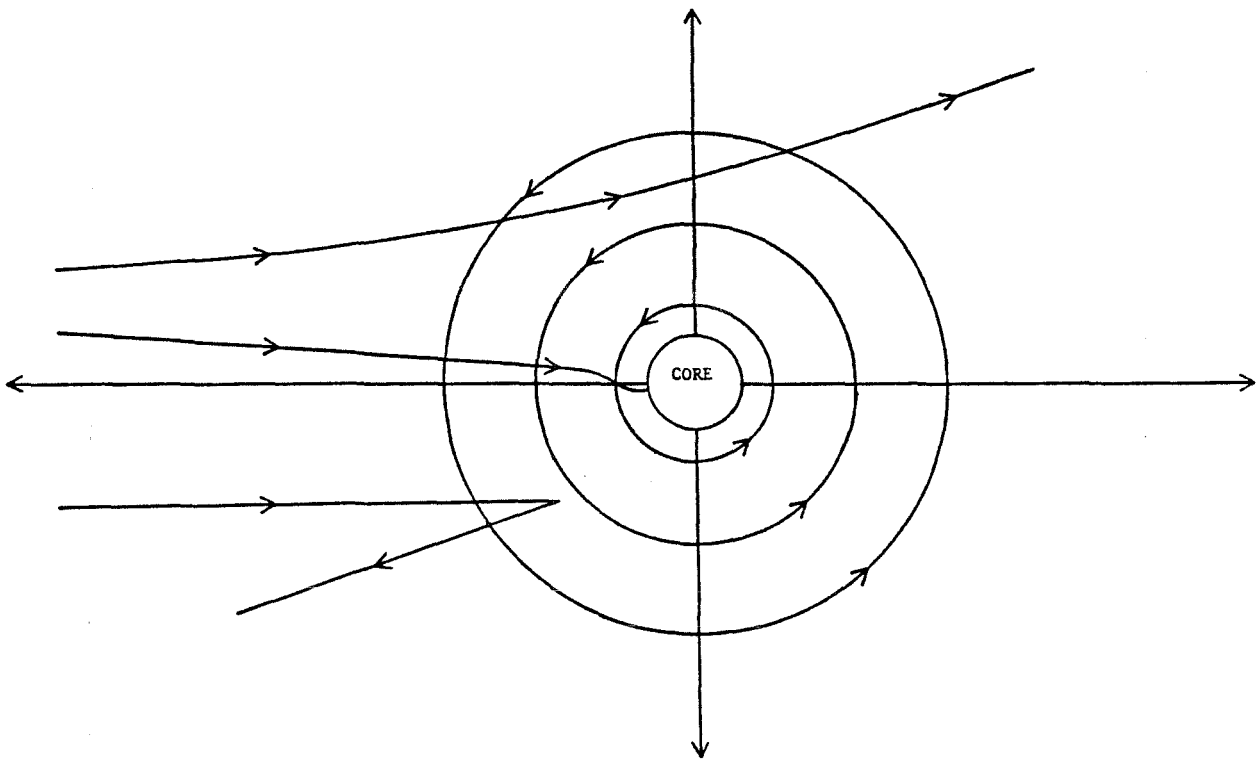

Figure 2.3. Typical roton trajectories (after Goodman, 1971).

the interaction of its circulation and the mean superfluid velocity

$$\vec{f}_m = \rho_s(\vec{v}_s - \vec{v}_L) \times \vec{\kappa} \tag{2.23}$$

which is the Magnus force (or lift). To relate these two forces it is assumed that there are no unbalanced forces.

$$\vec{f} + \vec{f}_m = 0. \tag{2.24}$$

2.5. A Simple Vortex Model of Breakdown

Before facing up to the three-dimensional problem of vortex rings, we consider first a two-dimensional problem in which there exist a finite number of parallel line vortices all of circulation $\pm\kappa$. An equation of motion will be deduced from the force balancing principle of the previous section (Turner, private communication). These equations will then be solved exactly for a simple model problem, demonstrating the breakdown mechanism.

Suppose this collection of vortices is in a counterflow w. Writing the force balance for each line yields the following set of equations describing the vortices' motion.

$$(\vec{v}_{Lj} - \vec{v}_{nj})(1 + D') = (\vec{v}_{sj} - \vec{v}_{nj}) - D\hat{\kappa}_j \times (\vec{v}_{Lj} - \vec{v}_{nj}). \tag{2.25}$$

Note that $\vec{v}_{sj} - \vec{v}_{nj} \neq -\vec{w}_j$ but also contains the velocity induced on the j^{th} vortex by each of the other vortices. The form of equation (2.25) suggests that the logical (local) frame of reference to use in studying these equations is the frame moving with $\vec{v}_{nj}$. Redefining the variables leads to the following equations.

$$\vec{v}_j = \vec{v}_{Lj} - \vec{v}_{nj} \tag{2.26}$$

$$\vec{u}_j = \vec{v}_{sj} - \vec{v}_{nj} \tag{2.27}$$

$$\vec{v}_j\,(1+D') = \vec{u}_j - D\hat{\kappa}_j \times \vec{v}_j \tag{2.28}$$

These equations are much more easily solved using complex variables rather than vector formalism. Let the position of each vortex be z_j. Then its velocity $v_j = \dot{z}_j$ and

$$\dot{z}_j\,(1+D' + iD\ sgn(\kappa_j)) = u_j \tag{2.29}$$

where u_j is found by superimposing the background superflow $-w_j$ with the induced flow from the other vortices.

$$\dot{z}_j\,(1+D' + iD\ sgn\ (\kappa_j)) = -w_j + \frac{i\kappa}{2\pi}\sum_{m\neq j}\frac{sgn(\kappa_m)}{\bar{z}_j - \bar{z}_m} \tag{2.30}$$

The two-dimensional analog to a vortex ring is a pair of counter-rotating line vortices. In this case, the two coupled equations reduce to

$$\dot{z}_1\,(1+D' + iD) = -w - \frac{i\kappa}{2\pi}\frac{1}{\bar{z}_1 - \bar{z}_2} \tag{2.31}$$

$$\dot{z}_2\,(1+D' - iD) = -w + \frac{i\kappa}{2\pi}\frac{1}{\bar{z}_2 - \bar{z}_1} \tag{2.32}$$

Call $z_c = \frac{1}{2}(z_1 + z_2)$ and $z_R = \frac{i}{2}(z_2 - z_1)$. Thus, z_c is the motion of the "center of vorticity," while z_R describes the relative motion (see Fig. 2.4). Note here $z_c = re^{i\varphi}$ and $z_R = \mathrm{Re}^{i\theta}$, so θ is the direction that the "ring" points.

$$(1 + D')\,\dot{z}_c - D\,\dot{z}_R = -w + \frac{\kappa}{4\pi\bar{z}_R} \tag{2.33}$$

$$D\,\dot{z}_c + (1 + D')\dot{z}_R = 0 \tag{2.34}$$

Eliminating $\dot{z}_c$ and rescaling the time yields

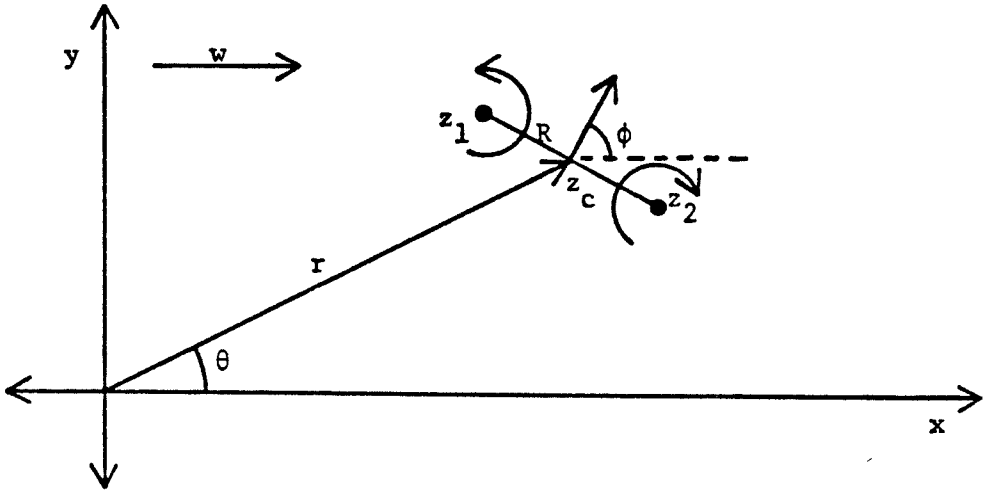

Figure 2.4 Two-dimensional analog of a vortex ring.

$$\frac{dz_R}{ds} = w - \frac{\kappa}{4\pi \bar{z}_R} \tag{2.35}$$

where

$$s = \frac{D}{(1+D')^2 + D^2} t \tag{2.36}$$

increases with time since $D > 0$ (it is the drag).

Using the polar form for z_R allows the separation of equations (2.34) into real and imaginary parts.

$$\frac{dR}{ds} = w\cos\Theta - \frac{\kappa}{4\pi R} \tag{2.37}$$

$$R\,\frac{d\Theta}{ds} = -w\sin\Theta \tag{2.38}$$

The time variable s does not appear explicitly in the equations, so it can be eliminated to give a phase plane equation.

$$\frac{1}{R}\frac{dR}{d\Theta} = \frac{\frac{\kappa}{4\pi w R} - \cos\Theta}{\sin\Theta}. \tag{2.39}$$

This may be solved analytically to yield

$$R\sin\Theta - R_o \sin\Theta_o = \frac{\kappa}{4\pi w}(\Theta - \Theta_o) \tag{2.40}$$

where R_o and Θ_o are the initial conditions.

Figure 2.5 shows a phase plane plot of these trajectories with R scaled by R_c where

$$R_c = \frac{\kappa}{4\pi w}. \tag{2.41}$$

Note that this is analogous to uniform flow and a potential sink. If a line pair is generated with initial conditions within the separatrix, it will collapse into the sink ($R \to 0$ as t increases). However, if it is created with initial conditions lying outside the separatrix, it will ultimately expand along one of the trajectories with $R \to \infty$ and $\Theta \to 0$. Note w is chosen positive, so the vortex pair is opposing the counterflow, and the flow decays as a result. Furthermore, any vortex pair with $R_o < R_c$ will collapse. Thus, it is the creation of vortex pairs of $R_o > R_c$ that will lead to decay of superflow.

Solving the above problem for a vortex ring rather than a vortex pair is quite difficult since the ring will certainly distort from its plane circular form as it

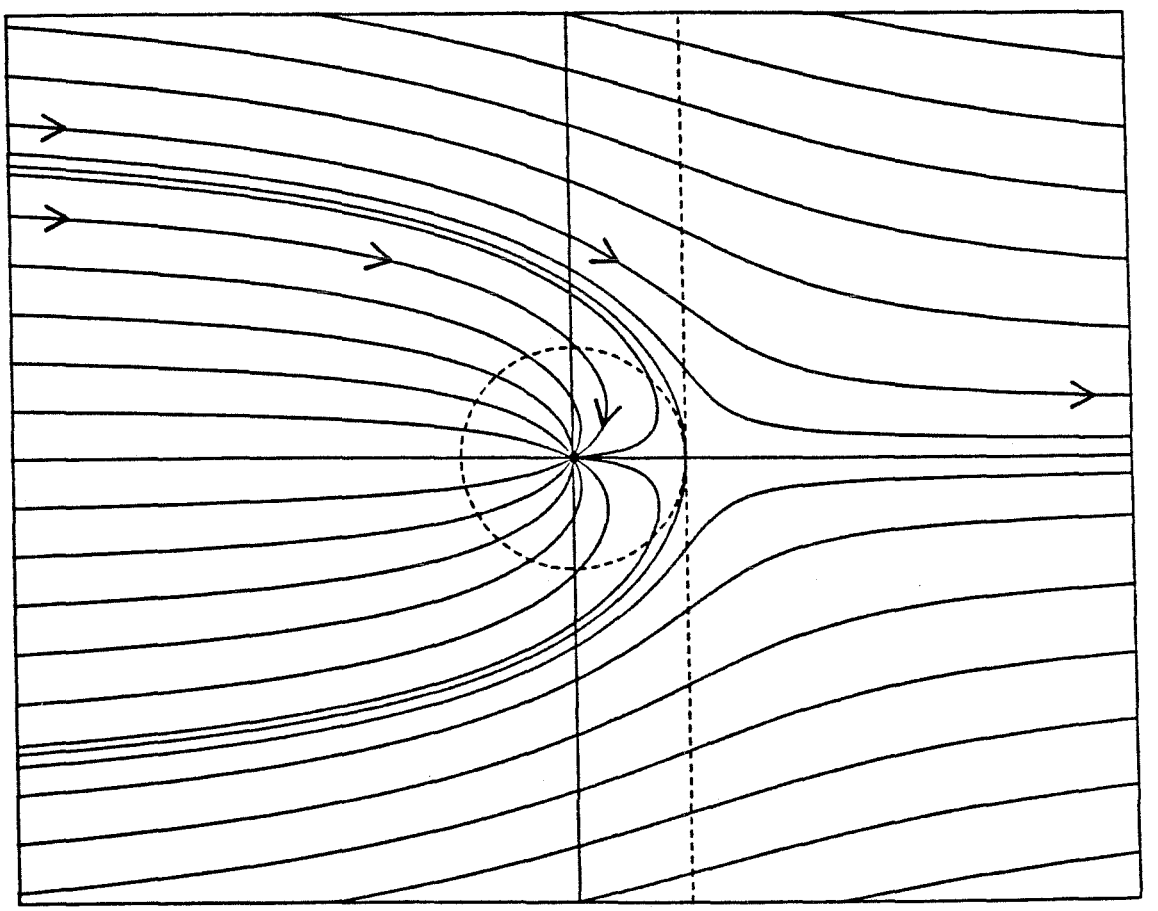

Figure 2.5. Phase space of vortex pair "trajectories". The flow in time is from left to right and into the sink. All initial states with $R<R_c$ (dashed circle) collapse. Initial states outside of the separatrix grow without bound (after crossing the dashed line).

evolves. One would have to solve equations such as (2.25) numerically for small elements of the vortex ring, at each step using the Biot-Savart law to determine the induced superfluid velocity from each element. This procedure would be cumbersome and not very enlightening. One case, however, due to high symmetry may be solved almost exactly (see Fig. 2.6).

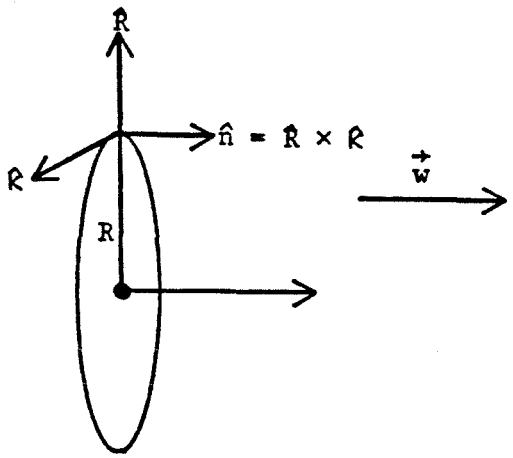

Figure 2.6. A circular vortex ring propagating along a uniform counterflow (against the super component).

It is suggested (Wilks, 1967) that a curvature force must be included in the force balance of equation (2.24).

$$\vec{f}_c = -\frac{\beta(R)\rho_s\kappa^2}{4\pi R}\hat{R} \tag{2.42}$$

Here $\beta(R)$ is a weak, positive, monotonic increasing function of R. Weak is taken to mean $\frac{\beta(R)}{R} \to 0$ as $R \to \infty$. Following the same approach as above yields

$$\frac{dR}{ds} = w - \frac{f(R)\kappa}{4\pi R} \tag{2.43}$$

where

$$f(R) = \beta(R) + \ln\left[\frac{8R}{ae^{1/4}}\right] \tag{2.44}$$

For R_o such that $w > \frac{f(R_o)\kappa}{4\pi R_o}$, the vortex ring will grow without bound, and for $w < \frac{f(R_o)\kappa}{4\pi R_o}$, the ring will collapse, transferring no momentum. So in this case a critical radius arises.

$$\frac{f(R_c)\kappa}{4\pi R_c} = w \tag{2.45}$$

If thermal fluctuations are the source of such vortex rings, to generate an appreciable number in the flow requires

$$E(R_c) = \frac{1}{2}\rho_s \kappa^2 R_c \left[\ln\frac{8R_c}{a} - \frac{7}{4}\right] \sim kT. \tag{2.46}$$

Neglecting logarithmic dependences leads to the following

$$w_c = A\,\frac{\rho_s}{T} \tag{2.47}$$

where A is a numerical constant determined primarily by how much smaller $E(R_c)$ must be than kT. The important observation to make is that vortex dynamics yields a critical velocity of the proper thermodynamic dependence.

2.6. Vortices Near Walls

Another observation to note is that this vortex model of breakdown predicts a vortex-free region in the vicinity of walls when counterflow is taking place. Consider a line vortex next to an infinite planar wall (see Fig. 2.7).

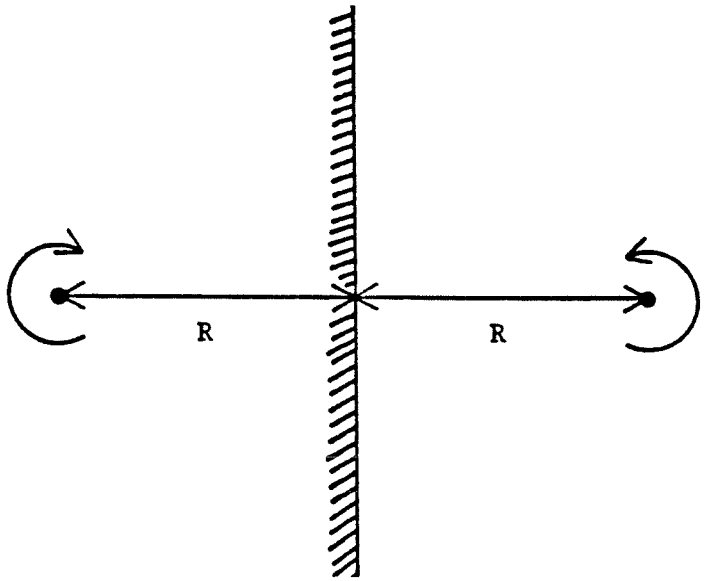

Figure 2.7. A vortex of circulation κ at distance R from a wall. The image vortex is shown at its (virtual) location.

If an adiabatic wall is assumed, $\vec{v}_s$ must be parallel to the wall at all points. This boundary condition is satisfied by placing an image vortex of opposite circulation equidistant from the wall along the normal. This forces the wall to be a streamline for the flow, and hence the wall itself may be removed from further consideration.

We now have the case that has been discussed above and solved completely, a vortex line pair. If $R < R_c = \frac{\kappa}{4\pi w}$, the vortex pair will collapse. Therefore, if $R < \frac{\kappa}{4\pi w}$, the vortex will collide with the wall and be annihilated. It is instructive to examine a few numerical values. For $w = 1 \frac{m}{sec}$, $R_c = 80\text{Å}$, which is much greater than the core radius. This distance should be compared to the thickness of the normal fluid boundary layer created following a shock.

$$\delta_n \sim \left[\frac{\nu_n x}{v_n}\right]^{\frac{1}{2}} \tag{2.50}$$

Looking 1 cm behind a shock producing a relative velocity of $1\frac{m}{sec}$, $\delta_n \sim 30\ \mu m$. Thus,

$$\frac{R_c}{\delta_n} \sim 10^{-4}.$$

Therefore, for most counterflow processes, $\vec{w}_{wall} \approx -\vec{v}_s$, which is less than the free stream value for $\vec{w}$ by a factor of $\frac{\rho_n}{\rho}$. Thus, R_c is increased by a factor of roughly $\frac{\rho}{\rho_n}$. It is in this manner that a vortex line near a wall is absorbed.

Chapter 3

SUCCESSIVE SHOCK EXPERIMENTS

3.1. Flow Disturbances Produced by a Shock

It has been shown in previous sections that the presence of quantized vortices permits momentum exchange between the normal and super components (breakdown). To examine this idea, it is useful to study the flows behind shocks to see whether any such excitations remain in the fluid. One way to do this is to probe the shock-processed fluid with another shock wave. In this way it is possible to see whether the second (successive) shock will be modified in any way by excitations produced by the initial shock.

A typical experiment takes place in the following manner. A shock pulse of prescribed amplitude and duration is fired and travels along the shock tube. After a certain time interval (the separation time t_s), a second shock pulse identical to the first is fired. The two profiles are recorded digitally when they are received at an endwall sensor located at a fixed distance from the heater. The separation time t_s is varied, and the resulting profiles are compared. It turns out that effects in such experiments are most dramatically displayed for shocks at the breakpoint, the strength at which arrival times begin to deviate from the Khalatnikov prediction. For significantly weaker shocks the effects are negligible.

Shown in Figure 3.1 are the results from one such experiment. For separation times greater than a few minutes, the profiles of the initial and successive shocks are indistinguishable. However, as the separation time is reduced, the profile of the successive shock takes on the appearance of a profile having

undergone breakdown. With t_s around 10 seconds, it is observed that the region of uniform counterflow has decayed (it appears tilted). This decay increases monotonically with decreasing t_s, and the profile changes curvature from convex to concave. Following behind the shock pulse is a warm tail, in which the geometric noise (see Appendix D) is smoothed out. As t_s is reduced, this warm tail rises rapidly to an asymptotic level. Further reductions in t_s do not affect the tail although the tilting continues to increase.

In light of the vortex model for breakdown, this result is interpreted as follows. The initial shock produces some sort of excitations in the fluid, presumably quantized line and ring vortices. Some of them remain in the fluid long after the initial shock pulse has decayed (decay time for shocks is typically on the order of 20 msec). The successive shock interacts with these vortices already present in the flow since their presence allows exchange of momentum between the components and generation of additional vorticity (see Chapter 4). Thus, decay for the successive shock is greatly enhanced.

3.2. Location of Disturbances in the Fluid

It is possible to use successive shock experiments to study the spatial distribution of these disturbances in the shock tube. If the disturbances are distributed uniformly throughout the shock tube, then the decay will be ongoing, and the points of the temperature profile should decrease in amplitude as the wave propagates. If the disturbances are localized, then the decay regions will be similarly localized. In this way, observing the evolution of the successive shock will reveal the distribution of disturbances in the fluid.

To observe this profile evolution, the variable length second sound shock tube (Turner, 1979) was used. This shock tube is conceptually similar to the shock tube described in Appendix C except that the endwall sensor may be positioned from 2 to 20 cm from the heater. Although it is not possible to observe the

evolution of a single pulse with this shock tube, it can be used to view identical waves at different locations along the shock tube. With the sensor at a fixed location, a successive shock experiment is run as described above. After recording the successive shock profiles for a variety of separation times, the endwall sensor is moved to a new position along the shock tube. Another successive shock experiment is done at this station as above with all other conditions unchanged. In this way, the wave profiles may be observed at many locations along the tube.

Figures 3.2-4 show a few results from such an experiment. The three sensor locations are at 7.2 cm, 9.6 cm, and 14.4 cm with separation times of 20 seconds. Note that the expected nonlinear evolution of the profile is observed (the expansion fan broadens, for example). A convenient point on the profile to examine for amplitude decay is the corner point on the expansion, indicated by small arrows in the figures. After comparing these three cases, it is seen that the amplitude of this point is unchanged to within experimental error. Similarly, in all cases examined experimentally, it is found that the pulses do not decay while propagating between stations. Thus, the results show that these disturbances are confined to a region near the heater and decay before getting more than a few diameters away.

The successive shock technique provides a powerful method with which to study the spatial distribution of this disturbance layer as a function of time, by varying both sensor location and separation time. The principal conclusions are threefold. A shock near the breakpoint produces disturbances in the fluid. A second shock passing through these disturbances undergoes enhanced decay. These disturbances have lifetimes on the order of minutes, remain near the heater, and probably have vortical character.

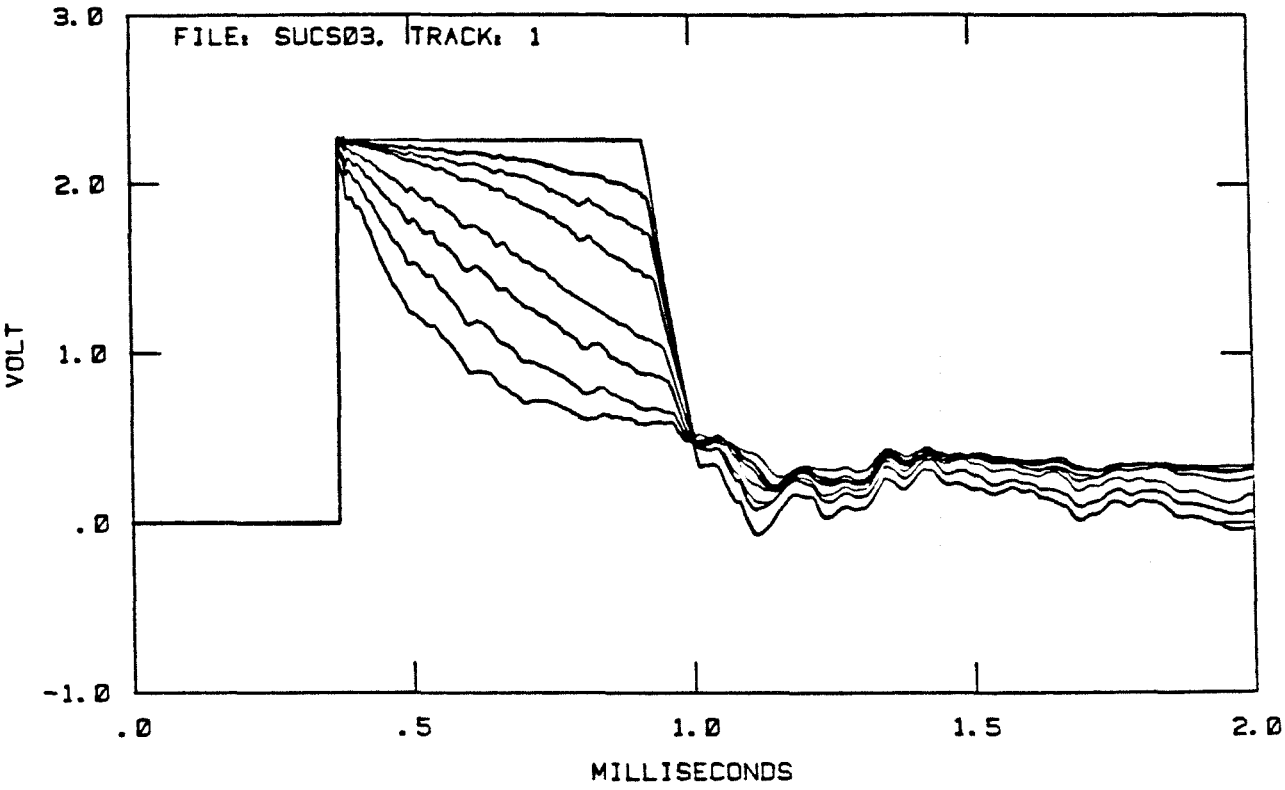

Figure 3.1. Successive shock data for separation times ∞, 20, 10, 5, 2, 1, 0.5, and 0.2 seconds. The decay increases as the separation time decreases.

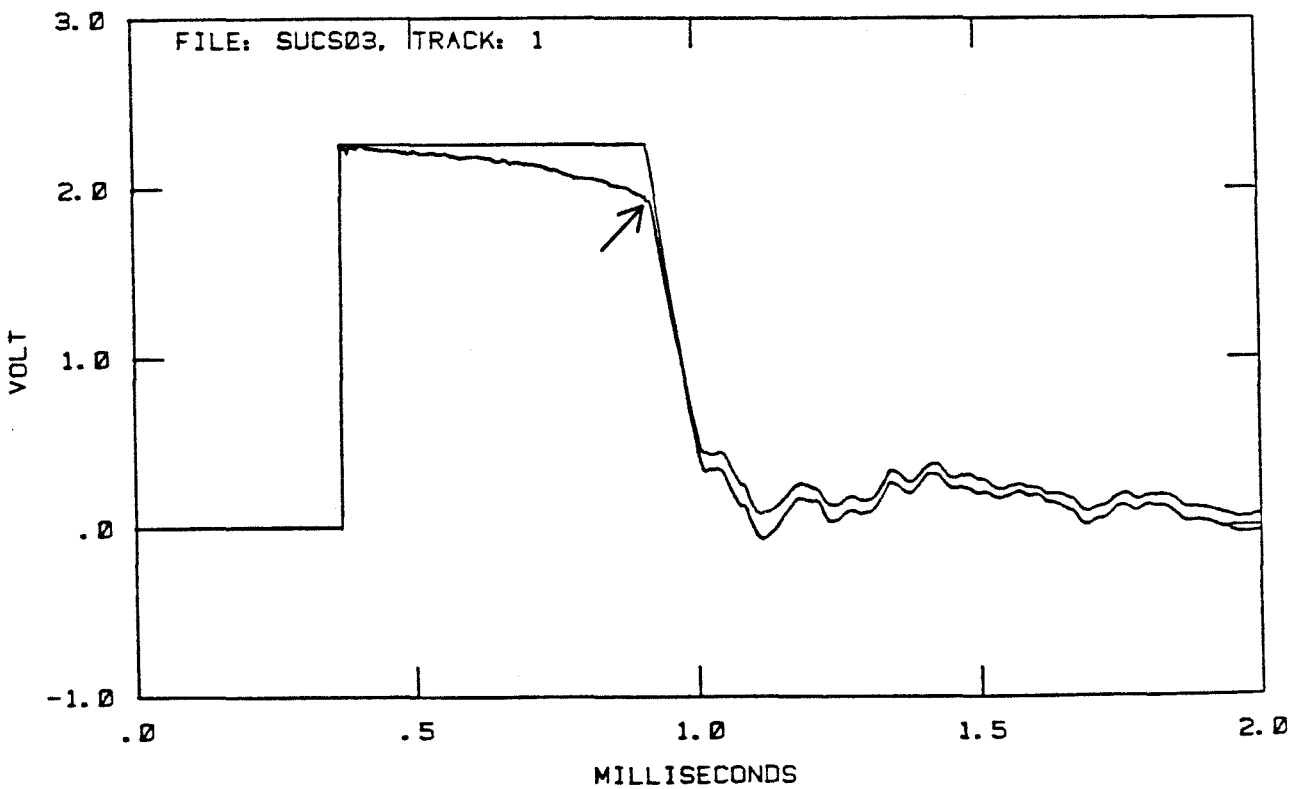

Figure 3.2. Successive shock data for separation times of ∞ and 20 seconds with sensor 7.2 cm from heater.

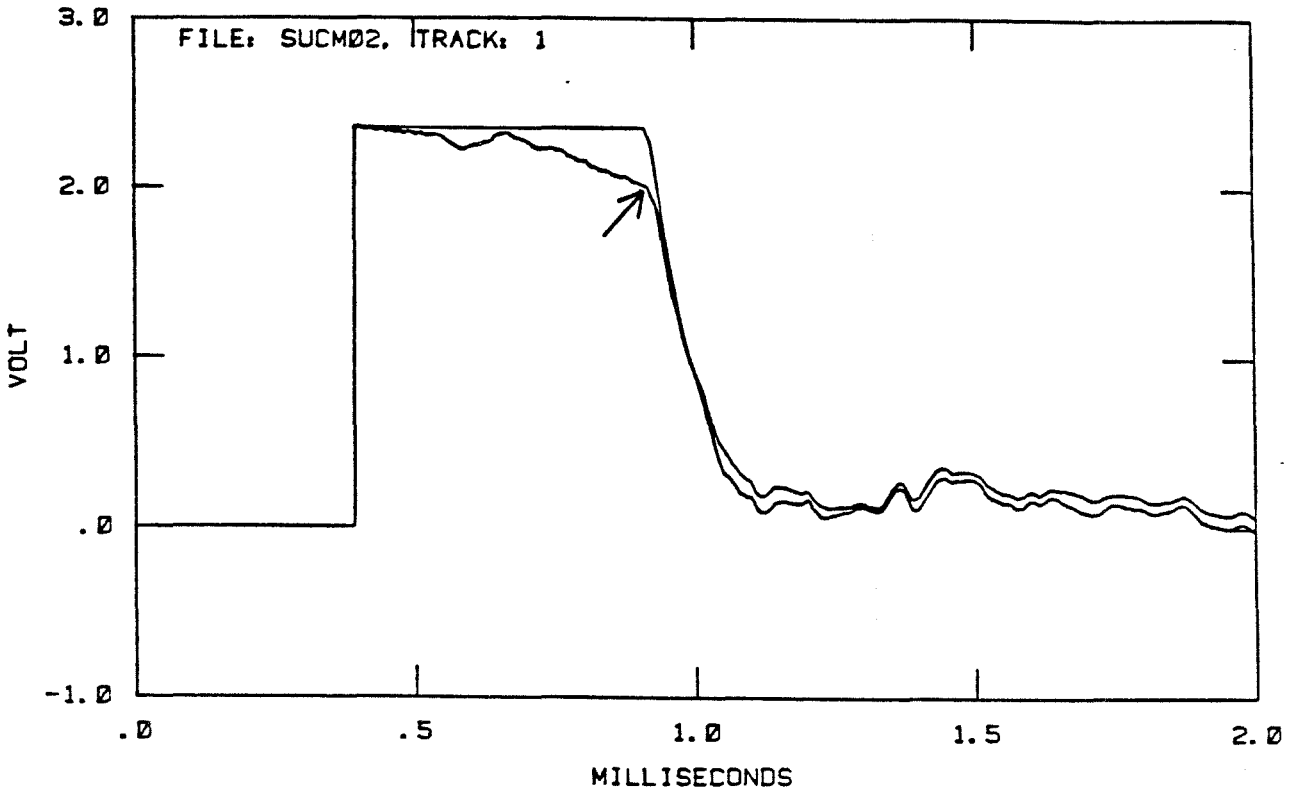

Figure 3.3. Successive shock data for separation times of ∞ and 20 seconds with sensor 9.6 cm from heater.

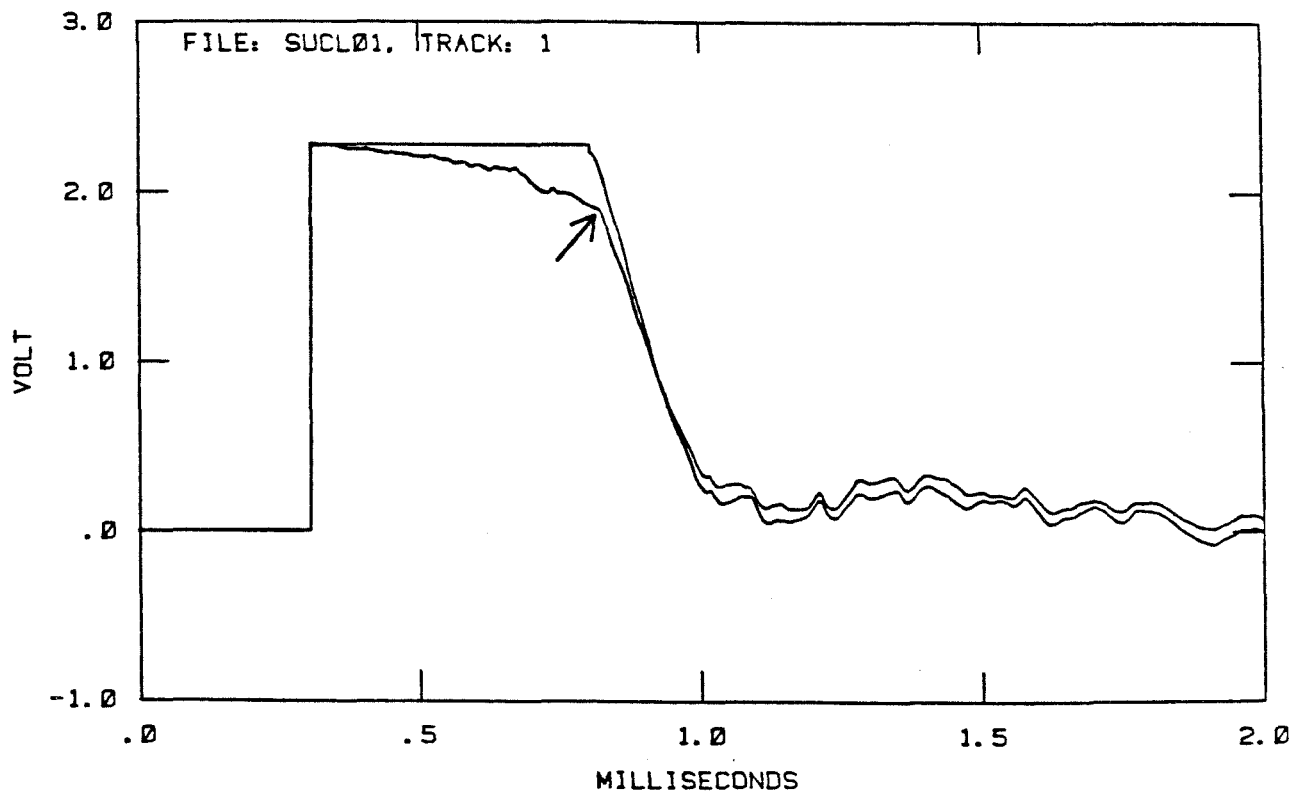

Figure 3.4. Successive shock data for separation times of ∞ and 20 seconds with sensor 14.4 cm from heater.

Chapter 4

ROTATING SHOCK EXPERIMENTS

4.1. Equilibrium of a Rotating Fluid

Before discussing second sound shocks in rotating superfluid helium, it is instructive to review briefly the equilibrium state of a rotating fluid. Consider first a closed arbitrary volume of a nonideal fluid with equation of state

$$e = e(s,\rho) \tag{4.1}$$

where

$$de = Tds + \frac{p}{\rho^2} d\rho. \tag{4.2}$$

Suppose this closed container is rotated at a constant angular velocity $\vec{\Omega}$. Thus, the boundary condition for velocity is

$$\vec{u}\ (boundary) = \vec{\Omega} \times \vec{r}\ (boundary). \tag{4.3}$$

Presumably after a long time all transients have died out, and the fluid has reached its equilibrium state which is described by the Second Law of Thermodynamics.

$$S[e,\rho,\vec{u}] = \int_V \rho s\ dV = \{maximum\}. \tag{4.4}$$

When the problem is posed in this manner, it immediately suggests a calculation of variations approach (Putterman, 1974). Thus, the variation of the entropy integral must vanish.

$$\delta \int_V \rho s \; dV = 0. \tag{4.5}$$

In this problem three integral constraints occur. The final state has a specified mass, angular momentum, and energy.

$$M[e,\rho,\vec{u}] = \int_V \rho dV \tag{4.6}$$

$$E[e,\rho,\vec{u}] = \int_V \rho(e + \frac{1}{2}u^2)dV \tag{4.7}$$

$$\vec{L}[e,\rho,\vec{u}] = \int_V \vec{r} \times \rho\vec{u} \; dV \tag{4.8}$$

One solves this problem with Lagrange multipliers, so the actual problem to solve is

$$\delta \int_V \{\rho s + \Lambda_1\rho + \Lambda_2\rho\,(e+\frac{1}{2}u^2) + \vec{\Lambda}_3 \cdot (\vec{r} \times \rho\vec{u})\}\, dV = 0 \tag{4.9}$$

where

$$\delta e = T\delta s + \frac{p}{\rho^2}\delta\rho \tag{4.10}$$

from equation (4.2) and Λ_1, Λ_2, and $\vec{\Lambda}_3$ are undetermined constants. After carrying out the variations, the following result is obtained.

$$\int_V \left[\left(\frac{\rho}{T} + \Lambda_2 \rho \right) \delta e + (\Lambda_2 \rho \vec{u} + \vec{\Lambda}_3 \times \rho \vec{r}) \cdot \delta \vec{u} \right. \tag{4.11}$$

$$\left. + \left(s + \Lambda_2 \left(e + \frac{1}{2} u^2 \right) - \frac{p}{\rho T} + \Lambda_1 + \vec{\Lambda}_3 \cdot (\vec{r} \times \vec{u}) \right) \delta \rho \right] dV = 0$$

Since δe, $\delta \rho$, and all components of $\delta \vec{u}$ may be varied independently, the expressions multiplying them must be 0.

$$T = -\Lambda_2^{-1} = constant \tag{4.12}$$

$$\vec{u} = \left(-\Lambda_2^{-1} \vec{\Lambda}_3 \right) \times \vec{r} = \vec{\Omega} \times \vec{r} \tag{4.13}$$

$$\mu - \frac{1}{2} u^2 = -\Lambda_2^{-1} \Lambda_1 = constant \tag{4.14}$$

where

$$\mu = e + \frac{p}{\rho} - Ts \tag{4.15}$$

has been used.

So the equilibrium state of a classical rotating fluid has solid body rotation, constant temperature, and constant $\mu - \frac{1}{2} u^2$. This latter equation is more

clearly understood by taking its differential and combining it with the other two equations.

$$\frac{dp}{dr} = \frac{\rho u^2}{r} \tag{4.16}$$

This is just the pressure force balancing the "fictitious" force, and by analogy equation (4.15) is just the chemical potential cancelling the "fictitious" potential so that the total potential is constant.

4.2. Equilibrium of a Rotating Superfluid

To find the equilibrium of a rotating superfluid, the same method as above is employed (Putterman, 1974). The entropy is maximized subject to the integral constraints of mass, energy, and angular momentum. Of course, in this case there are the additional variables $\xi = \frac{\rho_n}{\rho}$ and $\vec{w} = \vec{v}_n - \vec{v}_s$. One point to keep in mind, however, is the irrotationality of the super component, which must be taken into account during the variation. Thus, the variational principle becomes

$$\delta S + \Lambda_1 \delta M + \Lambda_2 \delta E + \vec{\Lambda}_3 \cdot \delta \vec{L} = 0 \tag{4.17}$$

where now

$$E = \int_V \rho \left[e + \frac{1}{2}\xi v_n^2 + \frac{1}{2}(1-\xi)\, v_s^2 \right] dV \tag{4.18}$$

and

$$\vec{L} = \int_V \vec{r} \times \rho \, (\xi \vec{v}_n + (1-\xi) \, \vec{v}_s) dV. \tag{4.19}$$

Varying all quantities independently except $\vec{v}_s$ yields the following relationships.

$$T = -\Lambda_2^{-1} = constant \tag{4.20}$$

$$\vec{v}_n = (-\Lambda_2^{-1} \vec{\Lambda}_3) \times r = \vec{\Omega} \times \vec{r} \tag{4.21}$$

$$\mu + \frac{1}{2} w^2 - \frac{1}{2} v_n^2 = constant \tag{4.22}$$

Note that for $\vec{w} = 0$ these conditions are the same as (4.12-14). Now we assume that the superfluid is irrotational.

$$\nabla \times \vec{v}_s = 0 \tag{4.23}$$

so

$$\vec{v}_s = \nabla \psi \tag{4.24}$$

where ψ is the super component potential. Hence, all three components of $\vec{v}_s$ may not be varied independently.

$$\delta \vec{v}_s = \nabla \, \delta \psi \tag{4.25}$$

Carrying out the ψ variations in equation (4.17) over all $\delta \psi$ such that the boundary terms vanish yields

$$\nabla \cdot (\rho_s \vec{w}) = 0. \tag{4.26}$$

Thus, equations (4.20-23, 26) provide a complete description of the dynamics and thermodynamics of rotating superfluid helium.

It is possible, however, to maintain the irrotationality of the super component in the bulk fluid without requiring the super component to be motionless when rotated. Onsager (1949) and Feynman (1955) suggested that the free energy of the fluid would be reduced by allowing line singularities (potential vortices) to exist in $\vec{v}_s$. A quantum mechanical argument then implies the quantization of the circulation κ. It is assumed that the super component is described by a wave function $\psi_s = \rho_s^{\frac{1}{2}} e^{i\varphi}$. The momentum and vorticity operators in quantum mechanics are given by the following.

$$\tilde{p_s} = -i\hbar\nabla \tag{4.27}$$

$$\tilde{\omega_s} = \nabla \times \tilde{v_s} \tag{4.28}$$

It is assumed that $\tilde{p_s}$ and $\tilde{v_s}$ are related by the mass of the helium atom.

$$\tilde{p_s} = m_4 \tilde{v_s} \tag{4.29}$$

Thus,

$$\tilde{\omega_s} = -\frac{i\hbar}{m_4}\nabla \times \nabla . \tag{4.30}$$

Applying this operation to a nonsingular wavefunction yields 0. Thus, away from

singularities, $\vec{v}_s$ is irrotational and may be expressed as the gradient of a potential. The circulation may be found by integrating $\vec{p}_s$ around a closed loop. If this loop does not pass through a singularity the result is

$$\int_C \vec{p}_s \cdot d\vec{l} = Nh \tag{4.31}$$

where h is Planck's constant and N is an integer. Thus, the circulation around any closed loop C is

$$\kappa = \int_C \vec{v}_s \cdot d\vec{l} = N \frac{h}{m_4} \tag{4.32}$$

Free energy calculations (Feynman, 1955) show that the equilibrium configuration of line vortices in rotating helium has the vortices aligned with the axis of rotation, having an areal density

$$n = \frac{2m_4\Omega}{h} \approx \left(2000 \frac{lines/cm^2}{rad/sec}\right)\Omega \tag{4.33}$$

which mimics solid body rotation. This result breaks down in the vicinity of walls or with small numbers of vortices.

4.3. Motivation and Method of Rotating Experiments

From the successive shock experiments it has been seen that shocks of strength near the breakpoint produce long-lived disturbances in the fluid. The presence of these disturbances enhances decay in a similar shock propagating through fluid containing them. As discussed in the previous chapter, it is thought that such disturbances have vortical character, perhaps being composed primarily of the quantized line and ring vortices mentioned above. Direct

measurement of vorticity in classical fluids is by no means trivial, and in many ways it is even more subtle in superfluid helium. Much more straightforward would be to send a second sound shock wave through a known vorticity field and see how the waveform is modified by the vorticity.

As discussed above, rotation of superfluid helium will send the normal component into solid body rotation, whereas the super component will form quantized line vortices roughly mimicking solid body rotation. For practical experimentation two orientations are convenient. The shock tube may be oriented normal to the axis of rotation so that the line vortices are *perpendicular* to the direction of propagation (but are parallel to the wave front). This case is referred to as the *transverse* orientation (see Fig. 4.1). Another possibility is to have the shock tube aligned with the axis of rotation. In this situation the vortices are *parallel* to the direction of propagation (but are perpendicular to the wavefront). This case is referred to as the *axial* orientation (see Fig. 4.1).

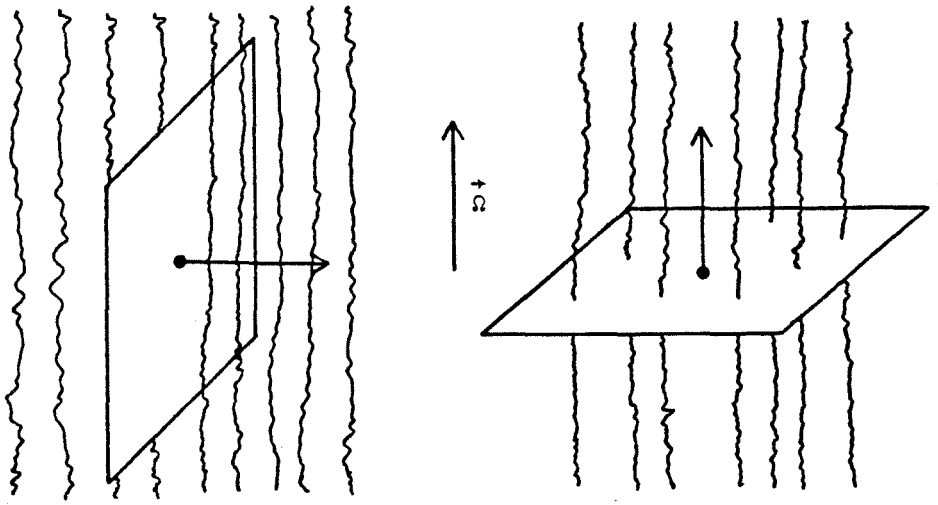

Figure 4.1 Transverse and axial orientations of the rotating shock tube.

A full description of the rotating apparatus is presented in Appendix B.

The experimental procedure is quite similar to that of the successive shock experiments for both the axial and transverse cases. First, the endwall sensor is positioned at a desired location. For the axial case, this is quite easily done *in situ* since the variable length second sound shock tube (Turner, 1979) was used. The transverse case was much more difficult experimentally since the entire shock tube had to be removed from the dewar and fitted with channels of different length for each run (see Appendix C). With the sensor positioned, a shock strength near the break point was selected. Then for various rotation rates shocks of this strength were fired and recorded digitally from the endwall sensor. Practice suggested a waiting time of several minutes between shocks or variations of the rotation rate to avoid hysteresis (recall the successive shock experiments). After all desired data at this station had been taken, the sensor was moved to a new location and the process was repeated.

4.4. Results of the Axial Case

Shown in Figure 4.2 are results of an experiment performed at $T = 1.605\ K$ and $p = s.v.p. = 5.83\ Torr$. In this experiment the sensor was located 2.65 cm from the heater. Note that as the angular velocity is increased, the region of uniform counterflow begins to tilt, indicating that decay has occurred. This decay increases almost linearly with Ω. Furthermore, a warm tail appears behind the shock pulse. As Ω is increased, this tail quickly reaches its asymptotic level. Further increases in Ω do not affect the tail. All of these profiles bear a strong resemblance to profiles of shocks having undergone breakdown. Note particularly the striking similarity to the successive shock experiments, especially the fact that the decay region begins directly at the leading edge of the shocks.

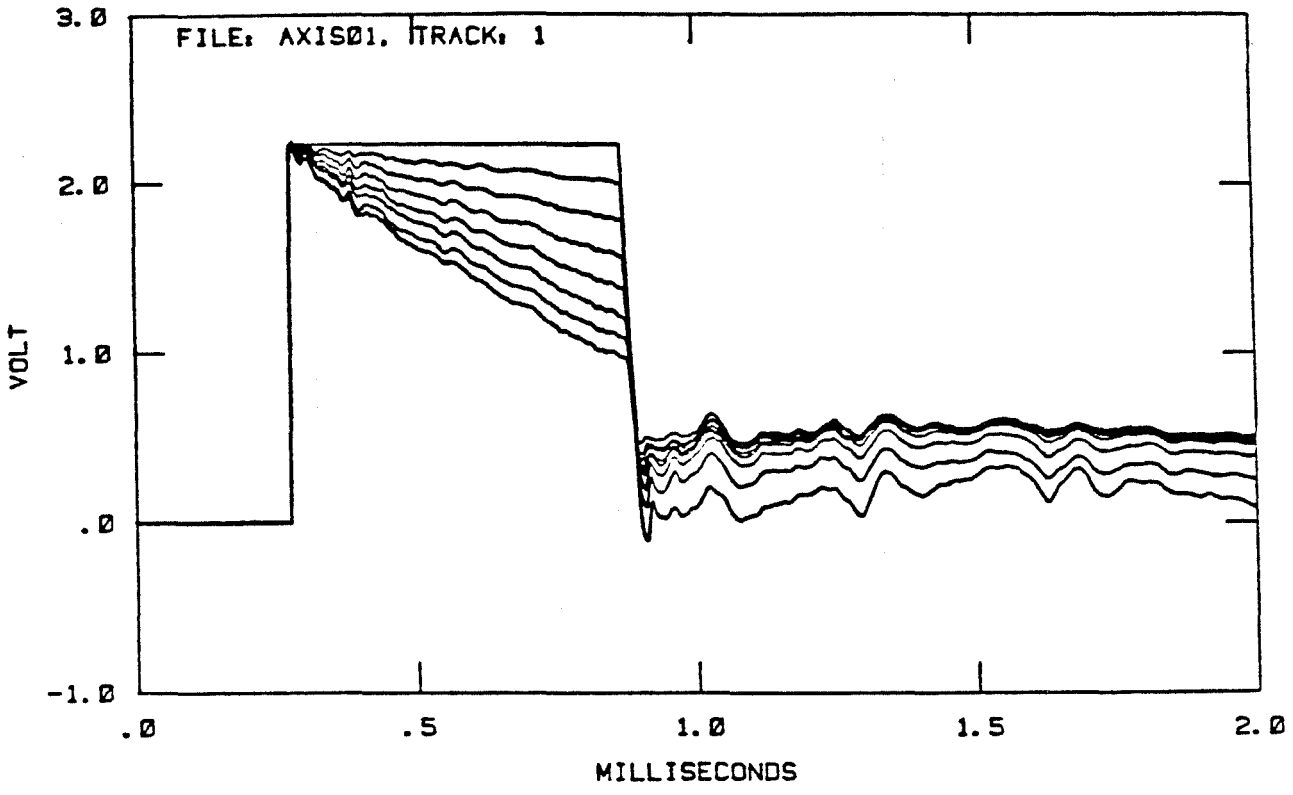

Figure 4.2. Axial shock data for experiment AXIS01. The rotation rate is from 0 °/sec to 420 °/sec in increments of 60 °/sec.

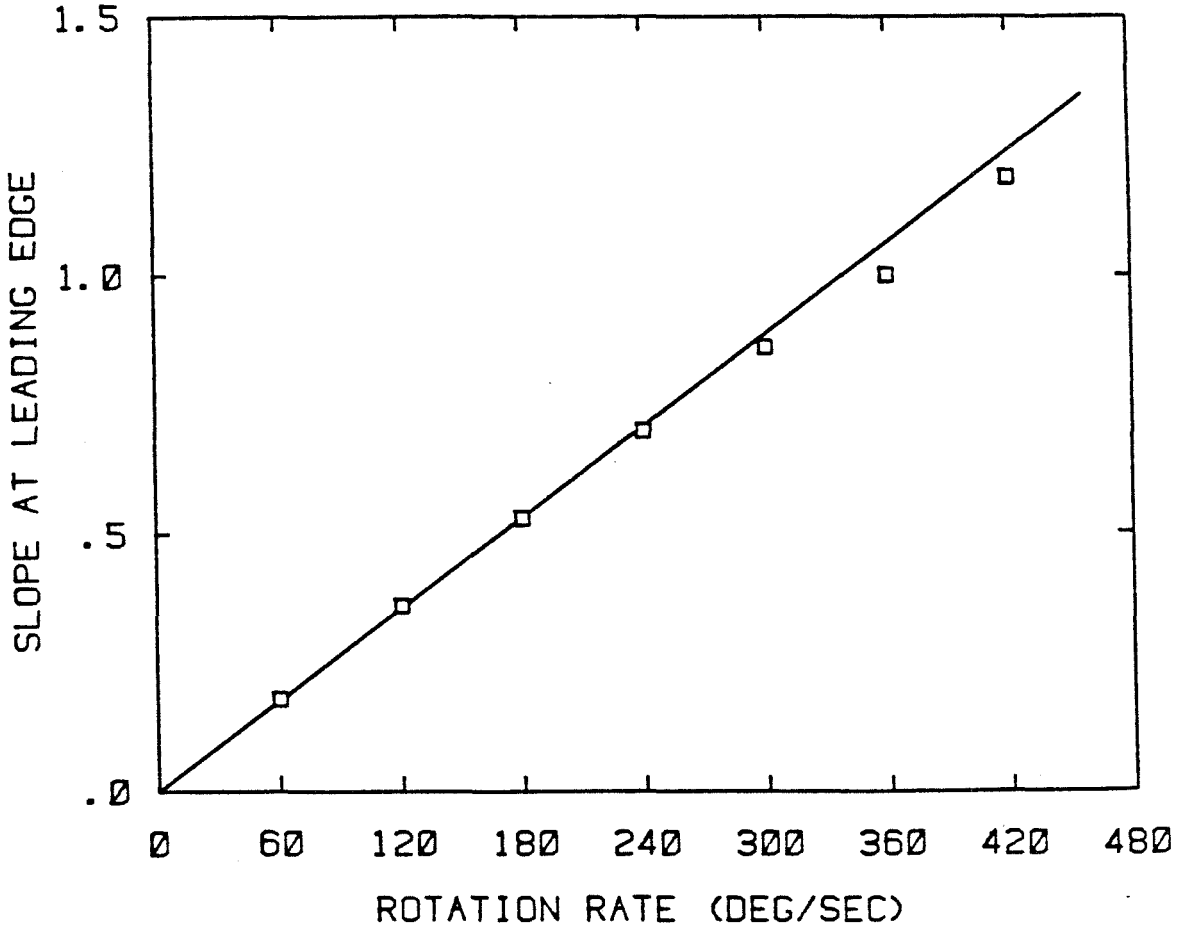

Figure 4.3. Normalized slope vs. rotation rate for experiment AXIS01.

It is of interest to examine the relationship between Ω and the decay. To do this it is useful to characterize the profile modification in terms of the slope at the leading edge. This slope was calculated by fitting a quadratic polynomial through the decayed part of the profile. For experiment AXIS01, the polynomial was fit between 280 μsec and 850 μsec, yielding 1141 points through which to fit the curve. The slope was obtained by evaluating the derivative at the leading edge and normalizing this by the height. This normalized slope is plotted in Figure 4.3.

Even if the slope decay were proportional to Ω, one would not expect to observe this directly. The reason for this is that the profile propagates nonlinearly — slopes flatten or steepen because the characteristic velocity is a function of amplitude. In the case above, the slopes will be flattened by the nonlinear wave propagation and thus should not be quite proportional to Ω. The effect will be more pronounced as the slope becomes steeper. Thus, for large values of Ω, the measured slope should begin to undershoot the value predicted by a linear proportionality. Moreover, at the shock front the characteristics are propagating into the shock, so the shock undergoes triangular wave decay. Nevertheless, for small Ω the slope decay is linear in Ω.

As discussed above, it is of interest to know whether the profile decays as the shock pulse propagates. Experiments as discussed above were run at three sensor locations: 2.65 cm, 5.81 cm, and 10.52 cm. In all three cases the wave strength was kept constant. Shown in Figure 4.4-6 are results for a rotation rate of 60 °/sec. The nonrotating case is shown for reference. That the pulses undergo decay while propagating is easily seen. The clearest manifestation is the decrease in amplitude at the corner point (the point at which the expansion and the "uniform" regions are coincident). Again to quantify this result, it is useful to calculate the slope at the leading edge. Define the decay parameter Λ

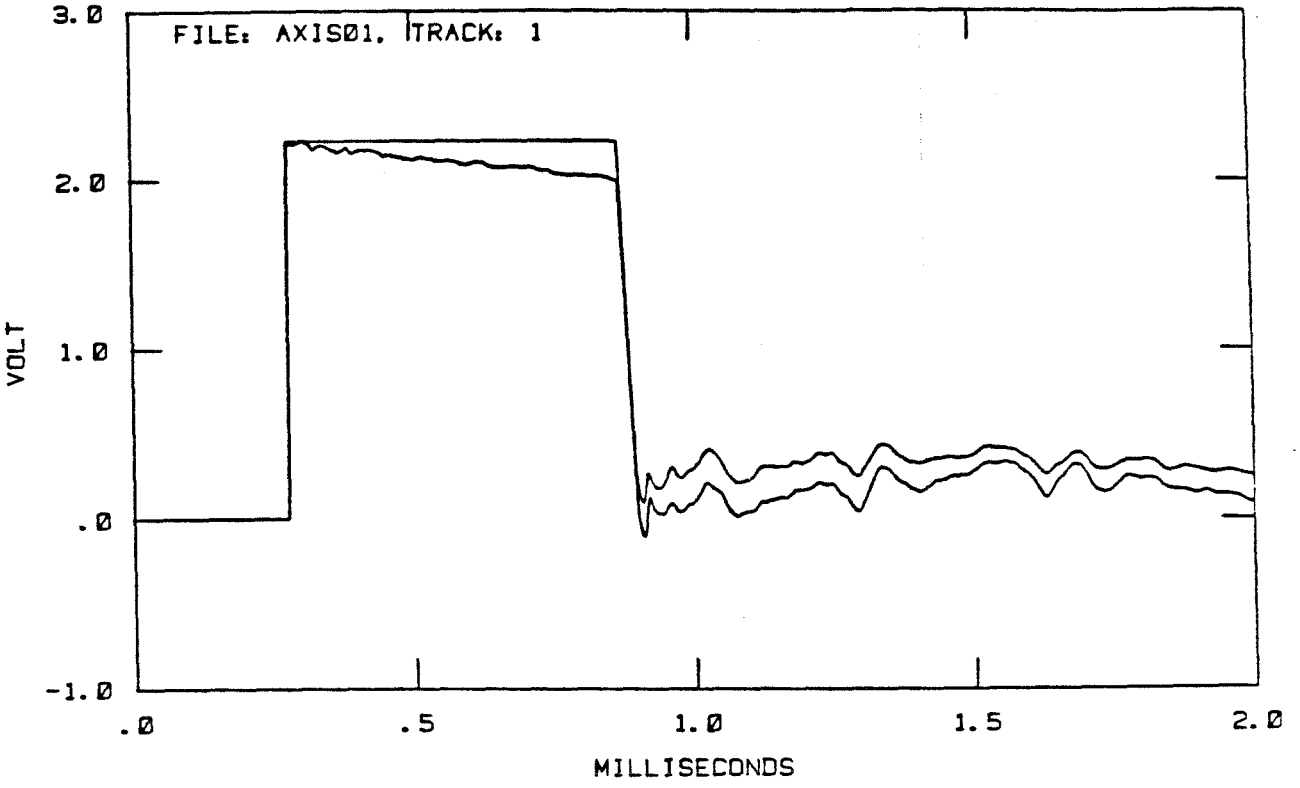

Figure 4.4. Axial shocks with 0 °/sec and 60 °/sec located 2.65 cm from heater.

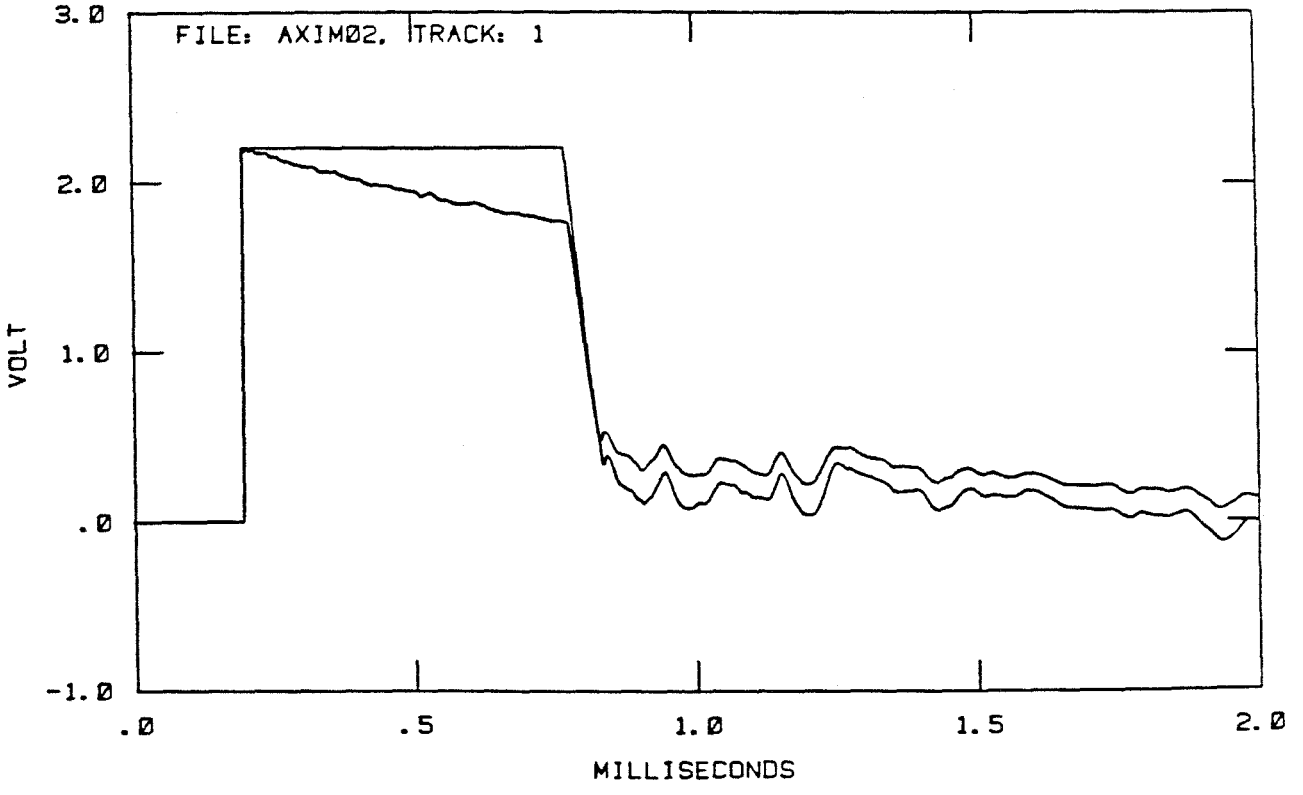

Figure 4.5. Axial shocks with 0 °/sec and 60 °/sec located 5.81 cm from heater.

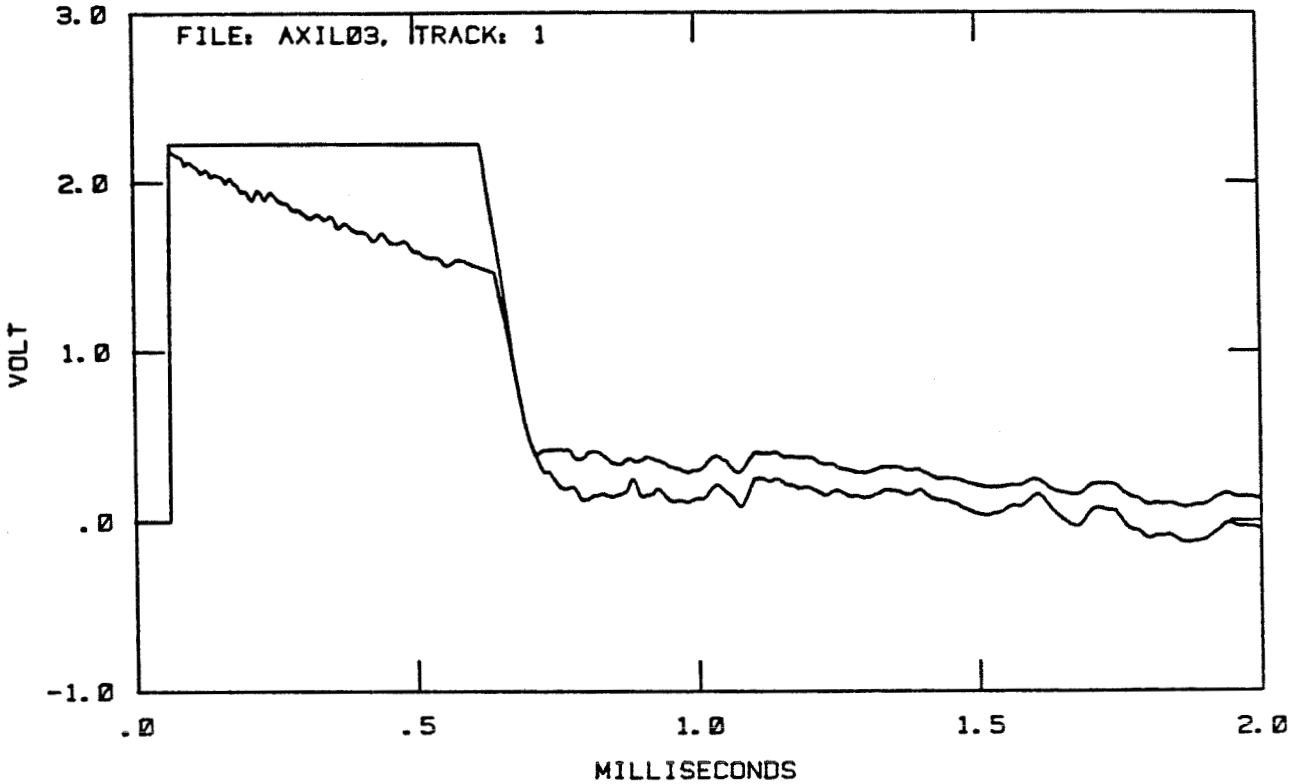

Figure 4.6. Axial shocks with 0 °/sec and 60 °/sec located 10.52 cm from heater.

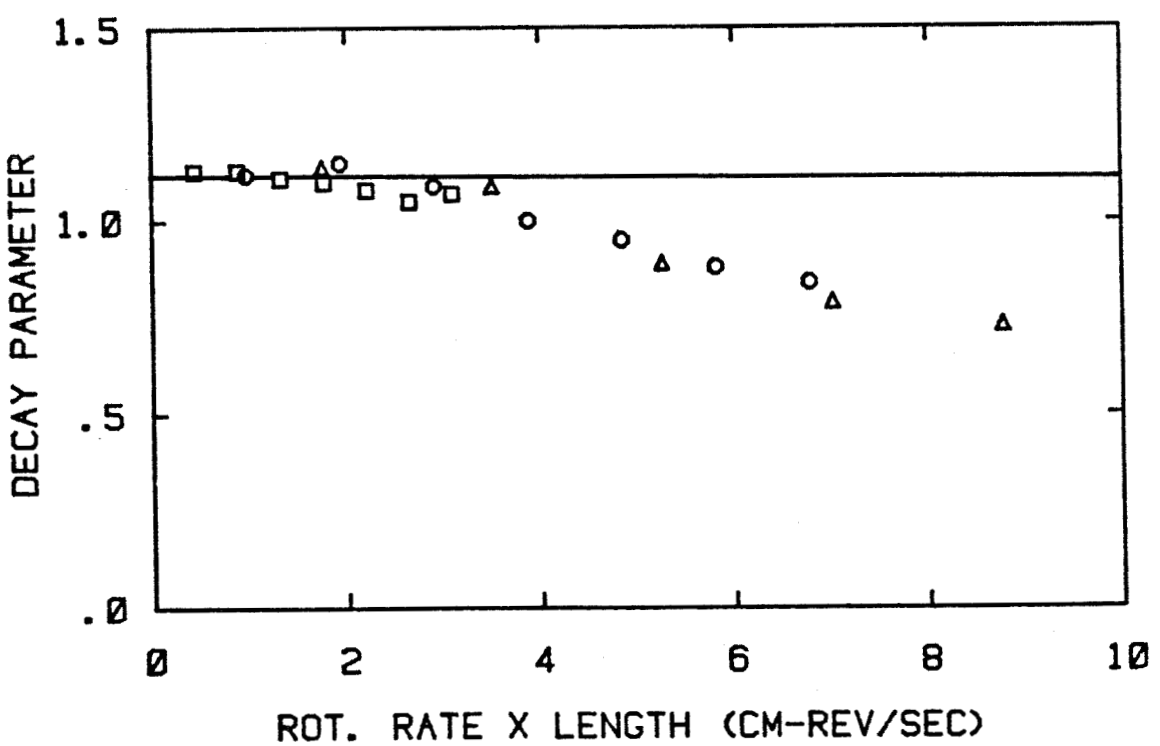

Figure 4.7. Decay parameter for AXI experiments. □'s are at 2.65 cm, ○'s are at 5.81 cm, and △'s are at 10.52 cm. Decay parameter is in units of $(1.8 \cdot 10^5/\pi)$ cm^{-1}.

to be

$$\Lambda = \frac{S}{\Omega L} \tag{4.34}$$

where S is the slope in $msec^{-1}$, Ω the rotation rate in °/sec, and L is the length in cm. Figure 4.7 is a plot of Λ for a variety of different lengths and rotation rates. In all cases, however, the shock strength is held constant. It is quite clear from Figure 4.7 that the slope decay is proportional both to the rotation rate and to the distance traveled by the shock front. Deviations from this are in the direction predicted by the nonlinear wave speed.

Figures 4.8-10 show results for Ω = 300 °/sec, which correspond to points in the right half of Figure 4.7. That the nonlinear wave speed and triangular wave decay are having an effect is seen in that the shock itself is being weakened by these effects. It is to be emphasized that these profiles are qualitative similar to pulses in which breakdown is occurring.

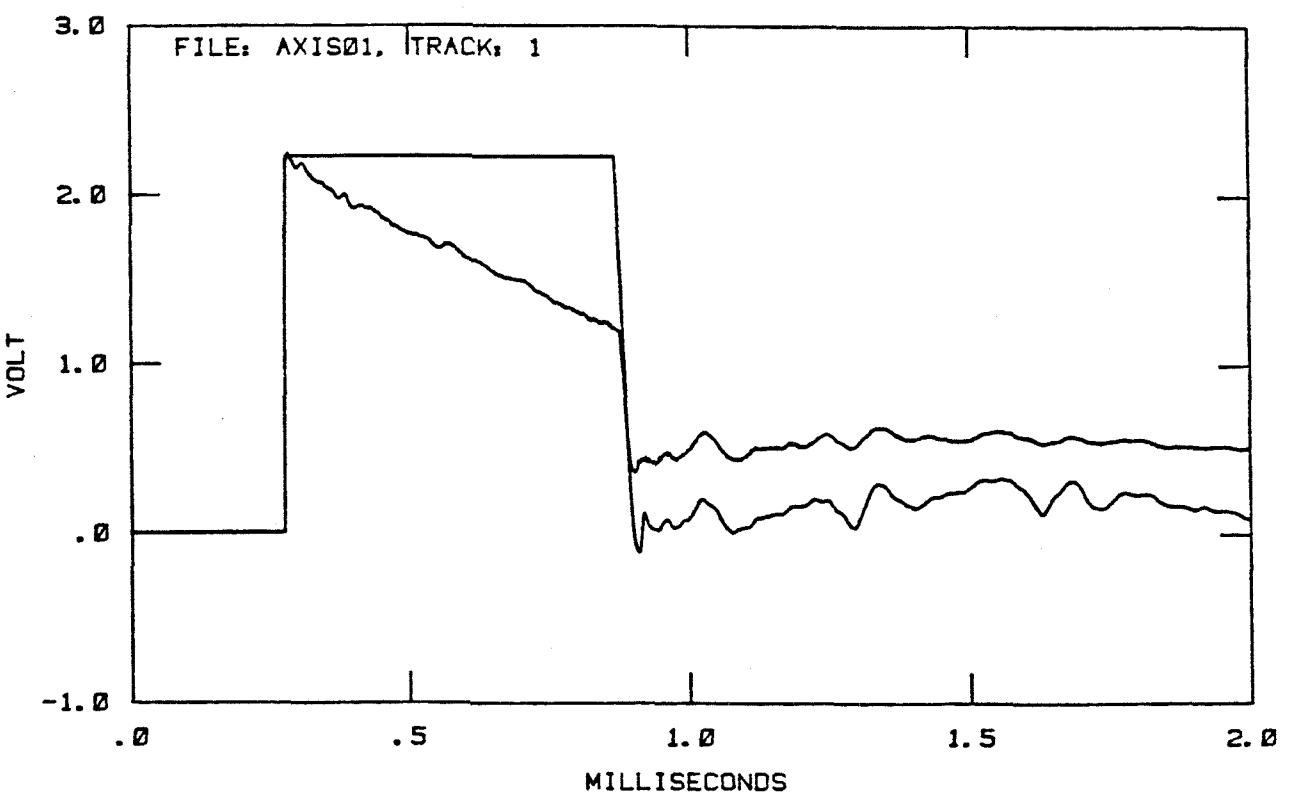

Figure 4.8. Axial shocks with 0 and 300 °/sec located 2.65 cm from heater.

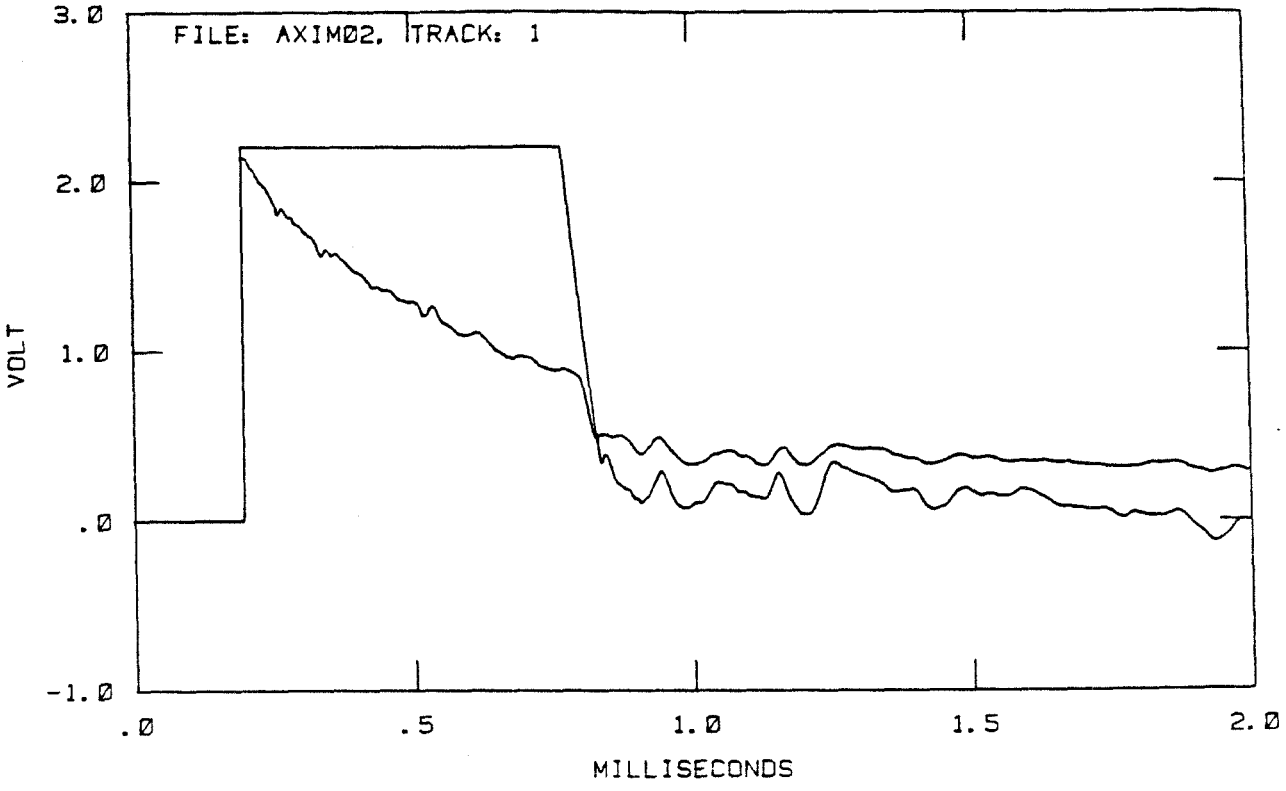

Figure 4.9. Axial shocks with 0 and 300 °/sec located 5.81 cm from heater.

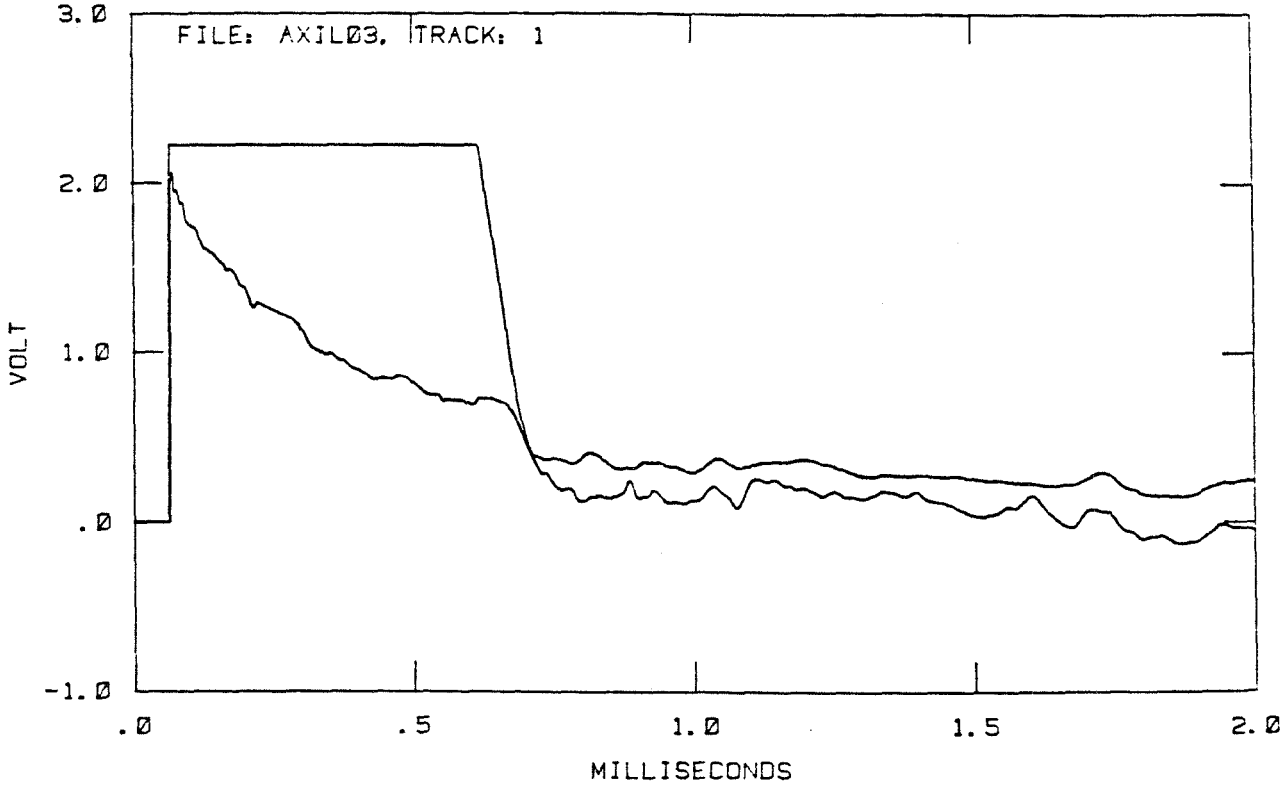

Figure 4.10. Axial shocks with 0 and 300 °/sec located 10.52 cm from heater.

4.5. Results of the Transverse Case

Shown in Figure 4.11 are results of an experiment with the shocks propagating normal to the rotation axis. This experiment was done at the same thermodynamic conditions as the experiments in the axial case although here the shock strength was slightly greater. The rotation rate was again varied from 0°/sec to 420°/sec in increments of 60°/sec. The results are qualitatively similar to those in the axial case with one important difference. The onset of decay is delayed by about 100 μsec rather than occurring immediately behind the shock. The significance of this point will be discussed in a later section.

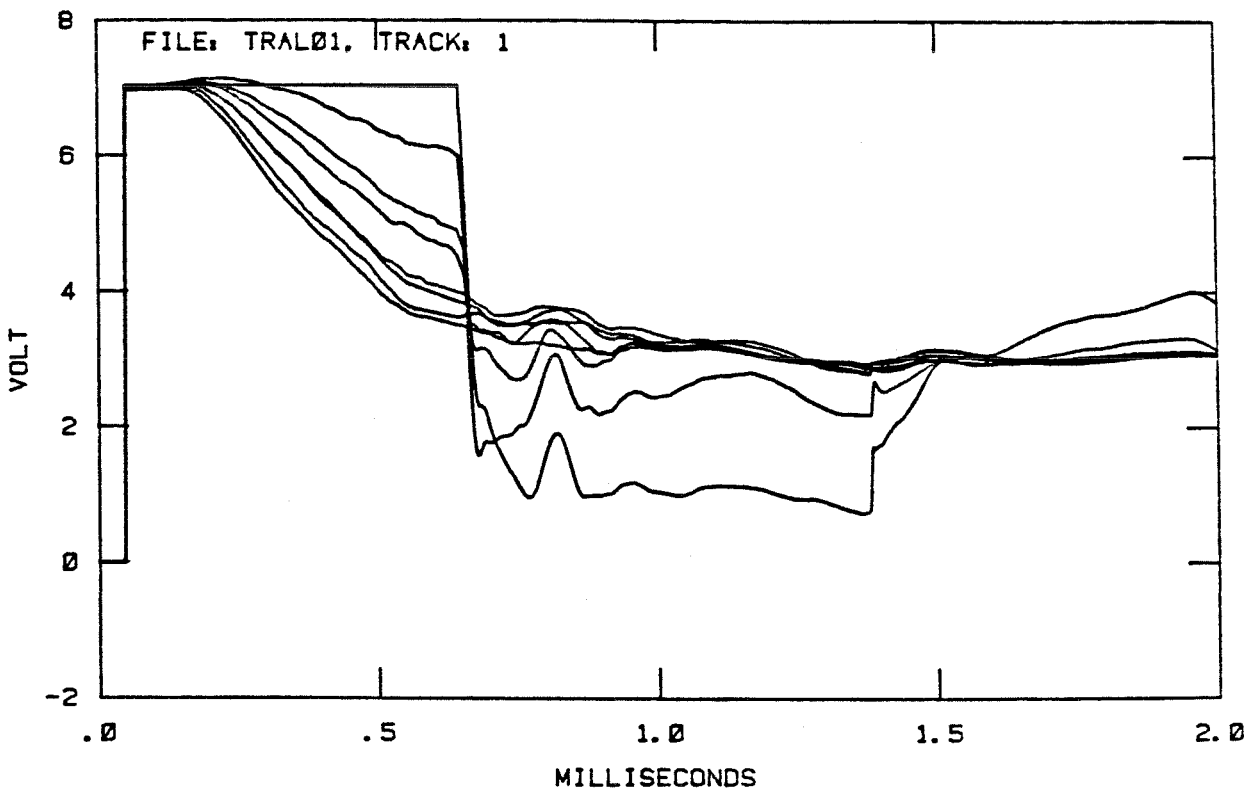

Figure 4.11. Transverse shock data for experiment TRAL01. The rotation rate is from 0 °/sec to 420 °/sec in increments of 60 °/sec. The discontinuity around 1.4 msec is the shock after reflecting from both endwalls (3 transits of the shock tube length).

As in the axial case the question arises as to whether the decay is ongoing while the shock propagates (as it is for the axial experiments) or whether it occurs only in a small region near the heater (as it does for the successive shock experiments). The initial guess would be that since the vortices are uniformly distributed in the shock tube, the pulse would decay while propagating. Although the results are neither as visually striking nor as easily quantified, measurements of the corner point height show unambiguously that the pulses have decayed while propagating. Figures 4.12-13 show some results performed in shock tubes of length 0.99 cm and 1.34 cm. All four shocks are of the same strength, and two rotation rates (180°/sec and 420°/sec) are shown for comparison. The corner heights, normalized by the height of the leading edge, are shown in Table 4.1.

Table 4.1. Decay of Transverse Shocks

Position (cm)	Ω (°/sec)	Normalized Corner Height
0.99	180	0.87
1.34	180	0.80
0.99	420	0.71
1.34	420	0.63

4.6. Local and Global Quantities

Before a discussion of the results, it is worth mentioning that certain features of the shock pulses are local while other features are global. By this it is meant that certain features are found to depend only upon their distance behind the shock front while certain other features depend on the length and height of the pulse. The profile of the shock and the decay region are quite invariant with respect to the length of the pulse. Figure 4.14 shows three pulses

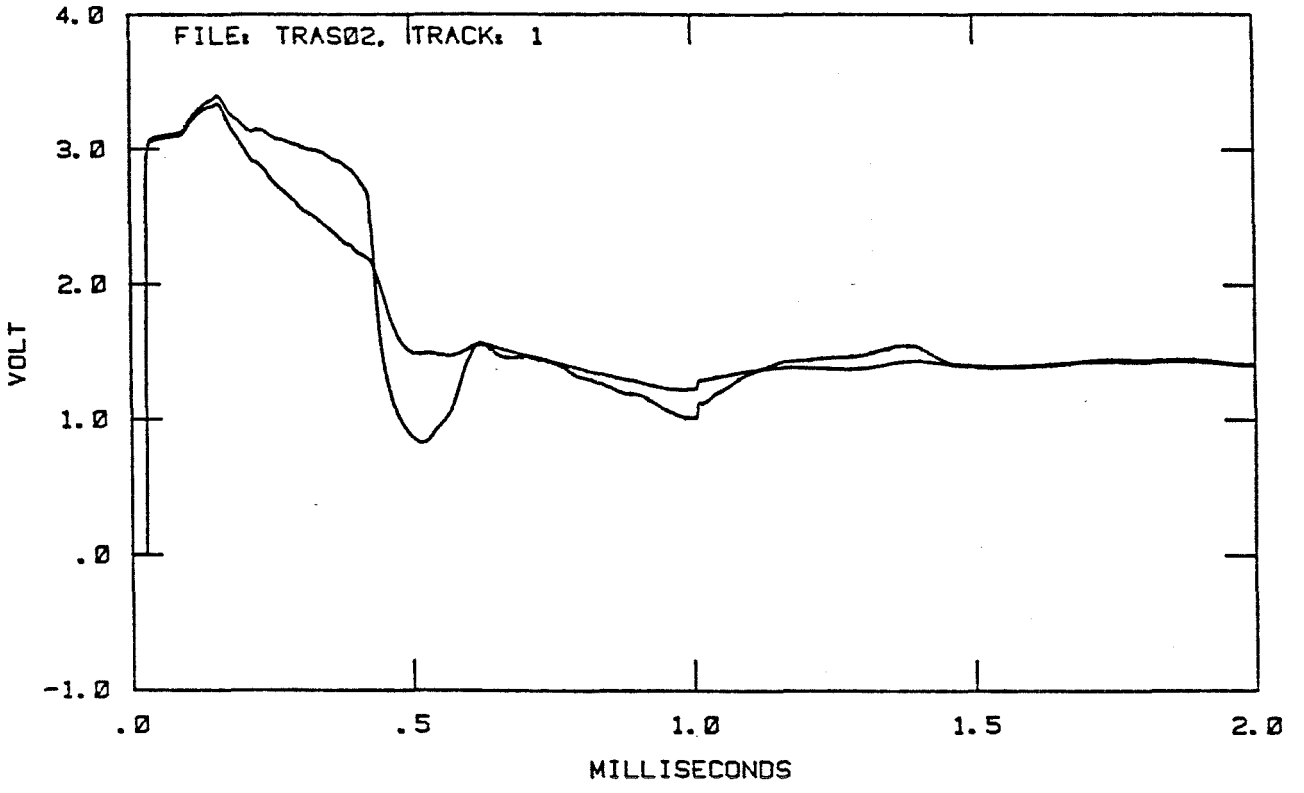

Figure 4.12. Transverse shocks with 180 °/sec and 420 °/sec 0.99 cm from heater.

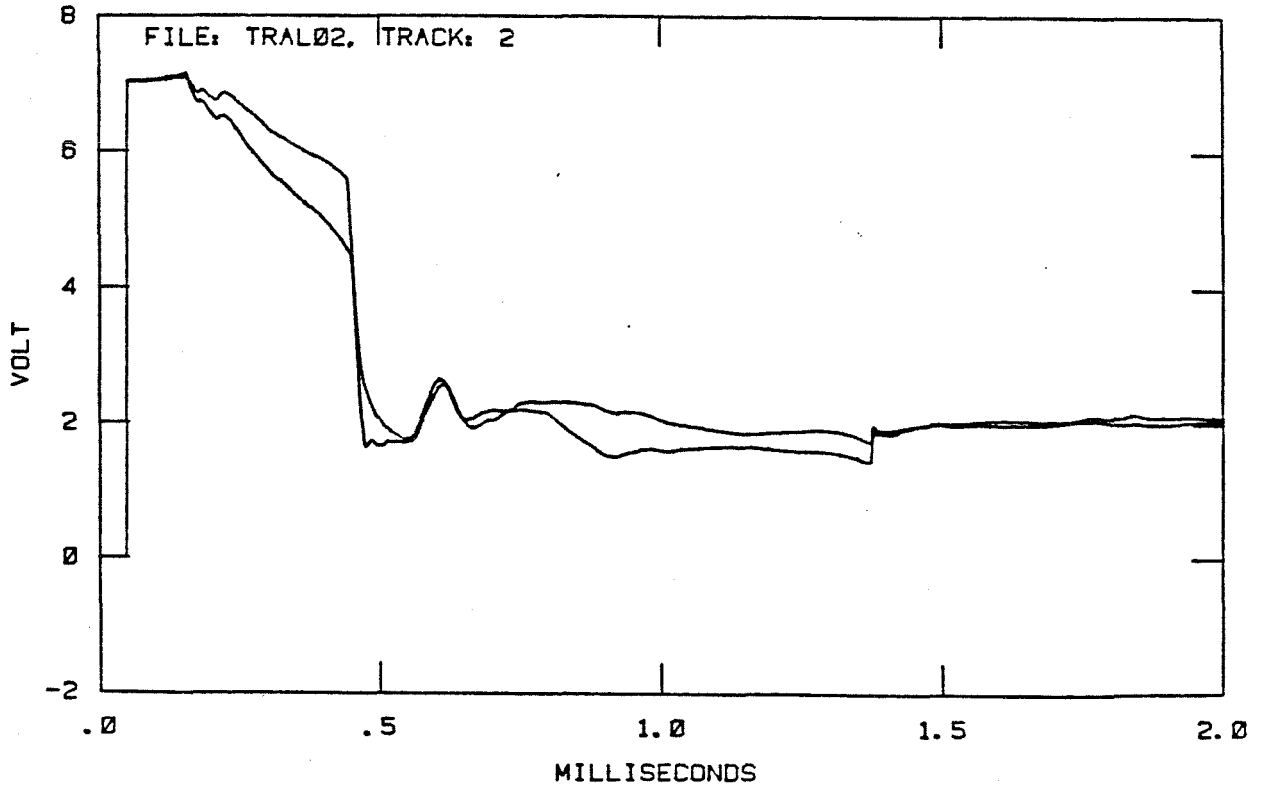

Figure 4.13. Transverse shocks with 180 °/sec and 420 °/sec 1.34 cm from heater.

of lengths 200 μ sec, 300 μ sec, and 400 μsec. In all cases the profiles lie atop one another until the expansion fans, which parallel each other very closely.

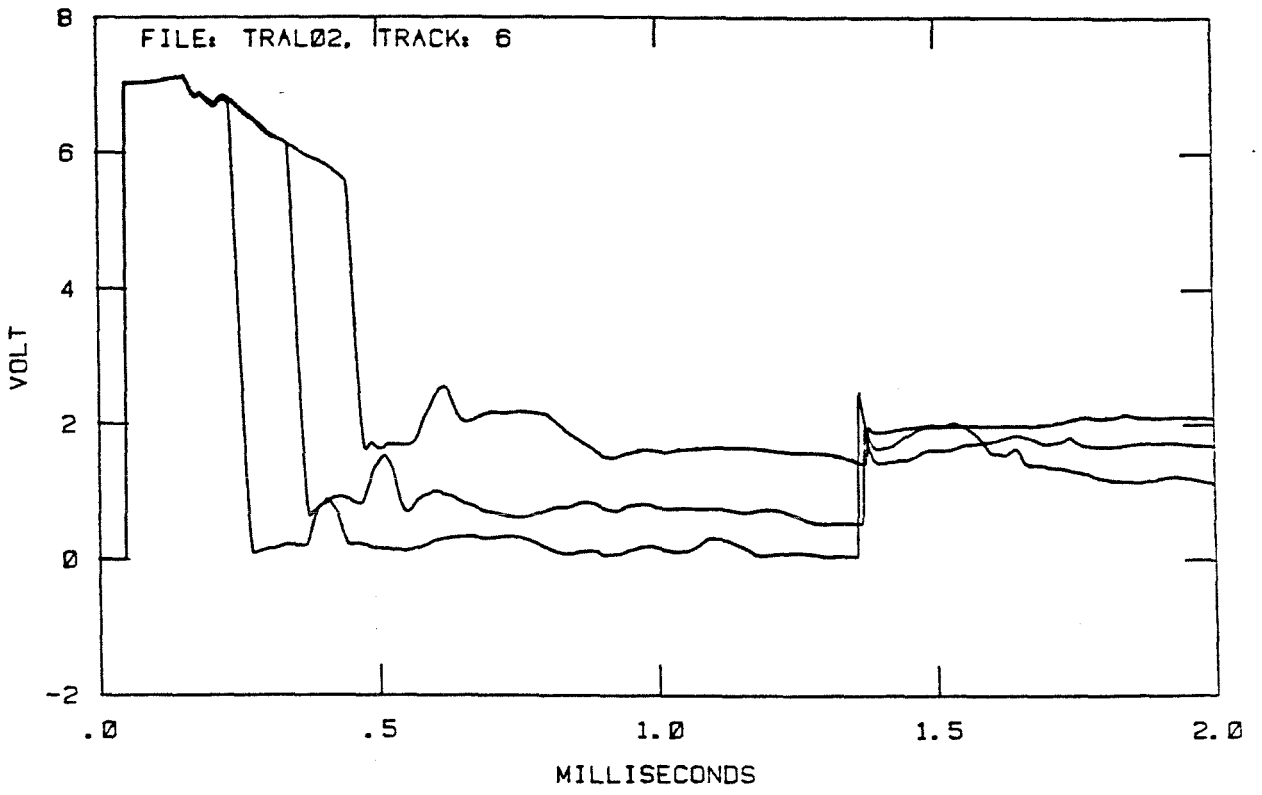

Figure 4.14. Decay does not depend on pulselength.

By contrast, the warm tails following these shocks are quite different. These traces show a feature typical of such experiments. As the pulse length is increased, the tail height rises. Conversely, it is possible to produce strong shocks (undergoing strong breakdown) with virtually no tail simply by reducing the pulse length. Recall from previous discussions that the tail height rapidly reached an asymptotic level when the rotation rate was increased. Further increases of rotation rate left this "mature" tail unaffected (see Fig. 4.11 as another example). The height of this mature tail may be varied in two ways.

One is to increase the pulse length since the height of the mature tail is found to be proportional to the pulse length. Moreover, increasing the voltage V across the heater produces a mature tail of height proportional to V^2. Thus, the mature tail height is proportional to the energy put into the pulse. Define the amplitude ratio to be

$$R = \frac{A}{V^2 T} \tag{4.35}$$

where A is the amplitude of the mature tail in volts, V is the heater voltage in volts, and T is the pulse length in seconds. Thus, R should remain approximately constant. Shown in Table 4.2 are values of R for several different shocks. The transverse rotating shock tube was used (length 1.34 cm) and the rotation rate was 420°/sec to ensure a mature tail in all cases. It is seen that R is indeed constant, showing that the tail amplitude is proportional to the amount of energy originally in the shock pulse.

Table 4.2. Amplitude Ratio of mature tails

Pulse Height (A)	Heater Voltage (V)	Pulse Length (T)	R
2.57	34.5	500μsec	4.33
2.03	34.5	400μsec	4.27
1.57	34.5	300μsec	4.39
1.05	34.5	200μsec	4.40
3.18	3.50	600μsec	4.32
2.68	32.5	600μsec	4.23
2.36	30.0	600μsec	4.37
3.70	37.5	600μsec	4.38
4.18	40.0	600μsec	4.36

4.7. An Explanation of the Rotating Results

To explain the results of the rotating experiments, the following facts should be kept in mind. First, recall that if quantized vortices, particularly rings, are present in the fluid, counterflow may decay by the mechanism proposed by Turner (discussed in Chapter 2). In fact, the maximum counterflow velocity has the thermodynamic dependence predicted by this theory. Second, in the axial case the decay was proportional to the rotation rate and to the distance that the shock traveled. Third, the axial and the successive shock experiments were similar in that the decay began sharply at the leading edge, whereas in the transverse case the onset of decay was delayed significantly.

Consider for a moment a weak shock wave in an ordinary fluid traveling along a heated wall (Thompson, 1972). For an inviscid, incompressible fluid the Crocco-Vazsonyi theorem becomes

$$\frac{D\vec{\omega}}{Dt} = (\vec{\omega} \cdot \nabla)\,\vec{u} + \nabla T \times \nabla s \tag{4.36}$$

where $\vec{\omega} = \nabla \times \vec{u}$ is the vorticity. In the above two-dimensional case, $(\vec{\omega} \cdot \nabla)\,\vec{u} = 0$, so equation (4.36) reduces to

$$\frac{D\vec{\omega}}{Dt} = \nabla T \times \nabla s\,. \tag{4.37}$$

Thus, the vorticity produced in the fluid behind the shock is found by integrating this equation in time for each fluid element as the shock passes over it.

$$[\omega] \sim c^{-1}[T]_{shock}\,|\nabla s_{wall}| \tag{4.38}$$

Here c is the wave speed. Another way of looking at this example is that due to

the entropy gradient near the wall, the wave speed c is modified. Because of this, the shock strength varies along the front. Thus, the shock front becomes slightly curved, and vorticity is produced (see Fig. 4.15). It should be said, however, that a curved wavefront will not produce vorticity if the shock strength is constant along the front. The best examples of this are cylindrically and spherically converging waves. Nevertheless, wavefronts that are curved because of nonuniform shock strength *always* imply the creation of vorticity.

Consider the case of a second sound shock propagating axially along a quantized vortex line. In the vicinity of the line, the thermodynamic state is slightly different than it is at ∞. Although the temperature remains constant, the pressure falls near the line according to the relation

$$\nabla p = -\frac{1}{2}\rho_s \nabla v_s^2 \tag{4.39}$$

which may be integrated if ρ_s does not vary much to yield

$$p + \frac{1}{2}\rho_s v_s^2 = p_\infty, \tag{4.40}$$

which is a Bernoulli theorem. Thus, near any vortex line there are radial gradients in the thermodynamic variables. These gradients cannot be determined explicitly since the canonical equation of state $\mu = \mu(p, T, w^2)$ is not known. Moreover, near the core, there must be strong radial gradients because $\rho_s \to 0$ over a few angstroms.

It is plausible that these radial gradients allow the production of azimuthal vorticity (vortex rings) around the vortex line (see Fig. 4.16). All of the gradients produced by the shock are parallel to the vortex line, so taking the cross

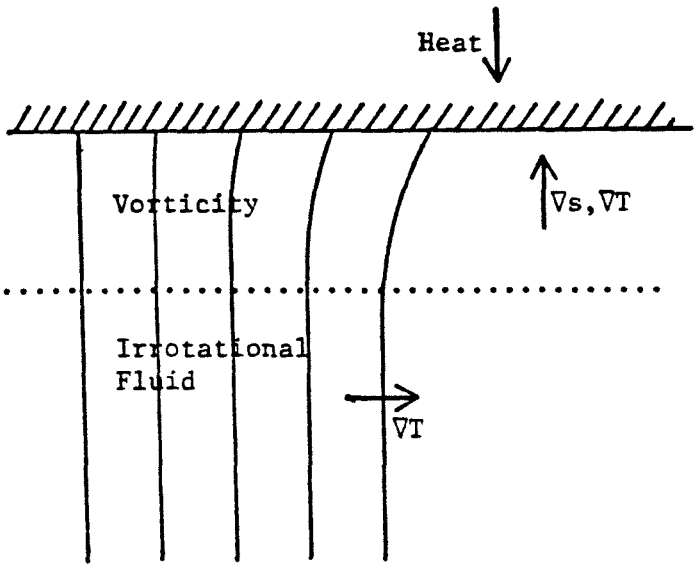

Figure 4.15. A weak shock wave propagating along a heated wall. Vorticity is produced near the wall.

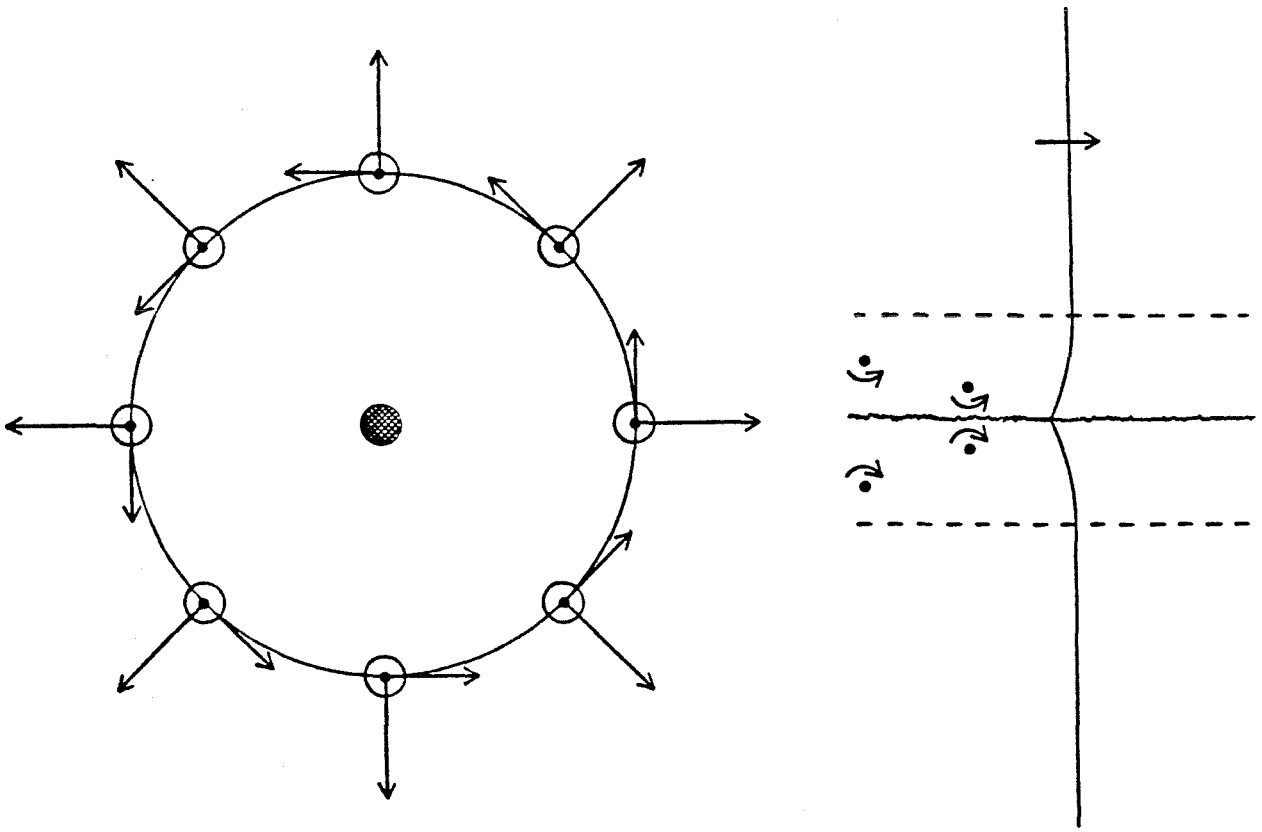

Front View (enlarged) Side View

Figure 4.16. A second sound shock creates azimuthal vorticity while propagating along a quantized vortex. In the front view, the vortex gradients are radial, the shock gradients are out of the paper, and the cross products are azimuthal.

product of shock gradients ($\hat{e}_z$) and vortex gradients ($\hat{e}_r$) yields azimuthal vorticity production ($\hat{e}_\theta$). Needless to say, this description cannot be completely correct — circulation in the super component is quantized. However, one can imagine some nonsteady process periodically producing vortex rings as the shock propagates along the vortex line. In this view the vortices are important in that they provide nucleation sites for rings rather than being tangled, stretched, or torn. These vortex rings then expand against the flow as discussed in Chapter 2.

The transverse case presents a rather different picture than the axial case. Although the gradient cross product is not zero everywhere, the effect is lessened since the gradients are no longer perpendicular. Moreover, the shock encounters each vortex line only briefly rather than *continuously* as in the axial case, and the ring-producing symmetry of the axial case is lacking during these encounters. In any case, it seems that the effect should be reduced in the transverse case.

Yet this is not exactly what happens. The decay is delayed in the transverse case, appearing quite dramatically around 100 μsec or so behind the shock front. This fact, however, actually lends support to the above ideas when it is realized that the onset of decay is coincident with the arrival of secondary wavelets (see Fig. 4.17). Secondary wavelets are produced at the heater seal: gaps or irregularities in the seal produce perturbations in the flow (see Fig. 4.18). These wavelets propagate radially outward from the corners and arrive slightly later than the main pulse since their path length is longer. More important, however, is the fact that they introduce a mean component of the thermodynamic gradients along the vortex lines, as is the situation in the axial case. The decay may then proceed as above.

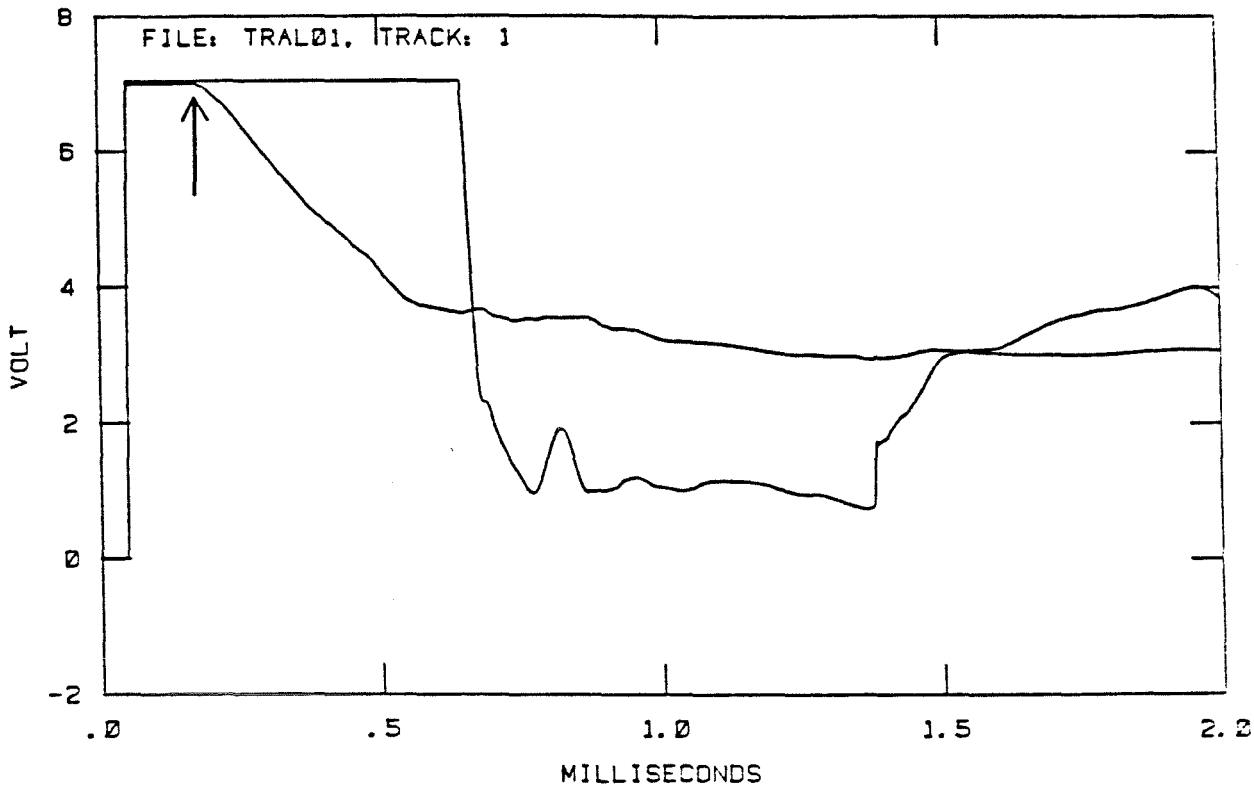

Figure 4.17. Decay in transverse shocks begins with arrival of secondary wavelets (at arrow). Rotation rates are 0 °/sec and 360 °/sec.

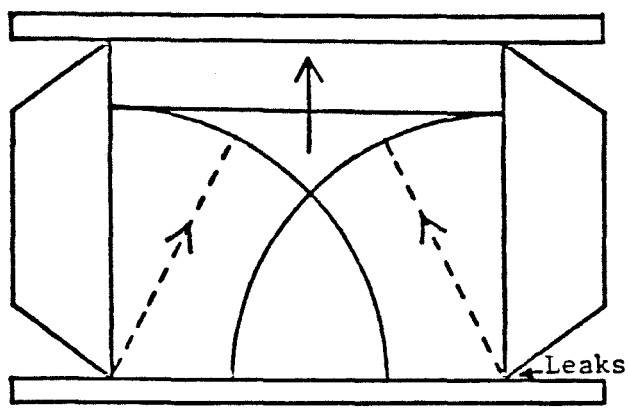

Figure 4.18. Secondary wavelets are produced at the heater seal when a second sound shock is fired.

These results lend an interesting interpretation to the successive shock experiments. Recall that as the separation time was reduced, the successive shock exhibited decay *beginning directly at the leading edge* (see Figs. 3.1-4). Comparison with the axial experiments suggests that any vorticity remaining in the fluid has a significant mean square component perpendicular to the heater. Although this sounds unusual, it is really not so since walls tend to attract and absorb vortices parallel to them (see Fig. 2.7). However, the remaining vorticity is not all axial; rather, the convexity of the successive shocks suggests a distribution (tangle) of vorticity (compare the successive and transverse shocks).

Chapter 5

CONVERGING SHOCK EXPERIMENTS

5.1. Motivation

It has been shown that the presence of vorticity enhances the breakdown phenomena. Specifically, ongoing decay is observed when vorticity is present in the bulk fluid. However, no progress has been made toward observing spontaneous breakdown out in the bulk fluid. It was mentioned above that the primary difficulty in making strong second sound shocks lay in getting the heat into the liquid, not in transporting it by counterflow. In order to observe breakdown in the bulk, it is therefore necessary to introduce a strong heat flux away from boundaries (say, with a laser sheet) or to strengthen a weaker second sound shock.

The latter method was found to be amenable to investigation with equipment on hand and proven techniques, so it was pursued. There are several ways to strengthen a wave. Two waves may merge to form one stronger wave as shown in Figure 5.1. This merging could be accomplished in space rather than time (see Fig. 5.2). A mach stem could be produced by having a planar shock incident on a wedge (see Fig. 5.3).

Perhaps the simplest way to produce a larger relative velocity is to use a converging channel to strengthen a shock. It is a well known result of acoustics that a weak wave in a channel will have a strength $s(x)$ given by

$$\frac{s(x)}{s(x_o)} = \left[\frac{A(x_o)}{A(x)}\right]^{\frac{1}{2}} \tag{5.1}$$

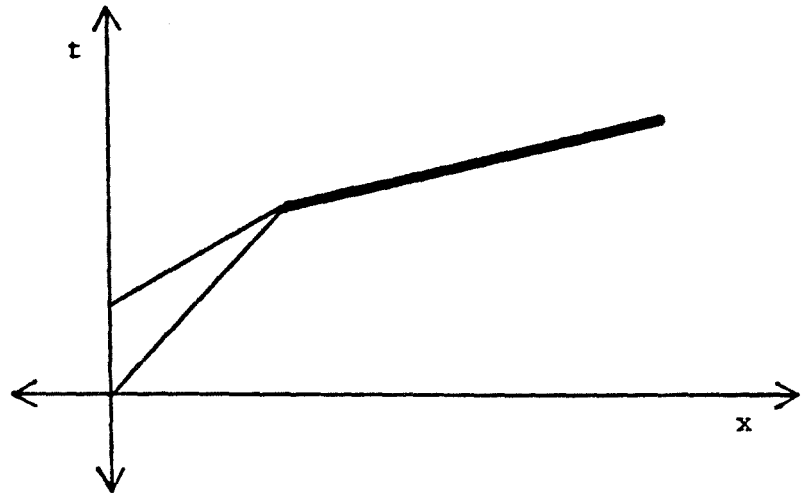

Figure 5.1. Two shocks coincide in time to form a stronger shock.

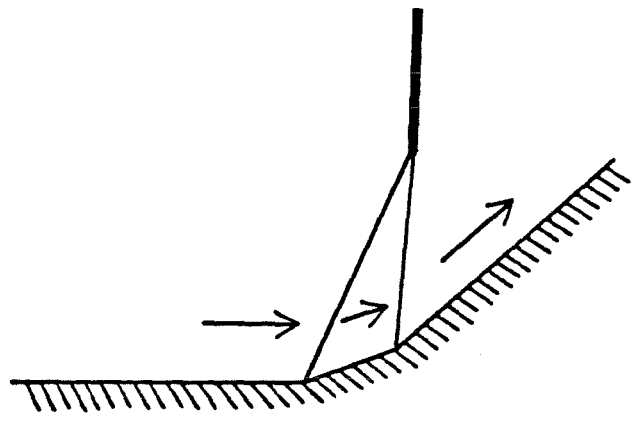

Figure 5.2. Two shocks coincide in space to form a stronger shock.

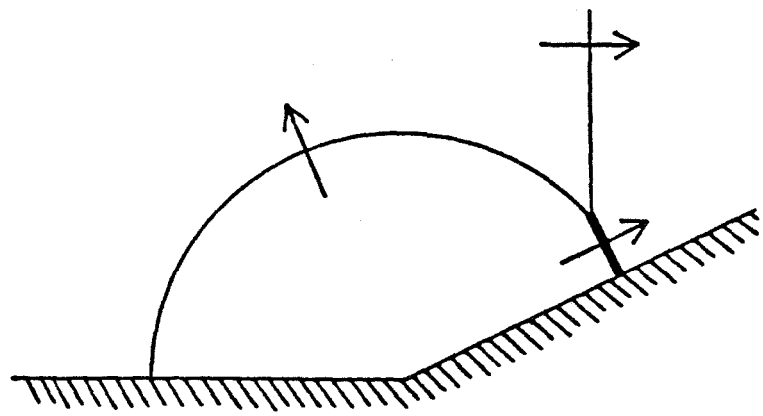

Figure 5.3. A Mach stem is stronger than the incident shock.

where $A(x)$ is the area of the channel (Whitham, 1974). For weak waves, $M-1 \propto s$, so

$$\frac{M(x)-1}{M(x_0)-1}=\left[\frac{A(x_0)}{A(x)}\right]^{\frac{1}{2}}. \tag{5.2}$$

If a spherically converging channel is chosen, equation (5.2) reduces to

$$\frac{M(r)-1}{M(r_0)-1}=\frac{r_0}{r}. \tag{5.3}$$

It should be emphasized that this relation retains its validity only so long as $M(r)-1 \ll 1$. If a shock wave travels a distance L down a spherically converging shock tube of initial radius r_0, this relation may be integrated to yield

$$< M > = \frac{L}{at_A}= 1-(M_0-1)\,\frac{r_0}{L}\ln\left[1-\frac{L}{r_0}\right] \tag{5.4}$$

where t_A is the arrival time. Since

$$\frac{M_L-1}{M_0-1}=\frac{r_0}{r_0-L}=\left[1-\frac{L}{r_0}\right]^{-1}, \tag{5.5}$$

this may be combined with equation (5.4).

$$< M > = \frac{L}{at_A}= 1+(M_L-1)\left[1-\frac{r_0}{L}\right]\ln\left[1-\frac{L}{r_0}\right] \tag{5.6}$$

It is this expression which for weak waves relates the average and final Mach

numbers or the arrival time and final temperature jump where

$$M_L = 1 + \frac{1}{2}B\,\frac{\Delta T_L}{T} \tag{5.7}$$

so

$$< M > - 1 = \frac{1}{2}B\left[1 - \frac{\tau_0}{L}\right]\ln\left[1 - \frac{L}{\tau_0}\right]\frac{\Delta T_L}{T}. \tag{5.8}$$

5.2. Difficulties Associated with Converging Shocks

There are a few difficulties in producing spherically converging shocks. Whenever a curved shock is produced, the question of stability arises. In many cases strong converging shocks have been shown to be unstable to perturbations on the shock front (Whitham, 1974). In these cases the perturbations on the front are strengthened by the converging geometry faster than the nonlinear wave speed can smooth them out (as occurs for a plane shock). However, experiments by Perry and Kantrowitz (1951) on *weak* cylindrically converging shocks yield very symmetric wave fronts. Experiments such as these give reason to hope that stability considerations for weak spherically converging second sound shocks will be unimportant.

A far more important problem occurs in the experimental realm. For all other second sound shock experiments, the heat fluxes were produced by *planar* thin film Nichrome heaters of uniform thickness. These heaters were (easily) fabricated by vacuum deposition of Nichrome on to a planar substrate, either quartz or glass, sufficiently far removed from the Nichrome source so as to produce a film of uniform thickness. Producing a curved uniform heater is much more difficult since placing the substrate at a large distance from the

source will guarantee a *nonuniform* heater. Moreover, getting sharp boundaries for the heater and leads requires spherical masks conforming exactly to the substrate curvature. In due time all of these problems were overcome.

5.3. Apparatus

The converging channel shown in Figure 5.4 was designed to fit in the rotating shock tube (see Appendix C). In this way building another complete shock tube could be avoided.

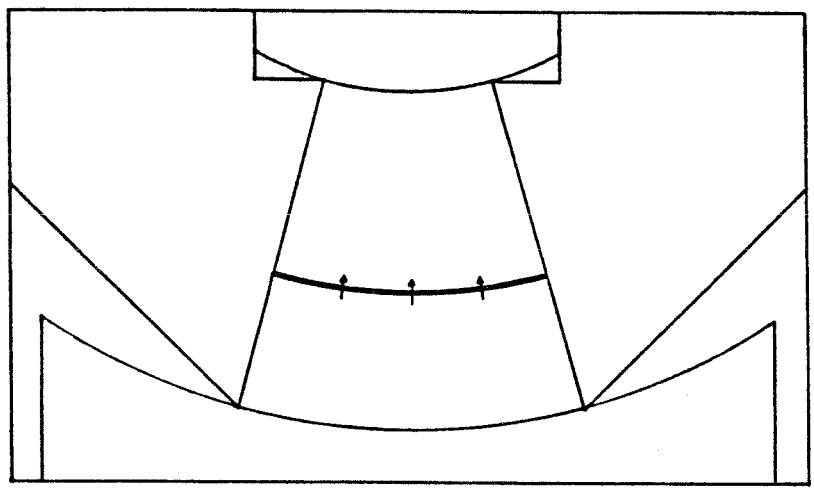

Figure 5.4 The spherically converging shock tube.

The shock "tube" itself was a conical channel with half-angle 15° in a cylindrical piece of teflon. This channel had a length L = 1.14 cm at superfluid helium temperatures and an area contraction of approximately 3:1. The channel cross section was 1.7% of the surface area of a sphere of the same raidus. The edges of the channel are perpendicular to the heater and sensor. For the heater, a plano-concave lens with radius of curvature r_0 = 2.70 cm was used, whereas the sensor was deposited on a plano-convex lens with radius of curvature r_c = 1.30 cm. Pressure loading kept the parts in contact.

5.4. Results

Experiments run with this shock tube were similar to those of Chapter 1. A thermodynamic point (p_o, T_o) was selected, and a series of shock pulses were fired with a suitable waiting time between them to avoid hysteresis. Measured quantities are the arrival time, which corresponds to $< M >$, and the final temperature jump. It should be noted in passing that an endwall sensor was used. Therefore, the temperature jump recorded was approximately double that of the incoming wave (for weak waves this is exact). Since the waves are fairly weak and for lack of a better assumption, the incident wave is taken to have half of the measured temperature jump.

Three such experiments were performed at temperatures of 1.605 K, 1.571 K, and 1.463 K. In all cases the pressure was the saturated vapor pressure plus the hydrostatic head from several inches of helium (1 Torr $\approx$ 4 in He). Figure 5.5 shows the results of these experiments with the right hand side of equation (5.8) plotted vs. the left hand side. These curves are typical of those in Chapter 1 with one important difference. The Mach numbers involved here are much higher in all cases. It is seen in these experiments that the weak wave equation relating $< M >$ and ΔT_L is remarkably well obeyed until there is an abrupt divergence from the prediction. Shown in Table 5.1 are values associated with the maximum ΔT_L in each case. The Khalatnikov values and exact numerical calculations (Moody, 1983) of Mach number and relative velocity in $\frac{m}{sec}$ are given for comparison.

The values for M_o were determined by using the Khalatnikov relation relating ΔT_L to M_L and the weak wave area relation.

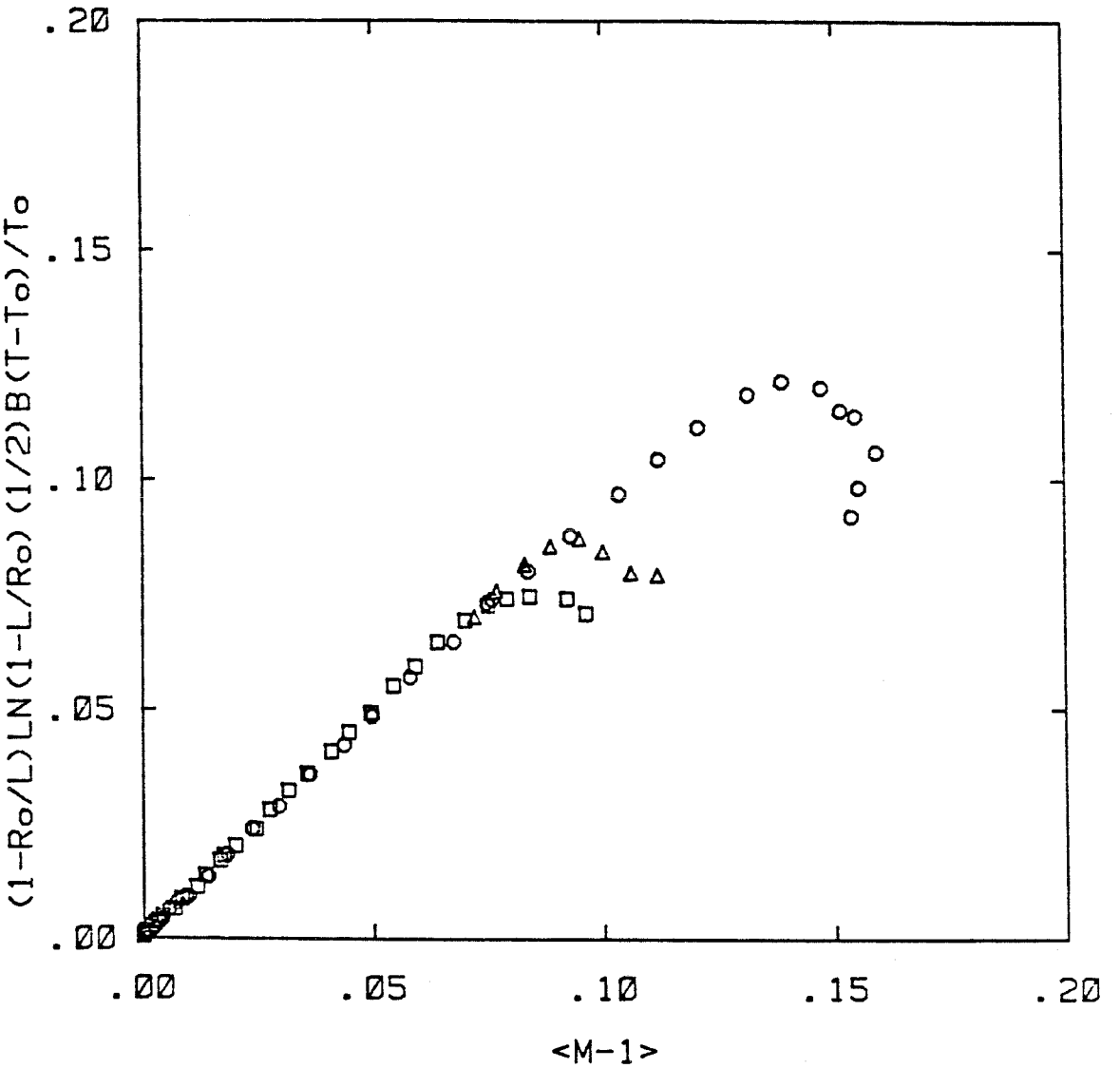

Figure 5.5. Final temperature jump (scaled) vs. average Mach number. □ are at T = 1.605 K, △ are at T = 1.571 K, ○ are at T = 1.463 K.

Table 5.1. Strong Converging Shocks

T_o	ΔT_L	$\langle M \rangle$	M_o	M_L(Khal.)	M_L(Moody)	w (Khal.)	w(Moody)
1.605	0.071	1.084	1.057	1.098	1.148	6.0	7.6
1.571	0.076	1.095	1.067	1.115	1.182	6.5	8.3
1.463	0.087	1.139	1.093	1.161	1.302	7.6	10.7

$$M_o - 1 = \frac{1}{2} B \frac{\Delta T_o}{T} \tag{5.9}$$

$$\Delta T_o = \left(1 - \frac{L}{r_o}\right) \Delta T_L \tag{5.10}$$

In each of the three experiments above, the calculated M_o values are in good agreement with maximum values of $< M >$ for the straight channel experiments of Chapter 1 and for those of Turner (1979).

One purpose of these converging experiments was to produce breakdown in the bulk fluid. If this had occurred, however, the temperature jumps at the sensor would have been far less, so in view of the data, it seems likely that breakdown is still occurring at the heater. To evaluate this hypothesis, it is instructive to compare calculations of ΔT_o and M_o from the above experiments with straight channel data at similar thermodynamic conditions. It is unfortunate that M_o and ΔT_o data are not available for the straight channel experiments. Instead, one can only make use of $< M >$ and ΔT_L for these experiments. This is no real hindrance, however, since in a straight channel $< M >$ and ΔT_L are changed only by triangular wave decay, a relatively weak effect. Thus, if

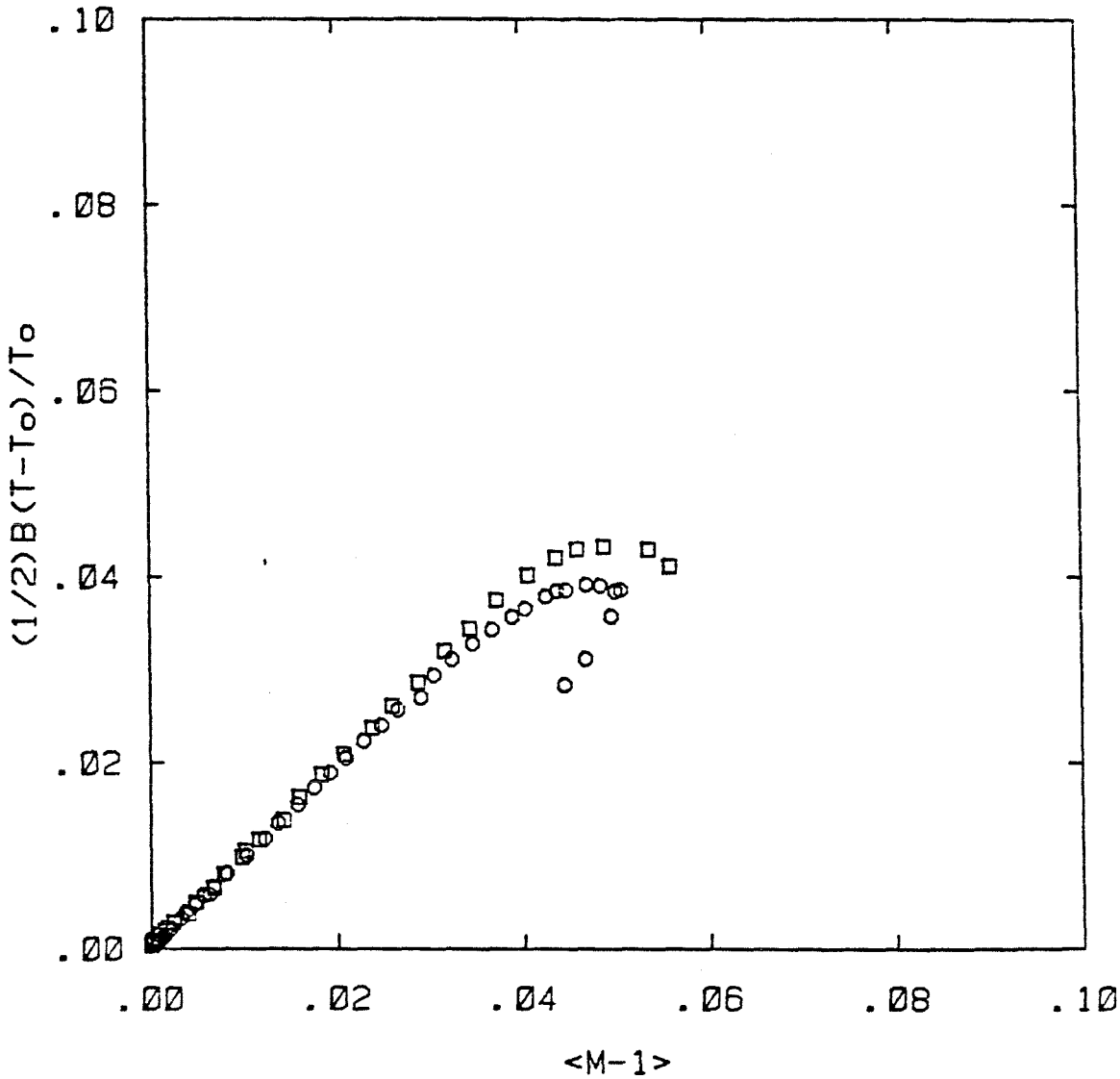

Figure 5.6. Calculated initial quantities from converging experiment (□) at T = 1.605 K compared with straight channel experiment H5 (○) at T = 1.609 K.

breakdown occurs at the heater, one expects these two data sets to lie almost atop one another, with the straight channel points slightly beneath the converging points. Figure 5.6 shows that this is indeed the case. It is concluded that the breakdown occurs principally at the heater.

5.5. Metastability

Associated with a second sound shockwave are jumps in all thermodynamic parameters, not just the temperature, although most attention is focused on it. Khalatnikov worked out the pressure perturbation across a second sound shock, neglecting the coefficient of thermal expansion. If this is not neglected (Lifshitz, 1944), the pressure jump becomes

$$\Delta p = -\beta\rho\left[\frac{a_1^2\, a_2^2}{a_1^2 - a_2^2}\right]\Delta T - \left[\frac{\rho_s\rho_n}{\rho} - \frac{1}{2}\rho^2\, a_2^2\left[\frac{\partial}{\partial p}\right]_T \frac{\rho_n}{\rho}\right]\left[\frac{\rho_s \Delta T}{\rho_n a_2}\right]^2 \qquad (5.11)$$

where β, the coefficient of thermal expansion, is negative. The coefficient of the quadratic term is dominated by $\frac{\rho_s\rho_n}{\rho}$, so Δp increases slightly and then becomes negative as the quadratic term begins to dominate. Exact numerical calculations (Moody, 1983) bear this out, Δp starting out initially positive, going through 0 typically by $M \lesssim 1.002$, and becoming increasingly negative thereafter.

This raises the possibility of using a second sound shock wave to produce a phase change, but not in the way typically considered. Since the pressure jump across such a shock is negative for any reasonable strength, it is possible to cross the coexistence curve by a *decrease of pressure* rather than by an increase in temperature.

It is of interest to compare the pressure jumps produced across the strongest converging shocks mentioned above.

Table 5.2. Pressure Jumps Across Second Sound Shocks

T	P(s,v,p.)	ΔP(Khal.)	Δp (Moody)
1.605	5.83	-4.65	-10.05
1.571	5.00	-4.96	-11.61
1.463	3.00	-5.55	-14.71

Table 5.2 shows pressure data in Torr for the strongest shocks in the converging experiments. The actual starting pressure for these experiments is about 2 Torr higher than saturated vapor pressure (1 Torr $\approx$ 4 in He). In all cases above, given a reasonable hydrostatic head, the coexistence curve is crossed. Moreover, the exact numerical calculations of Moody suggest that tensile stress was put on the liquid (the pressure became negative). It is possible that this effect may be exploited to study metastable liquid.

Chapter 6

CONCLUSIONS

Two conclusions can be made based upon the above experiments. It has been clearly shown that the presence of vorticity enhances the breakdown of superfluidity. However, in the nonrotating experiments it is found that all of the interaction occurs near the heater, rather than out in the bulk fluid.

Both experiment and theory attest to the role that vorticity plays in the breakdown of superfluidity. Theories of thermally nucleated quantized vortices predict a critical velocity

$$w \propto \frac{\rho_s}{T}.$$

This thermodynamic dependence has been verified experimentally although the numerical constant required to make the above proportionality an equality is approximately an order of magnitude lower than predicted. Nevertheless, the above two facts taken together provide strong evidence that the production of quantized vortex rings is intimately connected with breakdown.

Successive shock experiments demonstrate that a shock that has undergone breakdown leaves disturbances in the fluid after its passage. These disturbances never travel far away from the heater and decay after a few minutes. Note in passing that vortex dynamics predicts that, in the absence of counterflow, vortices will be attracted to and ultimately absorbed by the nearest wall. The presence of these perturbations in the fluid enhances breakdown in a second shock (the successive shock) passing through them. It has also been

shown that the radial thermodynamic gradients of a line vortex, when crossed into the gradients of the shock front, will produce azimuthal vorticity (like Crocco's Theorem).

The rotating experiments demonstrate that decay is enhanced by the presence of vorticity. The axial experiments show that the decay is proportional to the rotation rate (the density of line vortices) and to the distance traveled by the shock. Thus, the decay occurs wherever axial vorticity is located, rather than only near the heater. This decay is qualitatively similar to that observed in the successive shock experiments.

One important difference is observed between the transverse and axial cases. In the transverse case, decay does not begin until the arrival of secondary waves produced by leaks in the heater seal. An analogy with Crocco's Theorem suggests that vorticity should be much more easily produced in the axial case than in the transverse case. It is extremely suggestive that in the transverse case decay does not begin until the secondary waves introduce thermodynamic gradients *along* the vortices (as they do in the axial case).

It seems well established that the production of vortices is involved in the breakdown process. It is interesting to note, however, that in all stationary experiments breakdown occurred near the heater. In straight channel experiments the pulses did not decay anomalously while propagating. The successive shock experiments indicated that disturbances were produced only near the heater and remained there until they decayed away.

That the region of decay is near the heater was shown most dramatically by the spherically converging shock experiments. In these experiments relative velocities greater than $10\frac{m}{sec}$ were produced in the bulk fluid. However, when compared with the straight channel experiments, back calculation of the

conditions at the heater in the converging experiments unmistakably shows that the limiting phenomena occur there. Thus, the difficulty is getting the heat into the helium rather than propagating it by counterflow.

Appendix A

COLLECTED HELIUM EQUATIONS

A.1. The Landau Two-Fluid Equations with Dissipation

MASS CONSERVATION:

$$\frac{\partial}{\partial t}\rho + \nabla \cdot \rho\vec{v} = 0$$

MOMENTUM CONSERVATION:

$$\frac{\partial}{\partial t}\rho\vec{v} + \nabla \cdot \left[\rho\vec{v}\vec{v} + \frac{\rho_n\rho_s}{\rho}\vec{w}\vec{w} + pI + \tau^*\right] = 0$$

ENERGY CONSERVATION:

$$\frac{\partial}{\partial t}\left[\rho e + \frac{1}{2}\rho v^2 + \frac{1}{2}\frac{\rho_n\rho_s}{\rho}w^2\right]$$

$$+ \nabla \cdot \left[\vec{v}\left[\rho e + p + \frac{1}{2}\rho v^2 + \frac{1}{2}\frac{\rho_n\rho_s}{\rho}w^2\right]\right.$$

$$\left. + \frac{\rho_s}{\rho}\vec{w}\left[\rho_n\vec{w} \cdot \vec{v}_n + \rho ST\right] + \vec{Q}^*\right] = 0$$

SUPERFLUID EQUATION:

$$\frac{\partial}{\partial t}\vec{v}_s + \nabla \left[\mu + \frac{1}{2}v_s^2 + h^*\right] = 0$$

where

$$I = \textit{identity tensor}$$

τ^*, $\vec{Q}^*$, h^* are the dissipative fluxes

$$e = sT - \frac{p}{\rho} + \mu + \frac{1}{2}\frac{\rho_n}{\rho}w^2$$

NOTE: All thermodynamic variables have an intrinsic dependence on w^2.

$$\tau_{ik}^* = -\eta\left[\frac{\partial v_{ni}}{\partial x_k} + \frac{\partial v_{nk}}{\partial x_i} - \frac{2}{3}\delta_{ik}\,\nabla\cdot\vec{v}_n\right]$$

$$-\delta_{ik}\left[\zeta_1\,\nabla\cdot(\vec{j} - \rho\vec{v}_n) + \zeta_2\,\nabla\cdot\vec{v}_n\right]$$

$$h^* = -\zeta_3\,\nabla\cdot(\vec{j} - \rho\vec{v}_n) - \zeta_4\,\nabla\cdot\vec{v}_n$$

$$\vec{Q}^* = -\kappa\nabla\,T + h^*(\vec{j} - \rho\vec{v}_n) + \tau^*\cdot\vec{v}_n$$

From the Onsager symmetry principle $\zeta_4 = \zeta_1$; also, the requirement that entropy production be positive-definite ensures that η, ζ_2, ζ_3, and κ are positive and $\zeta_1^2 < \zeta_2\zeta_3$.

A.2. Other Assorted Equations and Identities

ENTROPY CONSERVATION (ignores dissipation):

$$\frac{\partial}{\partial t}\rho s + \nabla \cdot \rho s \vec{v}_n = 0$$

"$\vec{A}$" EQUATION (ignores dissipation):

$$\frac{\partial}{\partial t}\vec{A} + \nabla (T + \vec{v}_n \cdot \vec{A}) = \vec{v}_n \times (\nabla \times \vec{A})$$

$$\vec{A} = \frac{\rho_n \vec{w}}{\rho s}$$

CHEMICAL POTENTIAL DIFFERENTIAL:

$$d\mu = \frac{dp}{\rho} - s dT - \frac{1}{2}\frac{\rho_n}{\rho} d(w^2)$$

IRROTATIONALITY:

$$\nabla \times \vec{v}_s = 0$$

VELOCITY RELATIONS:

$$\vec{v} = \frac{\rho_s}{\rho}\vec{v}_s + \frac{\rho_n}{\rho}\vec{v}_n$$

$$\vec{w} = \vec{v}_n - \vec{v}_s$$

$$\vec{v}_s = \vec{v} - \frac{\rho_n}{\rho}\vec{w}$$

$$\vec{v}_n = \vec{v} + \frac{\rho_s}{\rho}\vec{w}$$

A.3. Weak Wave Results

FIRST SOUND SHOCK:

$$M = 1 + \frac{1}{2}D\,\frac{\Delta p}{p}$$

$$D = p\left[\frac{\partial}{\partial p}\right]_s \ln(\rho a_1)$$

$$\Delta u = \frac{\Delta p}{\rho a_1}$$

SECOND SOUND SHOCK:

$$M = 1 + \frac{1}{2}B\,\frac{\Delta T}{T}$$

$$B = T\left[\frac{\partial}{\partial T}\right]_p \ln\left[\frac{a_2^3\, c_p}{T}\right]$$

$$\Delta w = a_2\left[\frac{\rho\, c_p}{\rho_s s}\right]\frac{\Delta T}{T}$$

Appendix B

THE ROTATING DEWAR

The rotating liquid helium apparatus consists of three main parts: the dewar assembly, the rotating table, and its controlling electronics. The dewar system itself is contained in an aluminum framework about 3-1/2 feet high (see Fig. B.1). The outer liquid nitrogen dewar is encased in a protective lucite cylinder which is kept in place by padded wooden supports. The inner vacuum-jacketed liquid helium dewar, which seals to the aluminum top plate, is held there by a padded aluminum collar. The collar was designed so that the position of the helium dewar might be shifted for centering purposes. The "arm" of the helium dewar is plugged with a rubber stopper: evaporated helium is removed through the twin 1-5/8 inch vacuum lines which are connected to the "cap" that seals to the top of the aluminum support plate. The "cap" has four other ports, three of which are available for vacuum-tight BNC feed throughs. The fourth port is reserved for the barocel manometer so that absolute pressure measurements may be made (and hence the temperature determined). Pressure tests on the whole system indicate a leak rate of approximately 50 $\frac{\mu Torr-liter}{sec}$, about two orders of magnitude smaller than that of the large GALCIT research dewar.

The entire dewar apparatus is bolted to the stainless steel table top. The top is 24 inches in diameter and 1/2 inch thick, with degree markings ruled on the edge, and has a load capacity of about 1000 lbs. This limit is well above the actual weight of the dewar. The twin vacuum lines pass through the table top and underneath it to rejoin in a coupling which is sealed to the rotating axial vacuum line (1.97 inches in diameter). Inside the base of the table, the rotating vacuum line is joined through a Ferrofluidics rotary shaft seal to a stationary

line, which is connected to the main lab vacuum line after passing through a pressure regulator. Also mounted on axis are 24 Fabricast slip rings, rated at 20 amps. Signals may be transmitted to and from the dewar apparatus through these slip rings, which are accessed through 24-pin connectors mounted on the table top and the base. An optical encoder disc for direct angular velocity measurements is attached to the axis (see below for discussion).

The table is operated by a control panel which permits the selection of different modes and rates. The two modes that can be chosen involve using an external voltage reference to move the table to a prescribed angular location (program mode) or selecting a constant turn rate and direction, either clockwise or counter-clockwise (rate mode). The velocity ranges available are as follows for the rate mode:

Table B.1.

Full Scale Range	Rate Selection
10,000°/second	0 to 2000°/second
1,000°/second	0 to 999.9°/second
100°/second	0 to 99.99°/second
10°/second	0 to 9.999°/second
1°/second	0 to .9999°/second

The resolution is 0.01% of the full scale range, with an accuracy of 0.1% of the selected rate or 0.01% of the full scale range, whichever is greater. A more accurate value for the rate may be obtained using the optical encoder, a disk with 6000 lines equidistantly spaced around its edge. This disk is attached to the rotating axis, and a photodiode above senses the alternating light and dark pattern produced by lines blocking out the light from a small lightbulb below the

disk. Very accurate velocities can be calculated by counting the number of shadows (lines) that pass the photodiode in a set time interval. The table will reach a selected velocity in a matter of seconds since the angular acceleration is approximately $500°/sec^2$. The HOLD feature of the table allows smooth shifting from one rate to another without stopping when a new rate is selected.

The entire apparatus is 8-1/2 feet high and 2 feet wide. Because of the height, a special Janis flexible helium transfer tube is used to fill the inner dewar with helium. About five liters of helium are required to cool and fill the inner dewar, and the time for each run is about five hours. The inner diameter of the helium dewar is 2.486 inches at the vacuum jacket (the minimum value), so experiments must fit within a foot-long cylinder of this diameter.

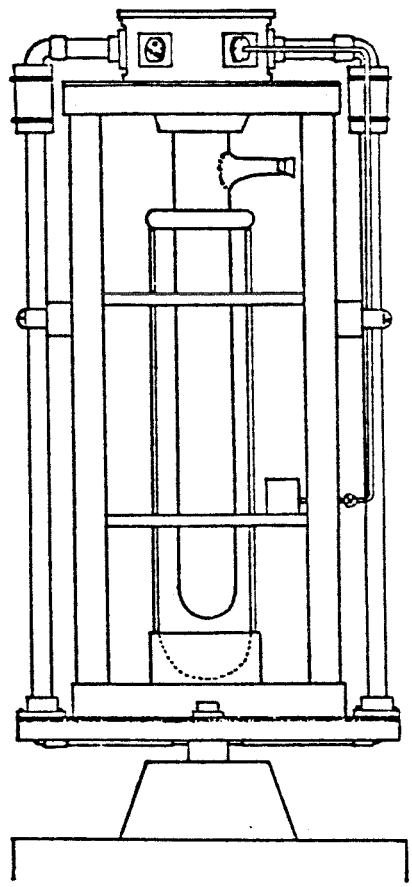

Figure B.1. A schematic of the rotating dewar.

Appendix C

THE SECOND SOUND SHOCK TUBE

Shown in Figure C.1 is a schematic diagram of the rotating second sound shock tube. The shock is produced by impulsively heating a Nichrome thin film evaporated on a planar quartz substrate. The shock propagates down a cylindrical teflon channel, to which the heater is tightly sealed by spring loading. The channel is terminated by another quartz disk, in the center of which is a scribed tin-on-gold superconducting transition edge bolometer. Since the sensor is an endwall sensor, the measured temperature jump is approximately double that of the incident wave. Located behind the sensor is a 7000 turn superconducting magnet, which is used to shift the sensor transition temperature (typically around 2.2 K) to the desired value for the experiment. The heater, sensor, channel, and magnet are contained in a pressurizable brass housing. This housing may be oriented so that the shocks travel along or normal to the axis of rotation.

Figure C.2 shows a typical sensor transition curve. With 1mA of current this sensor has a maximum sensitivity of about $1.6 V/K$. Greater sensitivity may be achieved by increasing the resistance.

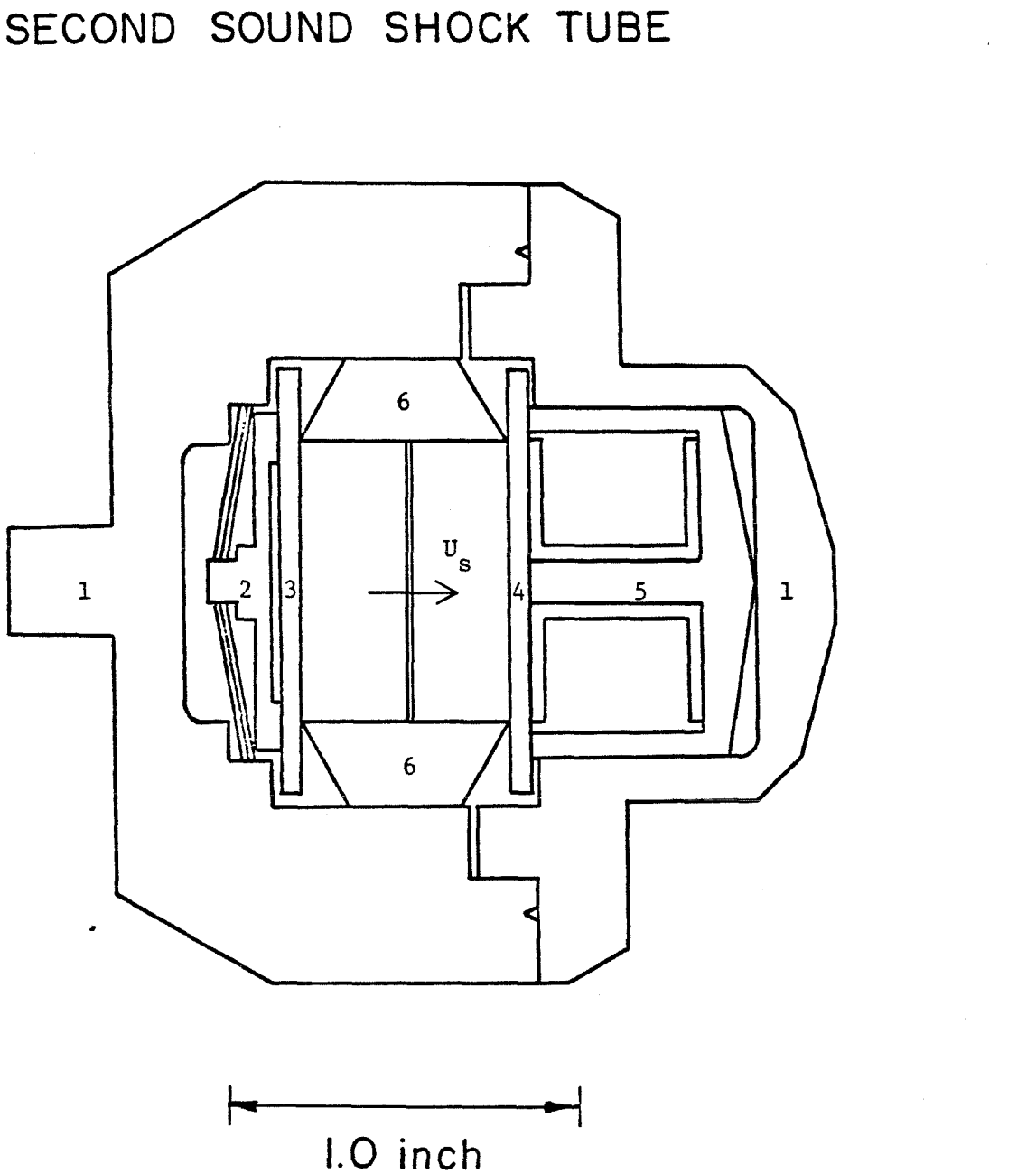

Figure C.1. Second sound shock tube. Labeled parts are:

1. Brass housing.
2. Spring loading for heater.
3. Quartz substrate of heater.
4. Quartz substrate of sensor.
5. Sensor biasing magnet (superconducting).
6. Teflon channel, through which the shock propagates.

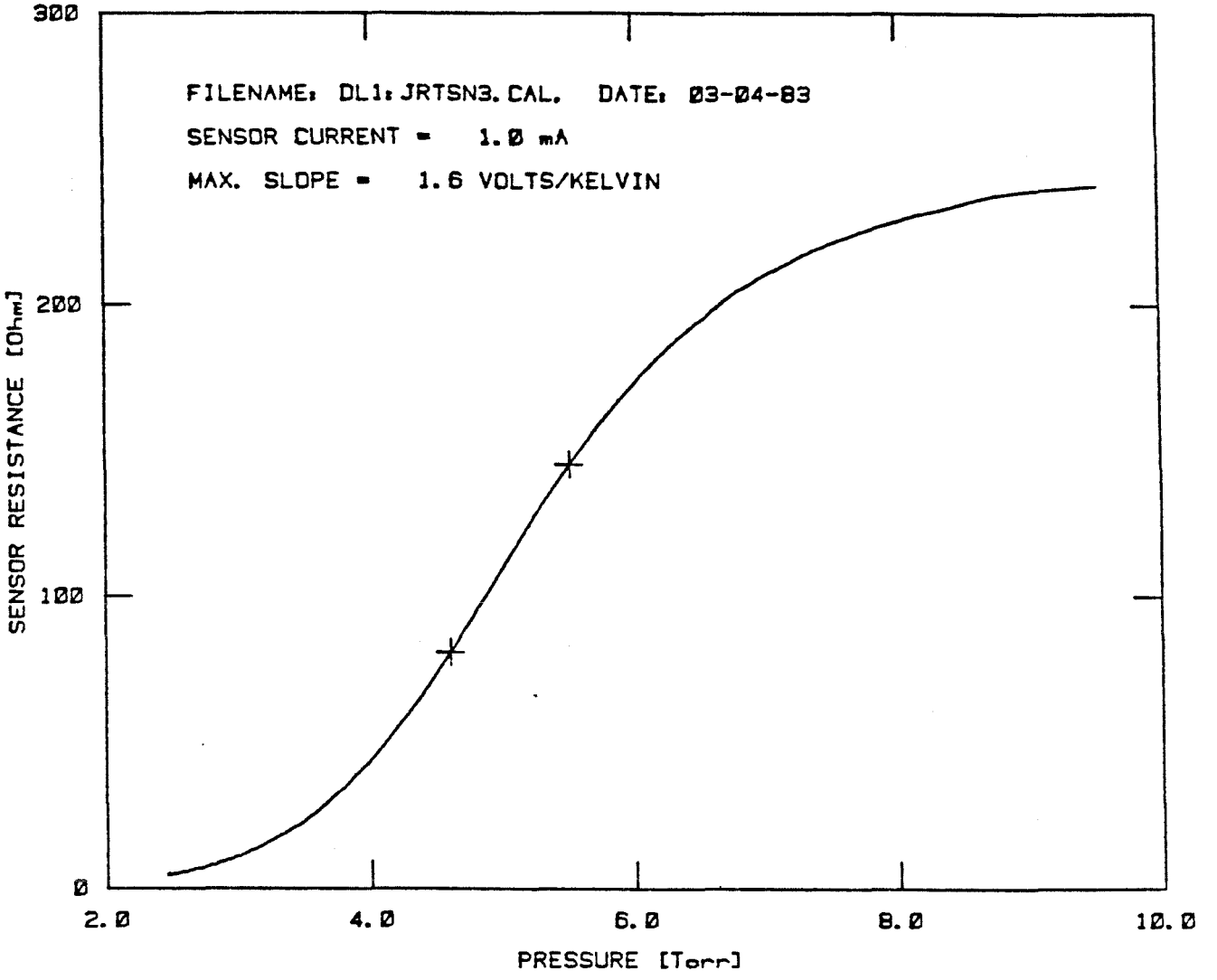

Figure C.2. A typical superconducting sensor transition curve.

Appendix D

TRACE CLEANING

In many cases it is possible to bring out more clearly the features of a second sound shock pulse by a systematic removal of geometric noise (trace cleaning). This correction rests on two basic principles. First, the noise bumps on a shock pulse profile are extremely reproducible from pulse to pulse. Thus, they are not random; rather, they are geometric in that they result from leaks, corners, and irregularities in the shock tube.

To determine the geometric noise at any location in the shock tube, one subtracts from a shock trace its "idealization," a perfect shock, a flat region of uniform counterflow, and so forth. What is left is the geometric noise trace. If this noise trace is then subtracted from other shocks of the same strength at the same location, the cleaned trace is almost identical to the idealization.

The real benefit from such a technique, however, is found in processing decayed shocks. The second principle of trace cleaning is that the noise decays just as the amplitude does for a decayed pulse. In the case of axial rotating experiments, for example, the nonrotating case and its idealization provide the noise trace. To remove the noise from each rotating trace, the noise trace is scaled by the ratio of rotating to nonrotating traces. This scaled noise trace is then subtracted from the rotating trace.

Symbolically this is represented as follows:

S = stationary real trace

SI = stationary idealization

SN = stationary geometric noise

R = rotating real trace

RI = rotating idealization

RN = rotating geometric noise

SN = S-SI

RN = R-RI

Assume: $RN = \frac{R}{S} SN$

Conclude: $RI = R\left(1 - \frac{SN}{S}\right)$

Practically, this algorithm is only useful in the "uniform" region. Elsewhere the situation $\frac{SN}{S} \rightarrow \frac{0}{0}$ often occurs, but this is no real problem since both $SN \rightarrow 0$ and $RN \rightarrow 0$ in these regions.

Figures D.1-2 show typical before and after pictures. Figures that have been so processed in the text are Figures 3.1-4 and 4.2,4-6,8-10,17.

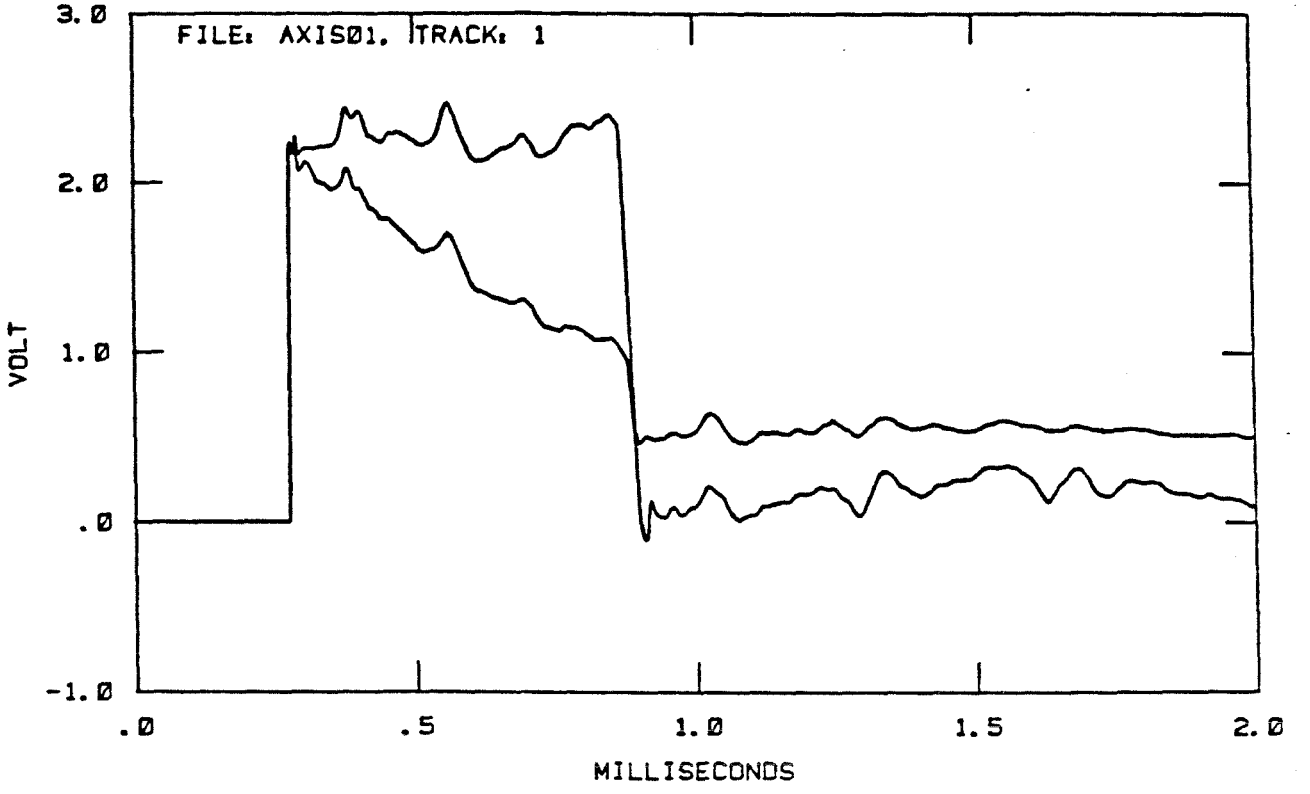

Figure D.1. Two axial shocks that have not been cleaned.

Figure D.2. The same two shocks after cleaning.

Appendix E

ADDITIONAL SHOCK TRACES

Contained in the following pages are more traces of rotating and successive shocks. They are included here for the sake of completeness, at the same time allowing Chapters 3 and 4 to remain uncluttered.

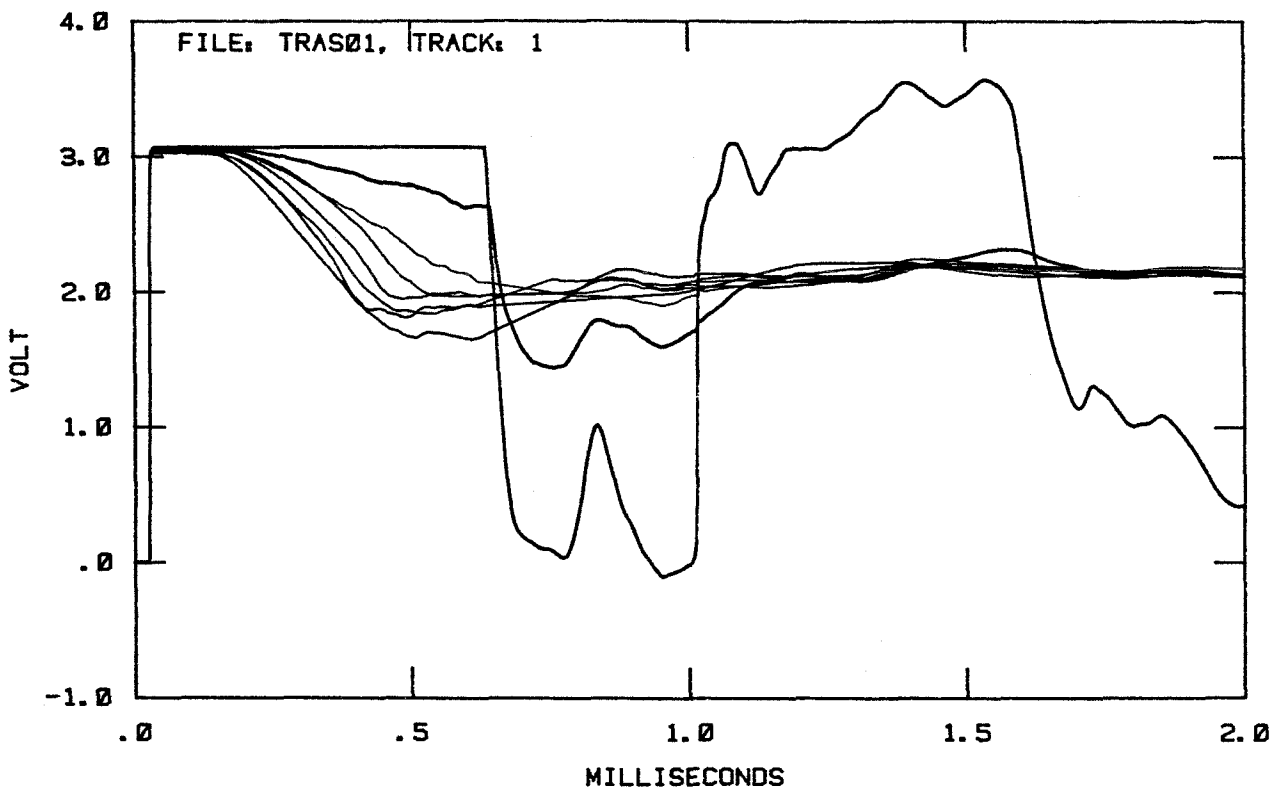

Figure E.1. Transverse shock data for experiment TRAS01 (compare with Figure 4.11). The shock tube length is 0.99 cm. The rotation rate is from 0 ^{o}/sec to 420 ^{o}/sec in increments of 60 ^{o}/sec.

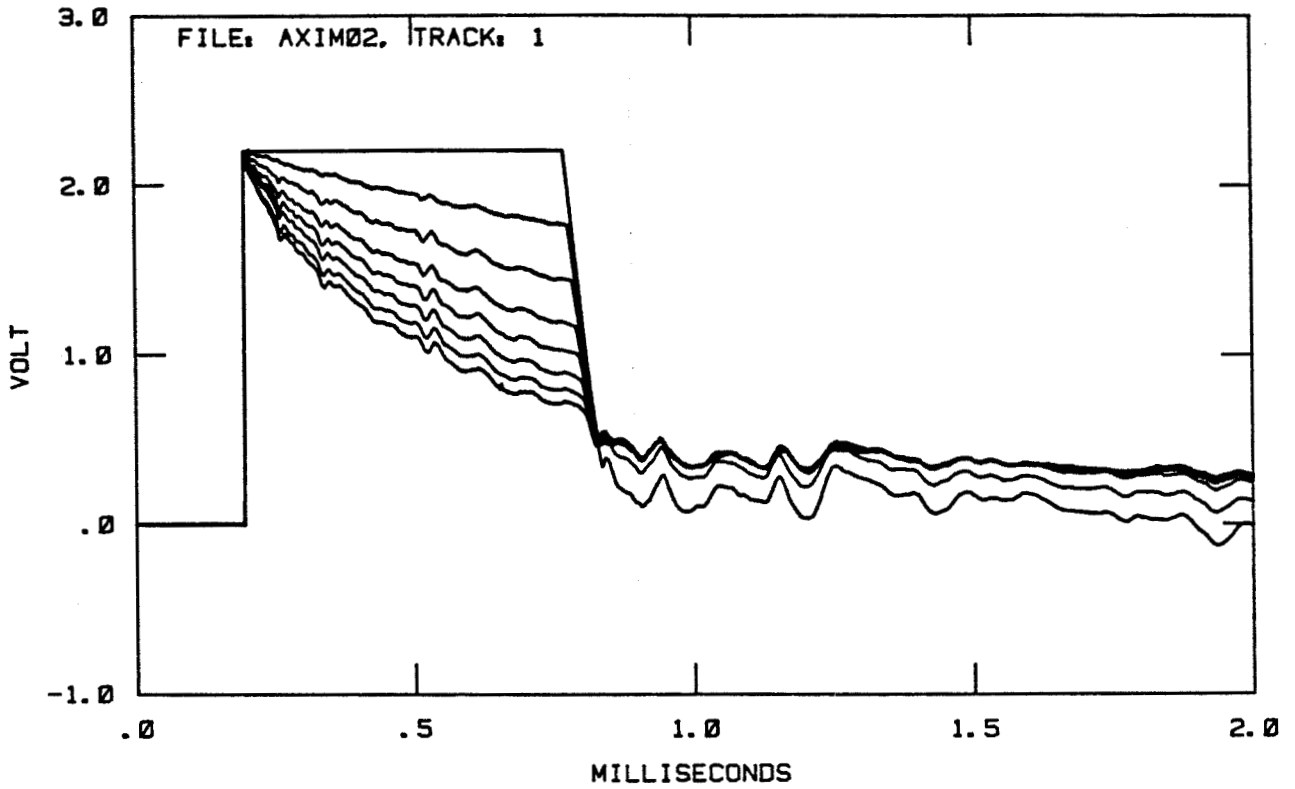

Figure E.2. Axial shock data for experiment AXIM02 (compare with Figure 4.2). The rotation rate is from 0 °/sec to 420 °/sec in increments of 60 °/sec. The shock tube length is 5.81 cm.

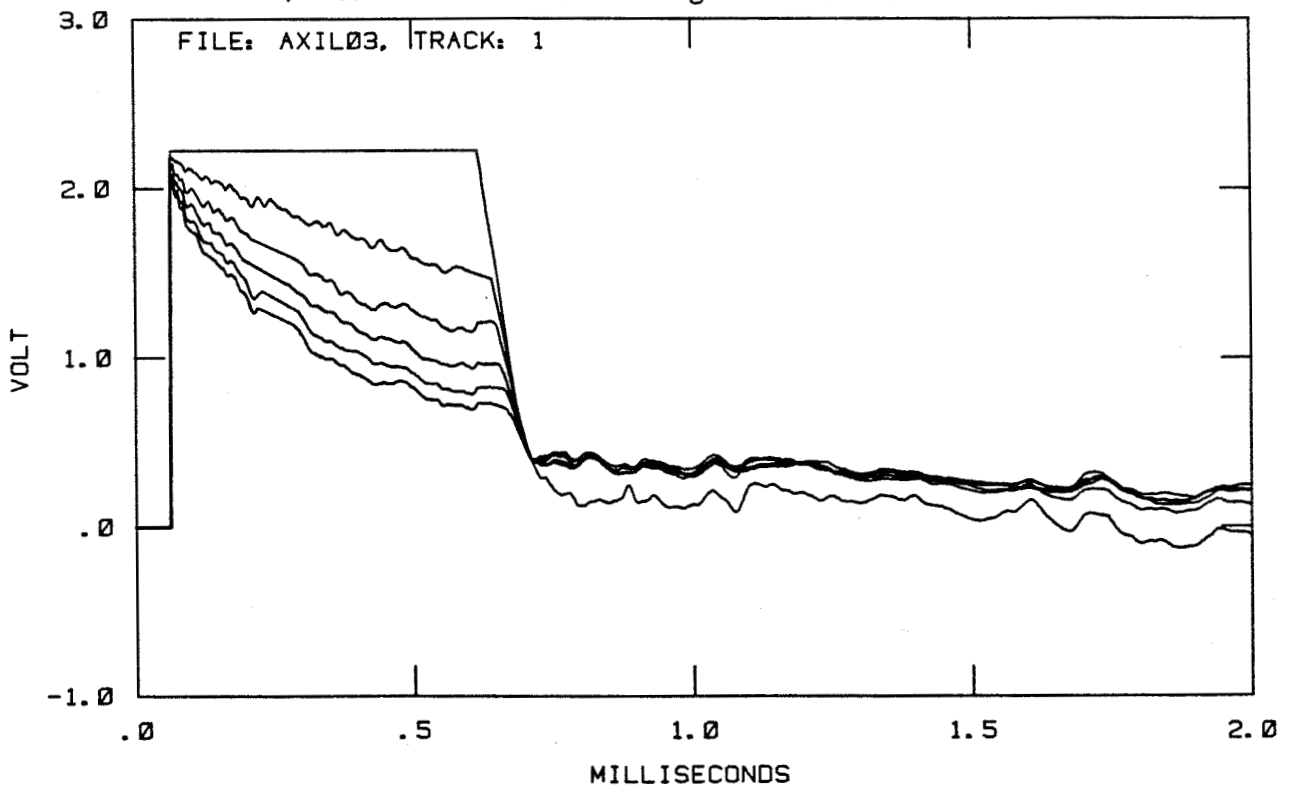

Figure E.3. Axial shock data for experiment AXIL03 (compare with Figure 4.2). The rotation rate is from 0 °/sec to 300 °/sec in increments of 60 °/sec. The shock tube length is 10.52 cm.

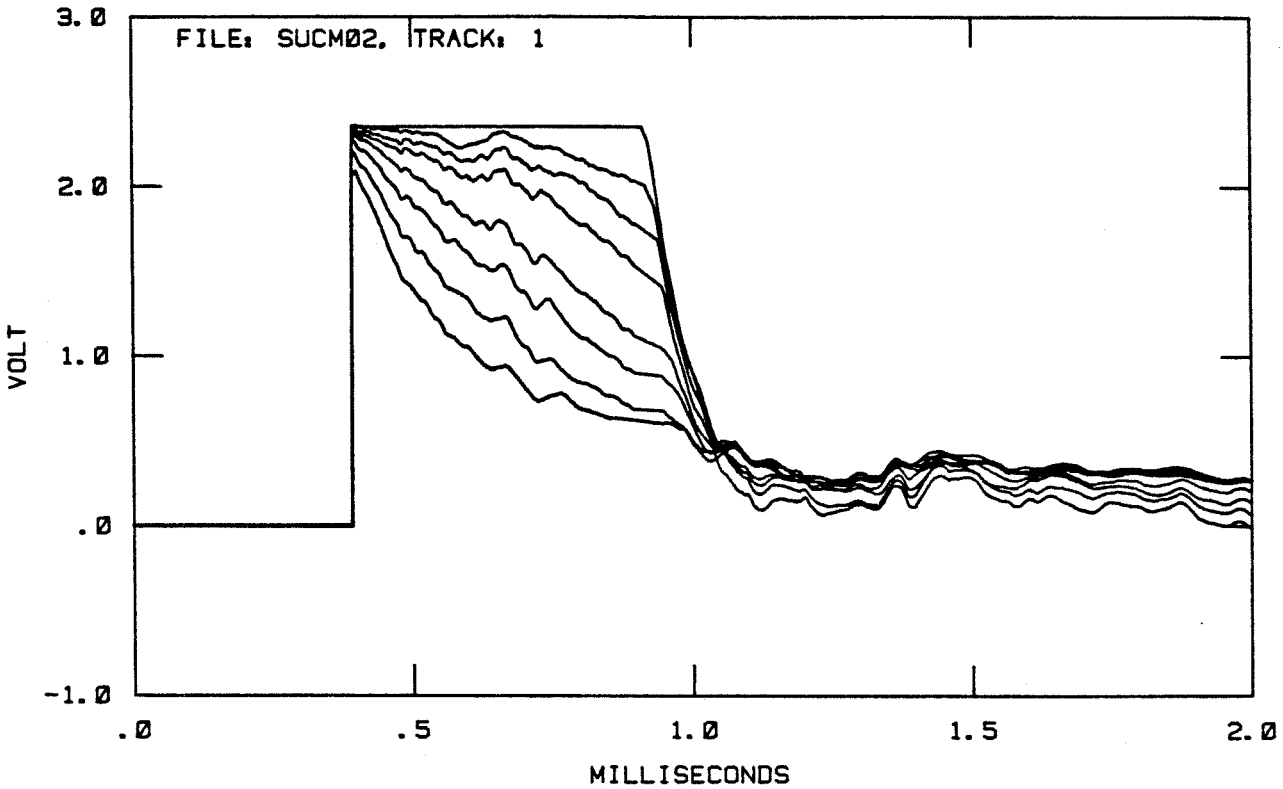

Figure E.4. Successive shock data for experiment SUCM02 (compare with Figure 3.1). The separation times are ∞, 20, 10, 5, 2, 1, 0.5, and 0.2 seconds. The shock tube length is 9.6 cm.

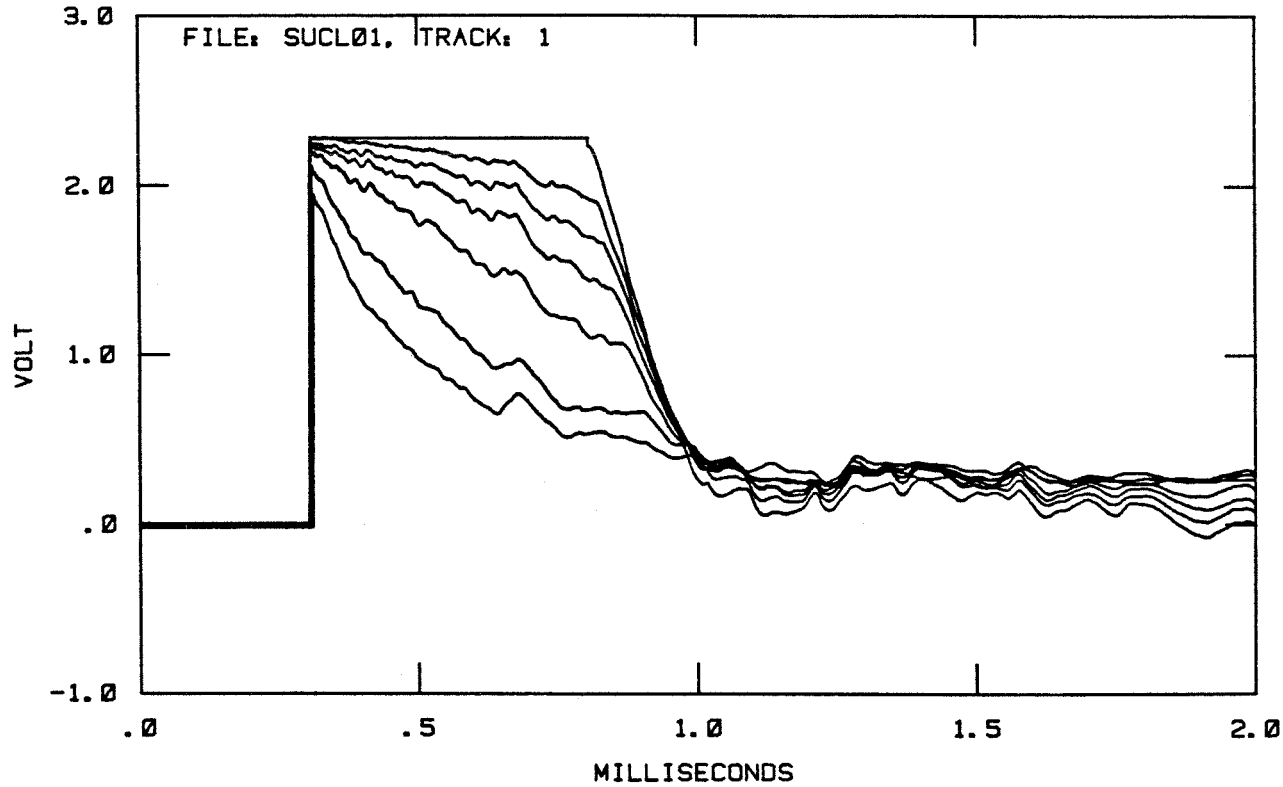

Figure E.5. Successive shock data for experiment SUCL01 (compare with Figure 3.1). The separation times are ∞, 20, 10, 5, 2, 0.5, and 0.2 seconds. The shock tube length is 14.4 cm.

1. References

Atkins, K.R. 1959 *Liquid Helium*. University Press, Cambridge

Catherasoo, C.J. 1982 *Shock Dynamics in Non-Uniform Media*. Ph.D. Thesis, Calif. Inst. of Tech.

Clow, J.R. and Reppy, J.D. 1967 Temperature Dependence of Superfluid Critical Velocities Near T_λ, *Phys. Rev. Lett.*, **19**, 291.

Cummings, J.C., Schmidt, D.W., and Wagner, W.J. 1978 Experiments on Second-Sound Shock Waves in Superfluid Helium, *Phys. Fluids*, **21**, 713.

Dessler, A.J., and Fairbank, W.M. 1956 Amplitude Dependence of the Velocity of Second Sound. *Phys. Rev.*, **104**, 6.

Dimotakis, P.E. 1974 Gorter-Mellink Scale, and Critical Velocities in Liquid-Helium-II Counterflow. *Phys. Rev. A*, **10**, 1721-1723.

Donnelly, R.J. 1967 *Experimental Superfluidity*. The University of Chicago Press, Chicago.

Feynman, R.P. 1955 Application of Quantum Mechanics to Liquid Helium. *Prog. in Low Temp. Phys.*, **1**, 17.

Goodman, S.E. 1971 Classical Model of the Roton-Quantized Vortex Interaction with an Application to Rotating Liquid He II. *Phys. Fluids*, **14**, 1293.

Gorter, C.J., and Mellink, J.H. 1949 On the Irreversible Processes in Liquid Helium II, *Physica* **15**, 285.

Gulyaev, A.I. 1970 Schlieren Photography of Thermal Pulses in Liquid He^4, *Sov. Phys. -- JETP*, **30**, 34.

Hall, M.E. and Vinen, W.F. 1956 The Theory of Mutual Friction in Uniformly Rotating Helium II. *Proc. Roy. Soc.*, **A238**, 215.

Joynson, R.E. 1970 Superconductive Thin Films and Devices, in *Handbook of Thin Film Technology*, (L.I. Maissel and R. Glang, eds.) McGraw-Hill, New York.

Khalatnikov, I.M. 1965 *An Introduction to the Theory of Superfluidity*. W.A. Benjamin, Inc., New York.

Laguna, G.A. 1976 Photolithographic Fabrication of High Frequency Second Sound Detectors, *Cryogenics*, **16**, 241.

Lamb, H. 1945 *Hydrodynamics*, Sixth Edition. Dover Publications, New York.

Landau, L.D. 1941 The Theory of Superfluidity of Helium II. *J. Phys. USSR*, **5**, 71 (in Russian). (See Khalatnikov, 1965, Part V).

Landau, L.D., and Lifshitz, E.M. 1959 *Fluid Mechanics*. Pergamon Press, Oxford.

Langer, J.S. and Fisher, M.E. 1967 Intrinsic Critical Velocity of a Superfluid. *Phys. Rev. Lett.*, **19**, 560.

Maynard, J. 1976 Determination of the Thermodynamics of He II from Sound Velocity Data. *Phys. Rev. B*, **14**. 3868-3891.

Moody, D.M. 1983 *I. Numerical Solution of the Superfluid Helium Shock Jump Conditions. II. Experimental Investigation of the Liquid Helium II-Vapor Interface.* Ph.D. Thesis, Calif. Inst. of Tech.

Notarys, H.A. 1969 Pressure Driven Superfluid Helium Flow. *Phys. Rev. Lett.*, **22**, 1240.

Osborne, D.V. 1951 Second Sound in Liquid Helium II. *Proc. Phys. Soc. (London)*, **64**, 114.

Perry, R.W. and Kantrowitz, A. 1951 The Production and Stability of Converging Shock Waves. *J. Appl. Phys.*,**22**, 878-886.

Putterman, S.J. 1974 *Superfluid Hydrodynamics.* North Holland Publishing Co., Amsterdam.

Tilley, D.R., and Tilley, J. 1974 *Superfluidity and Superconductivity*, Halstead Press, New York.

Thompson, P.A. 1972 *Compressible-Fluid Dynamics.* McGraw-Hill, New York.

Vinen, W.F. 1961 The Detection of Single Quanta of Circulation in Liquid Helium II. *Proc. Roy. Soc. (London)*, **A260**, 218.

White, G.K. 1979 *Experimental Techniques in Low-Temperature Physics.* Third Edition. Clarendon Press, Oxford.

Whitham, G.B. 1974 *Linear and Nonlinear Waves.* John Wiley & Sons, New York.

Whitmore, S.C. and Zimmerman, Jr., W. 1965 Observation of Stable Superfluid Circulation in Liquid Helium II at the Level of One, Two, and Three Quantum Units. *Phys. Rev. Lett.*, **15**, 389.

Whitmore, S.C. and Zimmerman, Jr., W. 1968 Observation of Quantized Circulation in Superfluid Helium. *Phys. Rev.*, **166**, 181.

Wilks, J. 1967 *The Properties of Liquid and Solid Helium.* Clarendon Press, Oxford.

Wise, J.L. 1979 *Experimental Investigation of First and Second Sound Shock Waves in Liquid Helium II.* Ph.D. Thesis, Calif. Inst. of Tech.